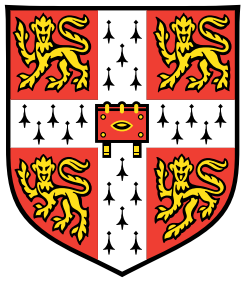

UNIVERSITY OF
CAMBRIDGE INSTITUTE
OF ASTRONOMY

A DISSERTATION SUBMITTED TO THE
UNIVERSITY OF CAMBRIDGE FOR THE DEGREE
OF DOCTOR OF PHILOSOPHY

THE SEARCH FOR THE HIGHEST REDSHIFT QUASARS USING THE DARK ENERGY SURVEY

SOPHIE REED
MURRAY EDWARDS COLLEGE

Submitted to the Board of Graduate Studies
June 2017

UNDER THE SUPERVISION OF
PROF. RICHARD G. MCMAHON
DR MANDA BANERJI

This Thesis would not have happened without the help and support of a lot of people. In particular my supervisors Richard McMahon and Manda Banerji. I need to thank you both for your help, advice and support. Especially to Richard who has now put up with me for five years despite the inability to do basic tasks correctly and the ability to be incredibly grumpy at times. Thank you.

Thanks is also due to everyone at the Institute who has helped me. In particular to Laura Keating who has provided emotional and scientific support to this work. Much gratitude is also due to my collaborators who have helped with this; in particular Paul Hewett and Liam Coatman both of whom have provided important insights.

My parents deserve most of the blame for the decisions that cumulated in me writing this thing. I am truly grateful for their support throughout my foray into science. Love you both and thank you for not minding that I'm not a ballet dancer.

Last but not least I should thank my fiancé, Adam Guterres. I'm incredibly grateful for your support, especially over the last few weeks when I have been very busy. I love you a lot and can't wait for us to start the next bit of our lives together.

DECLARATION OF ORIGINALITY

I, Sophie Reed, declare that this Thesis entitled *The Search for the Highest Redshift Quasars Using the Dark Energy Survey* and the work presented in it, is the result of my own work and includes nothing which is the outcome of work done in collaboration except as declared in the Preface and specified in the text.

Chapter 3 includes work accepted for publication ("*DES J0454-4448: discovery of the first luminous $z \geq 6$ quasar from the Dark Energy Survey*", Reed et al. 2015, MNRAS accepted). Chapter 4 also includes work accepted for publication ("*Eight new luminous $z \geq 6$ quasars discovered via SED model fitting of VISTA, WISE and Dark Energy Survey Year 1 observations*", Reed el at. 2017, accepted).I have always clearly attributed where I have consulted the published work of others, especially in Chapters 1 and 2 which serve as an introduction and largely draw on work in the literature. When appropriate, collaborators and their contribution were specifically named in the text.

I confirm that this thesis is not substantially the same as any that I have submitted, or, is being concurrently submitted for a degree or diploma or other qualification at the University of Cambridge or any other University or similar institution except as declared in the Preface and specified in the text. I further state that no substantial part of my dissertation has already been submitted, or, is being concurrently submitted for any such degree, diploma or other qualification at the University of Cambridge or any other University or similar institution.

The length of this thesis does not exceed the stated limit of the Degree Committee of Physics and Chemistry of 60,000 words.

_____

Signed

_____

Date

Contents

List of Figures

List of Tables

1

Introduction

The hunt for quasars began after the discovery in 1963 by Cyril Hazard of the first quasar (Hazard et al., 1963). Hazard used the method of lunar occultations to determine a sufficiently accurate radio position of 3C 273 to allow an optical counterpart to be identified. This optical counterpart was then classified by Schmidt (1963) as a star-like object with a (then) large redshift of 0.158. The motivation for the occultation work was to provide precise, arcsecond radio positions for high Galactic latitude radio sources in order to establish their nature. The isotropic spatial distribution of these sources suggested to Hazard that these sources were extragalactic and motivated him to search for their true nature. Since this discovery quasars have been searched for at higher and higher redshifts. Initially through radio surveys, then optical and now into the infra red (IR), leading to the discovery of objects up to $z \sim 7$, with the furthest known quasar discovered by Mortlock et al. (2011) at z = 7.1. Recent searches for high redshift quasars are discussed further in Section 1.3.

1.1 What is a Quasar?

A quasar or quasi stellar object is where the central super massive black hole outshines its host galaxy. The Milky Way is observed to host a supermassive black hole with a mass of around 5 million solar masses (Genzel et al. 1996; Ghez et al. 2008; Gillessen et al. 2009). The supermassive black hole is surrounded by an accretion disk which fuels the black hole. The gravitational potential energy of the infalling material is converted to heat and light making these objects some of the brightest in the Universe and thus able to be seen to large distances. Figure 1.1 shows a nearby dormant quasar (Centaurus A) which has an estimated black hole mass of 55 million solar masses. The galaxy can be seen in optical light while the jets are best seen in the radio. The observed spectrum of most normal quasars (i.e. excluding broad absorption line quasars) are dominated by the intrinsic emission line and continuum spectrum of the quasar and these show little variation with redshift. Superposed on

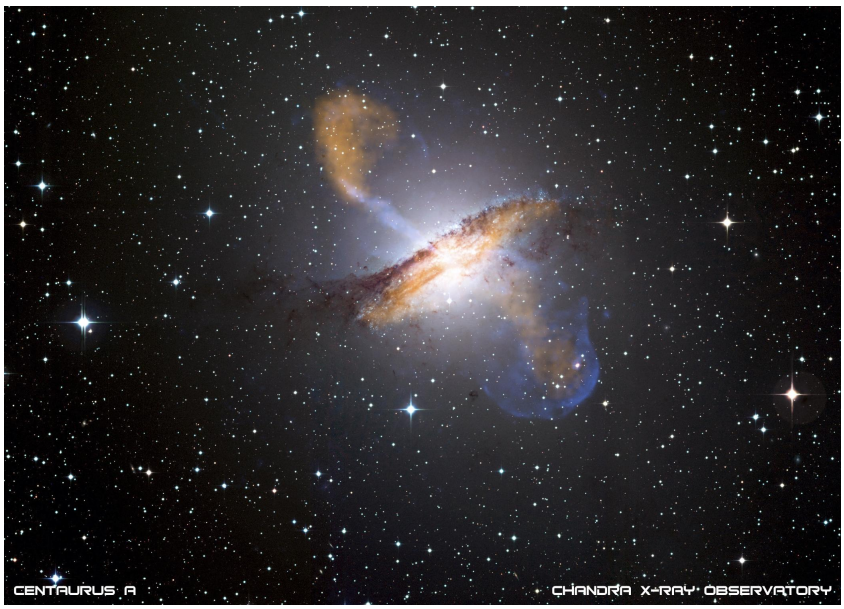

Figure 1.1 Image Credit: X-ray: NASA/CXC/CfA/R.Kraft et al.; Submillimeter: MPIfR/ESO/APEX/A.Weiss et al.; Optical: ESO/WFI. The very bright central engine of the actice galactic nuclei can be seen as well as the bright radio jets.

the intrinsic spectrum are absorption lines due to the cosmologically distributed intervening material such as hydrogen, carbon, nitrogen and oxygen.

1.2 Applications of Quasars

Beyond being intrinsically interesting, high redshift quasars can be used for many science purposes. They provide a unique insight into the Universe from within a billion years of its creation and pose difficult questions for established theories of the formation of supermassive black holes and their associated galaxies. Growing black holes from seeds to the size required to match observations (Mortlock et al. 2011; De Rosa et al. 2011, 2014) has proved challenging for theoretical models of their birth and growth (Volonteri & Rees, 2006). The main science application of high redshift quasars that is focused on in this Thesis is their utility for studying the inter galactic medium (IGM) and their local environment. The spectra of high redshift quasars can be used to elucidate the properties of the IGM as well as giving direct measurements of the neutral hydrogen fraction at the end of reionisation through the study of Lymanα (Lyα) forest absorption (Fan et al. 2006b; Bolton & Haehnelt 2007). Absorption lines in the spectra of high redshift quasars allow the properties of gas and metals to be studied on cosmological scales.

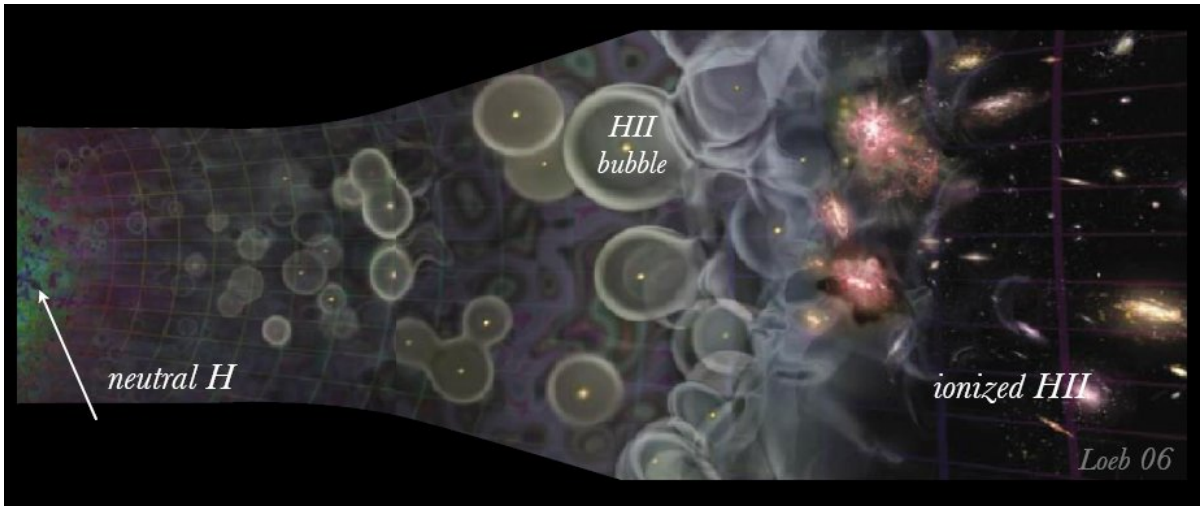

Figure 1.2 Credit: Loeb (2006). A visualisation of the process of reionisation. The initially neutral hydrogen becomes ionised in bubbles surrounding the first bright sources. Eventually these bubbles overlap leading to a fully ionised IGM.

1.2.1 The Epoch of Reionisation

The epoch of reionisation marks the end of the cosmic dark ages when the first ultraviolet (UV) luminous sources ionised the IGM. As the Universe expanded after the Big Bang it also cooled which, at $z \sim 1100$, allowed protons and electrons to combine to form neutral hydrogen, this time is known as recombination. Following recombination, and before the first stars and galaxies were formed, the Universe was mostly cold and neutral. The end of this cosmic dark age was initiated when the first stars ignited and the first galaxies formed, these primordial sources started to ionise the gas surrounding them and thus the epoch of reionisation commenced. Over the history of the Universe there have been two reionisation events, one of hydrogen and one of helium, which happened at lower redshift. The discussion here and throughout this Thesis is concerned with hydrogen. When reionisation is discussed it will refer to hydrogen reionisation rather than helium. A visualisation of the process of reionisation is given in Figure 1.2, which shows the ignition of the first ionising sources and the transition from a neutral to ionised IGM.

Results from the Cosmic Microwave Background (CMB) measurements given in Planck Collaboration et al. (2015) suggest that the beginning of reionisation was at $z \sim 8$. Studies at lower redshifts ($2.0 < z < 6.0$) (Gunn & Peterson 1965; Fan et al. 2006b; Becker et al. 2007) show that the IGM is highly ionised ($n_{HI}/n_H \leq 10^{-4}$) and therefore that reionisation was complete by $z \sim 6$. Quasars are an important tool for studying the redshift interval ($6 < z < 8$) and the discovery of quasars in this interval gives multiple lines of sight along which to study the IGM. Having multiple sight lines is important

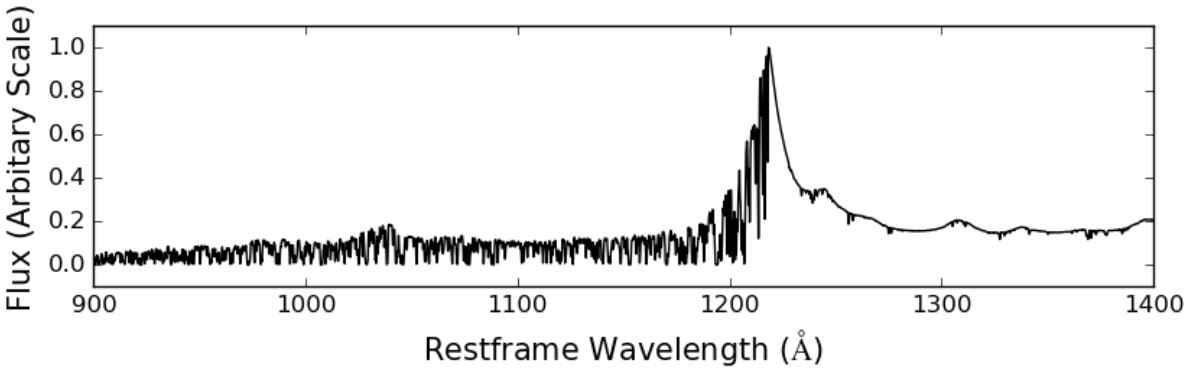

Figure 1.3 Credit: George Becker. Spectrum of a z = 3.62 quasar taken using the Echellette Spectrograph and Imager (Keck telescope). The Lyα forest blueward of the prominent Lyα peak at 1216Å can be seen.

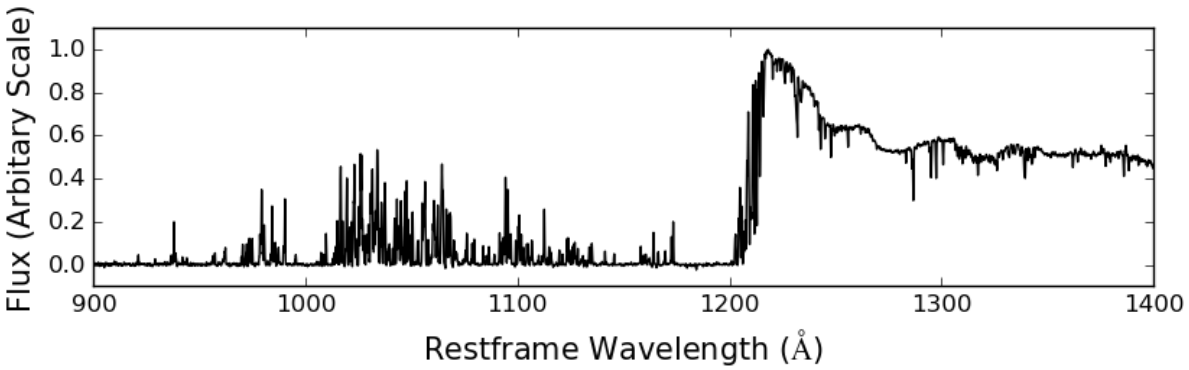

Figure 1.4 Credit: George Becker. A X-Shooter spectrum of a z = 6.12 quasar where the near complete absorption can be seen blueward of the Lyα peak. A dark Gunn Peterson trough can be seen immediately shortward of Lyα formed by the total absorption of the restframe UV flux from the quasar.

as there are indications that reionisation is inhomogeneous (Becker et al., 2015) and as such different paths give disparate times for the completion of reionisation. The patchiness of the process can be seen in Figure 1.2.

Figure 1.3 shows a low redshift quasar spectrum taken by George Becker. The intricate absorption features of the Lyα forest can be seen blueward of the Lyα emission line at 1216Å. Each of these features is due to a cloud of hydrogen gas absorbing the emission from the quasar at that wavelength, where the wavelength in the observed frame is the correct one to excite the Lyα transition in the Hydrogen at the redshift of the cloud. At higher redshift the spectrum in Figure 1.4 shows deeper absorption features with patches of complete absorption indicating an increase in neutral hydrogen along the line of sight to the quasar.

1.2.2 Near Zone Studies

Quasars emit large amounts of high energy (E > 13.6 eV; the ionisation potential of hydrogen) radiation which ionises a bubble around them. This can be seen in their spectra, where there is flux just blueward of Lyα before the spectra becomes fully absorbed and the characteristic Gunn-Peterson trough can be seen. This transmission can be seen in Figure 1.4 where it commences at $\sim$1200Å. The size of these near zones is dependent on the neutral fraction of the surrounding material, the luminosity of the source and how long the source has been emitting the ionising radiation. It has been postulated that near zone sizes measured from high redshift quasars could be used to constrain the end of reionisation (Fan et al. 2006b; Mortlock et al. 2011; Bolton et al. 2011) although care needs to be taken in the interpretation of the sizes as they are dependent on the local environment and the age of the quasar. Measurements of the near zone sizes of larger samples of quasars have shown a tentative trend of decreasing size with redshift (Carilli et al., 2010), but larger samples of high redshift quasars are required to provide robust, statistically significant constraints.

1.2.3 Sources of Reionisation

Reionisation was driven by an increase in the number of ionising photons available to reionise neutral hydrogen. These photons were emitted by the first luminous sources formed but the nature of these sources is still an open question. The number density of bright quasars falls rapidly with redshift suggesting that they do not produce enough ionising photons to be the sole driver of reionisation unless there is a large previously undetected population of faint quasars (Giallongo et al. 2015; Madau & Haardt 2015). As high redshift galaxies are much more common (albeit fainter) they have been suggested to be the source of the ionising flux. However, their contribution depends on the escape fraction of UV photons from the galaxy, which is poorly constrained (Robertson et al. 2015; Bouwens et al. 2015). To address this problem the number of faint high redshift quasars needs to be further investigated.

1.3 Quasar Surveys

The first discovery of a z $\sim$ 6 quasar (Fan et al., 2000) came from the Sloan Digital Sky Survey (SDSS) which was the first survey with enough area, depth and red enough wavebands to find these rare, high redshift objects. The SDSS covered approximately

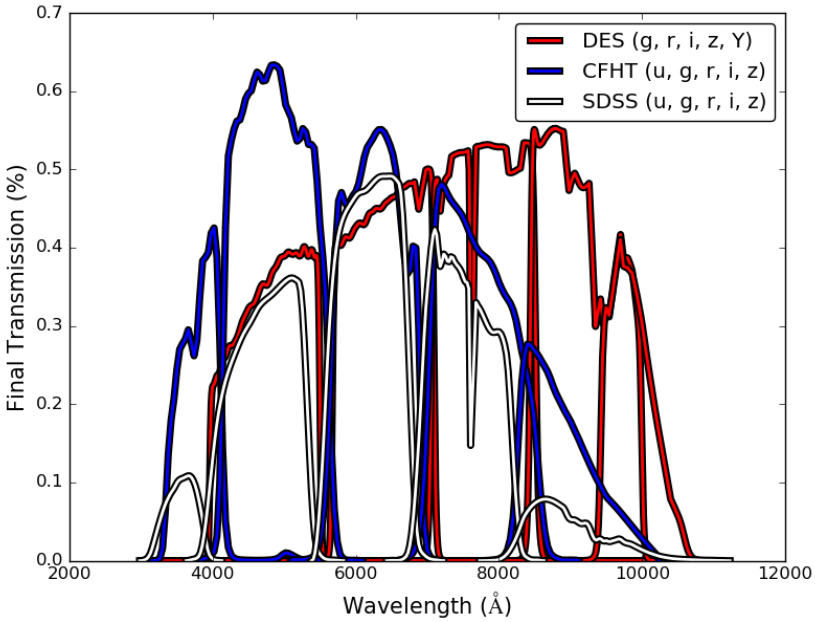

Figure 1.5 A comparison of the SDSS, CFHT and DES filter system throughputs (including atmospheric absorption and other factors). It can be seen that the total transmission is much higher at longer wavelengths for DES than either SDSS or CFHT. This is optimal for high redshift work and makes the data very suitable for the selection of high redshift quasars.

10,000 deg^2 in the northern Galactic Cap in the u, g, r, i and z bands with a 5σ detection limit in each band of 22.3, 23.3, 23.1, 22.3 and 20.8 respectively (York et al., 2000). The large area made the SDSS suitable for rare object searches, however the redshift range it can probe is limited by the shallow magnitude limit of the z band. This is demonstrated in the redshift distribution of the objects discovered, with the majority found between z = 5.7 and z = 6.0. The SDSS was very successful in finding low redshift quasars; from the 7$^{\text{th}}$ data release there were 105,783 quasars found from $\sim$ 9380 deg^2 (Schneider et al., 2010) which were supplemented by 78,086 from 3275 deg^2 in data release nine (Pâris et al., 2012) and 74,454 from 6373 deg^2 in data release ten (Pâris et al., 2014). These quasars are all below z = 6, but there have been a number of searches in the SDSS data for z $\sim$ 6 quasars (Fan et al. (2000) to Fan et al. (2006b), Jiang et al. (2008)) which were concluded with Jiang et al. (2016) bringing the number of high redshift quasars found from SDSS up to 52, of these 28 are at 5.7 < z < 6.0, 19 are at 6.0 < z < 6.2 and the remaining 5 are between 6.2 and 6.5. This is indicative of the diminishing sensitivity of the SDSS instrumentation at z > 6.2. Figure 1.5 shows the differences in total transmission for the different surveys.

The other major search for high redshift quasars used data from the Canada France Hawaii Telescope (CFHT) Quasar Survey. The CFHT team presented their first results in Willott et al. (2005), in which they discovered no quasars, this was fol-

lowed by the discovery of 18 new quasars (Willott et al. 2009, 2010). These were selected from a combination of surveys which are detailed fully in Willott et al. (2009). The area includes $\sim$ 550 deg^2 of the Red-Sequence Cluster Survey 2 (which has 360s exposures in the z band), $\sim$ 150 deg^2 CFHT Legacy Survey (CFHTLS) Very Wide (420s exposure in z), $\sim$ 171 deg^2 in the deeper CFHTLS Wide (z band exposure time 3600s) and 4.47 deg^2 for CFHTLS Deep, the deepest part of the CFHTLS (z band exposure time of 200,000s, z_{limit} = 24.5) which is combined with $\sim$ 1.2 deg^2 from the Subaru/XMM-Newton Deep Survey which is in comparable colours and to comparable depths as the CFHTLS Deep. This area is not limited by z band depth and the search was conducted to a deeper magnitude limit (z = 22.5) than previous surveys. However the z band sensitivity still falls off dramatically with wavelength, limiting the redshift range that the survey can detect. Overall the previous high redshift quasar surveys (e.g. Venemans et al. 2015b; Carnall et al. 2015; Willott et al. 2010; Jiang et al. 2009; Mortlock et al. 2012; Venemans et al. 2013; Fan et al. 2006b) have led to the discovery of $\sim$ 50 quasars at z $\geq$ 6.0.

Following on from the use of optical surveys to find z $\sim$ 6 quasars, large area IR surveys have been used in combination with their optical counterparts to push the redshift range probed. This led to the discovery of ULAS J1120 at z = 7.1 (Mortlock et al., 2011) from the United Kingdom Infra-red Deep Sky Survey (UKIDSS) (Lawrence et al., 2007) Large Area Survey (LAS). ULAS J1120 was, and still is, the highest redshift quasar known upon its discovery, dramatically increasing the previous record of z = 6.44 (Fan et al., 2003).

At the start of this Thesis new quasar searches were just beginning with upcoming large area surveys, such as the Panoramic Survey Telescope and Rapid Response System (Pan-STARRS) (Chambers et al., 2016) which will cover three quarters of the sky in the optical wavebands g, r, i, z and Y to 5σ depths of 23.3, 23.2, 23.1, 22.3 and 21.3 respectively. The Hyper Supreme Camera (HSC) (Aihara et al., 2017) is on an 8m telescope and will cover a smaller area of sky (1400 deg^2) to a greater depth (26.5, 26.1, 25.9, 25.1 and 24.4 5σ depths in g, r, i, z and Y respectively) allowing fainter quasars to be found. Over the next 10 years the Large Synoptic Survey Telescope (LSST) and Euclid will transform the field of quasar surveys. The techniques developed here will be instrumental to exploiting these rich datasets.

Following this introduction, this Thesis introduces the observational datasets used in this work. The next three chapters cover the development of a robust quasar selection method, its application to high redshift and the discoveries made with the method. The final chapter is a study into the uses of quasar near zone measurements to probe the timeline of reionisation. When required, a flat concordance cosmology with Ω_{m0} =

0.3 and H_0 = 70.0 $kms^{-1}Mpc^{-1}$ is used. The code used in this Thesis makes use of the astropy python package (Astropy Collaboration et al., 2013).

2

Observational Datasets

Throughout this Thesis observational data is used from a variety of large scale surveys covering wavelengths from the optical into the mid IR. This chapter details the survey data used and the data releases from these surveys. The surveys used in this work are:

- The VISTA Hemisphere Survey (VHS) - a near IR survey covering the J, H and K_s bands.
- The Dark Energy Survey (DES) - an optical survey collecting data in the g, r, i, z and Y bands.
- The Wide Infrared Survey Explorer (*WISE*) - a mid IR survey which images in the W1, W2, W3 and W4 bands.

A summary of the properties of the surveys used in this work is given in Table 2.1.

2.1 The VISTA Hemisphere Survey

The VISTA Hemisphere Survey (VHS) (McMahon et al., 2013) aims to carry out a near infra red (NIR) survey of $\sim$18,000 deg^2 of the southern hemisphere to a depth 30 times fainter than the Two Micron All Sky Survey (2MASS) in two wavebands J and K_s. The survey uses the 4m VISTA telescope (Sutherland et al., 2015) at ESO's Cerro Paranal Observatory in Chile. In the Southern Galactic Cap, $\sim$5000 deg^2, which will overlap the DES area, is being imaged more deeply (J_{AB} = 21.2, $K_{s;AB}$ = 20.4; 5σ point source depths) with partial coverage in H. The cumulative area against depth is shown in Figure 2.2 for the VHS data. This gives data in three bands (J, H and K_s) in the NIR at $\sim$1 - 2 μm. The filters and system response are shown in Figure 2.1. H band data is not being taken over the full DES and some of the area used in this project does not have H band imaging. The VHS data used in this work were taken between 2009 November 4$^{\rm th}$ and 2014 February 1$^{\rm st}$.

Table 2.1 A summary of the surveys used in this work.

Band	Central Wavelength Å	Full Width Half Max Å	5σ depth Mag [AB]
g	4730	1503	24.0
r	6420	1488	24.4
i	7840	1468	23.9
z	9260	1521	23.1
Y	10090	1126	21.6
J	12520	1725	21.2
H	16460	2916	20.6
K_s	21470	3090	20.4
W1	33530	6358	19.6
W2	46030	11073	19.3
W3	132160	62758	16.7
W4	222230	47397	14.7

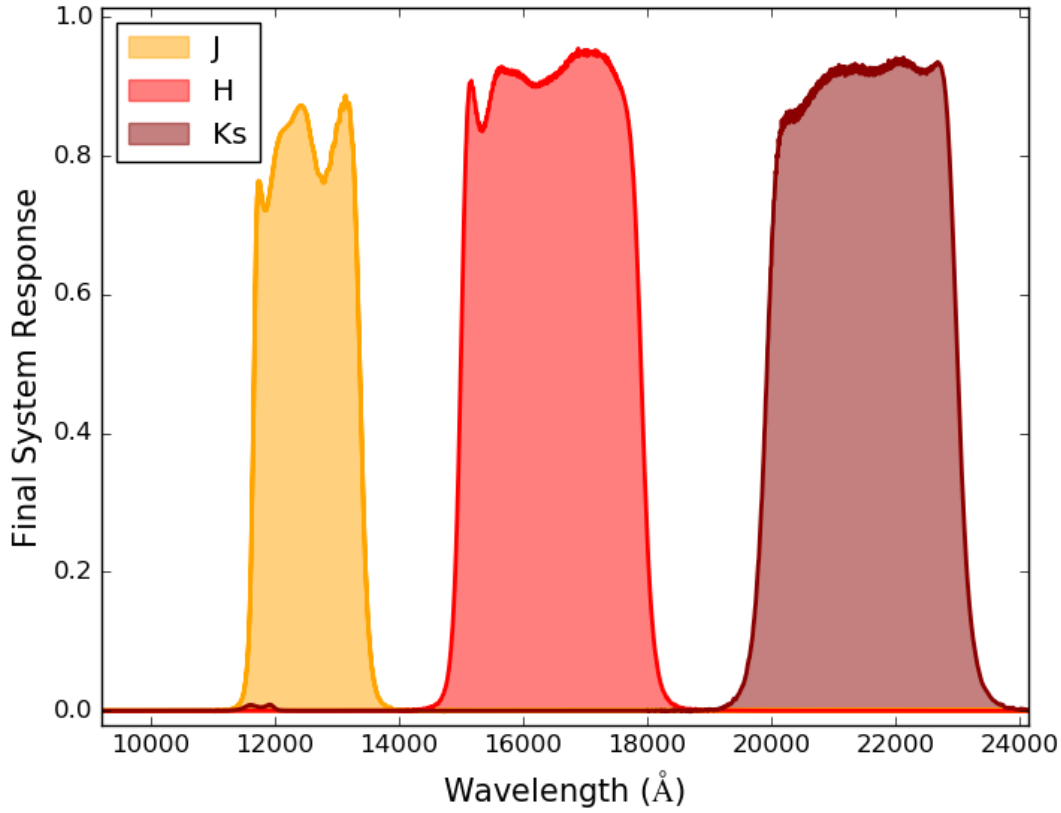

Figure 2.1 The wavelength coverage and system response of the VHS filter set.

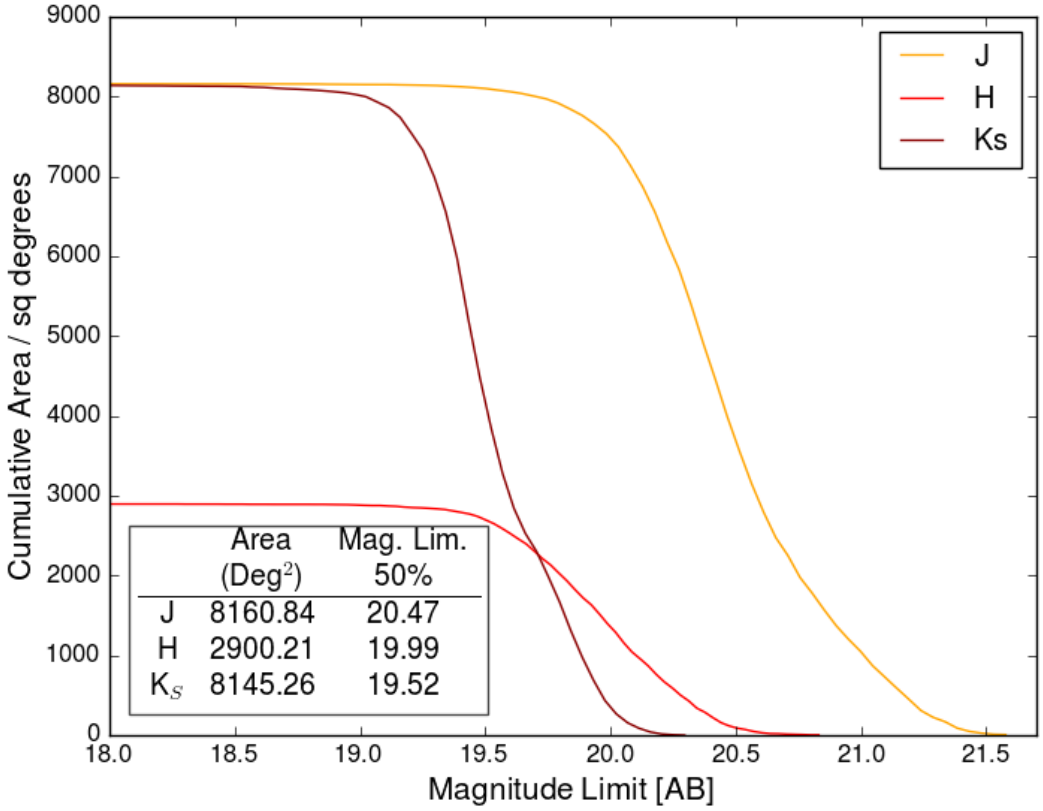

Figure 2.2 Cumulative area versus depth for the three VHS filters. Data from all the VHS areas is included, not just the area that overlaps DES.

The VIRCAM camera (Dalton et al., 2006) used for VHS imaging has a sparse array of 16 individual 2k x 2k MCT (Mercury-Cadmium-Tellurium) detectors covering a region of 0.595 square degrees. Six exposures are required to cover the full 1.5 square degree field of view of the camera. These exposures are then combined into one coadded tile as part of the pipeline processing. The data are processed with the VISTA Data Flow System at CASU (Irwin et al. 2004; Emerson et al. 2004; Lewis et al. 2010) and the science products are available from the ESO Science Archive Facility and the VISTA Science Archive (Hambly et al. 2004; Cross et al. 2012).

The native magnitude system of VHS is Vega; the conversions used from Vega to AB for the VISTA data are: $J_{AB} = J_{Vega} + 0.937$, $H_{AB} = H_{Vega} + 1.384$ and $K_{s,AB} = K_{s,Vega} + 1.839$, these are taken from the Cambridge Astronomical Survey Unit's website. [1]

[1] http://casu.ast.cam.ac.uk/surveys-projects/vista/technical/filter-set

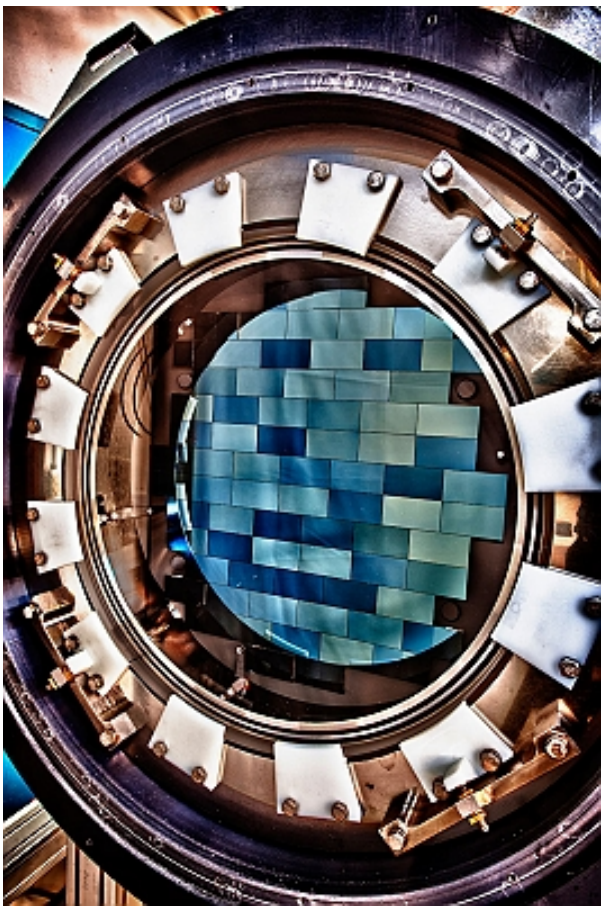

Figure 2.3 Credit: The DES Collaboration. The DECam focal plane where the gaps between the CCDs can be seen.

2.2 The Dark Energy Survey

The Dark Energy Survey (DES) is a multi-band survey aimed at understanding the nature of the dark energy that is driving the expansion of the Universe. The survey is being conducted using the Dark Energy Camera (DECam) (Flaugher et al., 2012). DECam is mounted on the Blanco 4-metre telescope at the Cerro Tololo Inter-American Observatory (CTIO) and the data are processed by the DES data management system (Mohr et al. 2012; Desai et al. 2012). The 570 megapixel DECam has a field of view of 3 deg^2 with 0.27 arcsecond per pixel. The CCD mosaic for the DECam is shown in Figure 2.3.

The survey will image $\sim$5000 deg^2 of the southern hemisphere sky to unprecedented depth in 5 bands - g, r, i, z and Y. These bands are shown alongside those from other surveys in Figure 1.5 and on their own in Figure 2.4. To succeed in the DES primary science goals the DES filters need to have a very good detection efficiency

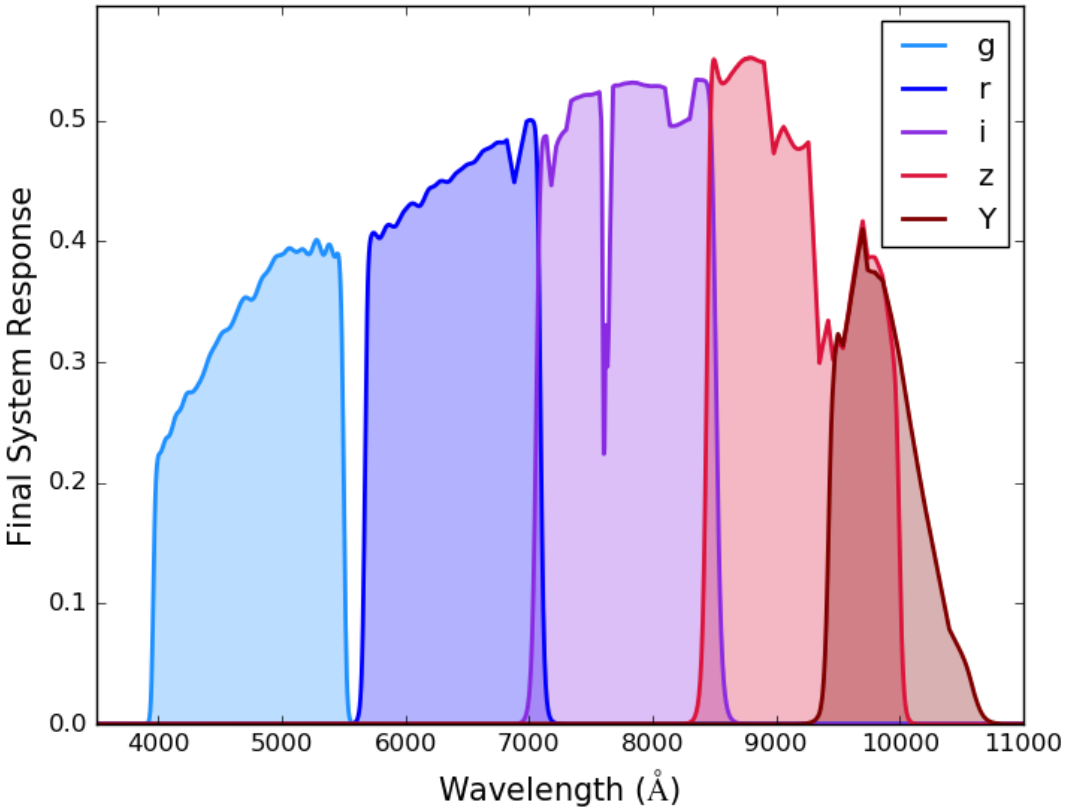

Figure 2.4 The wavelength coverage and system response of the DES filter set.

for high redshift objects. To ensure this the DECam CCDs are very sensitive to the red part of the spectrum. This sensitivity comes from the fully depleted, 250 μm thick detectors which have been developed at the Lawrence Berkeley National Laboratory to be used specifically for DES. The quantum efficiency of these devices in the z band is above 50%, almost an order of magnitude higher than traditional thinned devices. These sensitive detectors also allow the inclusion of the Y band in the same survey, reducing the need for follow up photometry to be taken to confirm redshift quasar candidates. The combination of depth, red sensitivity and area provided by DES, makes it an ideal experiment to use to search for high redshift quasars.

The Sloan Digital Sky Survey (SDSS) is an optical survey predecessor of DES that used a dedicated 2.5m telescope to survey $\sim \frac{1}{3}$ of the sky but primarily in the northern hemisphere. While the data from SDSS are not used directly in this Thesis it is useful to use them to put the DES magnitude limits into context. The SDSS 12^{th} data release (DR12) has 95% completeness for point source limits of 22.2, 22.2, 21.3 and 20.5 for the g, r, i and z bands respectively. This is two magnitudes brighter than the 10σ limiting magnitudes for the DES Y1 release (given in Section 2.2.3) in the i

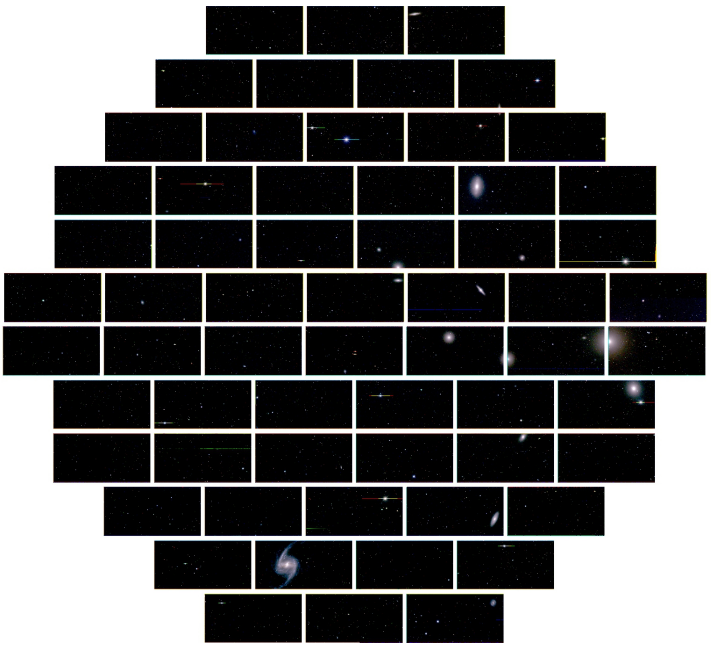

Figure 2.5 Credit: The DES Collaboration. One of the first images taken with the DECam for the DES survey of the Fornax cluster. The gaps in the data arising from the gaps between the CCDs can be seen in this single epoch image.

and z bands, which are the most important for quasar selection at redshifts above 6. This improvement is due to the specialised detectors, the larger telescope and longer integration times (SDSS 53.9 secs, DES 90 secs).

2.2.1 DES Image and Catalogue Data

The single epoch images are reduced and coadded by the DES data management team (DESDM) before being used for catalogue creation and released to the collaboration. An example of a single epoch image is shown in Figure 2.5 where the gaps in the image due to the CCD structure in the camera can be seen. The raw data is reduced using the DESDM processing pipeline which primarily uses the astromatic software suite[2]. The main functions of this software in the pipeline are to perform astrometric calibration using SCAMP (Bertin, 2006) followed by remapping and coadding the single epoch images with SWarp (Bertin et al., 2002) into image tiles which cover the survey area. Once the coadds have been produced catalogue source detection can be done using the SExtractor (Bertin & Arnouts, 1996) image detection software in double image mode. This uses two images; a detection image for source detection and a measurement image from which the objects' properties are measured. The detection image is a χ^2 detection image (Szalay et al., 1999) constructed from the

[2]https://www.astromatic.net/

combination of the r, i and z band images. This image is then used to locate the sources to have their properties measured from the image in each band.

The source catalogues produced by DESDM contain a number of different magnitude types. The ones relevant to this Thesis are described below.

- PSF Magnitudes
  These are point spread function magnitudes where a measurement of the PSF is used to try and account for all the flux from the point source. PSF models for DES are calculated using PSFex (Bertin, 2011) which then feeds them into SExtractor during the catalogue production.

- Model Magnitudes
  This is calculated by fitting a galaxy model to pick up the flux in the extended wings of the object. DES uses an exponential disk model convolved with the local PSF to calculate the model magnitudes.

- Aperture Magnitudes
  An aperture magnitude is calculated from the flux contained within a circular aperture of a given diameter. The DES aperture magnitudes do not correct for flux falling outside of the aperture due to either the morphology of the object or the effects of the PSF.

- Auto Magnitudes
  Auto magnitudes are intended to give the most precise measurement for galaxies but is supposed to also be appropriate for point sources. The SExtractor implementation is based on the first moment algorithm defined in Kron (1980).

The DESDM implementation of SExtractor produces 587 data columns for each object. Many of these parameters were studied for their utility as discriminators in the search for high redshift quasars. It was found that most were not reliable enough to be useful; the only parameters that were used in the selection were the flags. The flags are indicators of untrustworthy data and are detailed fully, in the context of the high redshift quasar search, in Section 3.1.1.

2.2.2 Science Verification Annual Release

The DECam obtained its first light images in September 2012. This was followed by a period of Commissioning and Science Verification (SV) observations lasting between

October 2012 and February 2013. For the work covered in Chapter 3 the Science Verification First Annual Data Release (SVA1) by DESDM was used. The SVA1 observations were designed to reach the full DES survey depth expected after the nominal 5 year survey period. However, the depth across the SVA1 area is non-uniform. Figure 2.6 shows the cumulative area in the DES SVA1 region down to a given 10σ depth in the z-band derived from Mangle (Swanson et al., 2008) based polygon depth maps. These 10σ depth maps are calculated for 2" diameter apertures. These values will depend on the seeing in each polygon and have been converted to PSF magnitudes using the median difference, between mag_{PSF} and mag_{Aper}, for all stellar objects (as defined in Section 4.1). The median of these differences ($z_{PSF} - z_{2"}$) was found to be -0.28 with a σ_{MAD} = 0.066. The σ_{MAD} is related to the standard deviation through σ = 1.4826 x MAD where the MAD is the median absolute deviation and is defined as median($|X_i$ - median(X)|). The MAD is a robust measure of the statistical dispersion of data and is more tolerant of outliers than the direct calculation of the standard deviation. This offset was applied to the magnitude limit calculated as shown in Figure 2.6. As detailed later, a flux-limited sample down to a depth of $z_{PSF} < 21.5$ was used for the high redshift quasar search discussed in Chapter 3, corresponding to a total survey area of 291 deg^2.

2.2.3 Year One Annual Release

The work covered in Chapter 4 uses the Year One First Annual (Y1A1) internal collaboration release of the Dark Energy Survey (DES) data (Diehl et al. (2014), Drlica-Wagner et al. (In preparation)). These data cover $\sim$1840 deg^2 of the southern celestial hemisphere to a median 10σ point source (MAG_PSF) depth in AB magnitudes of 23.28, 23.6, 23.1, 22.3 and 20.8 in the g, r, i, z and Y bands respectively. The point source depths are calculated by adjusting the area weighted median aperture (MAG_APER_4) magnitude limits taken from the DES Mangle (Swanson et al., 2008) products. These are derived for a 2 arcsec diameter aperture and give 10σ depths of 24.2, 23.9, 23.3, 22.5 and 21.2. To convert these aperture depths to point source depths, the median differences between the 2 arcsec aperture magnitude and the PSF magnitude for point sources were used across the survey. The offsets (MAG_APER – MAG_PSF) are g: -0.4, r: -0.3, i: -0.2, z: -0.2, Y: -0.4 with the differences due to the differences in the average point spread function widths induced by seeing for each waveband. See Figure 2.7 for the z band magnitude limit versus cumulative area.

The data contained in the Y1A1 release were taken between 2013 August 15^{th} and 2014 February 9^{th}. The Y1A1 release is shallower than the final survey depth

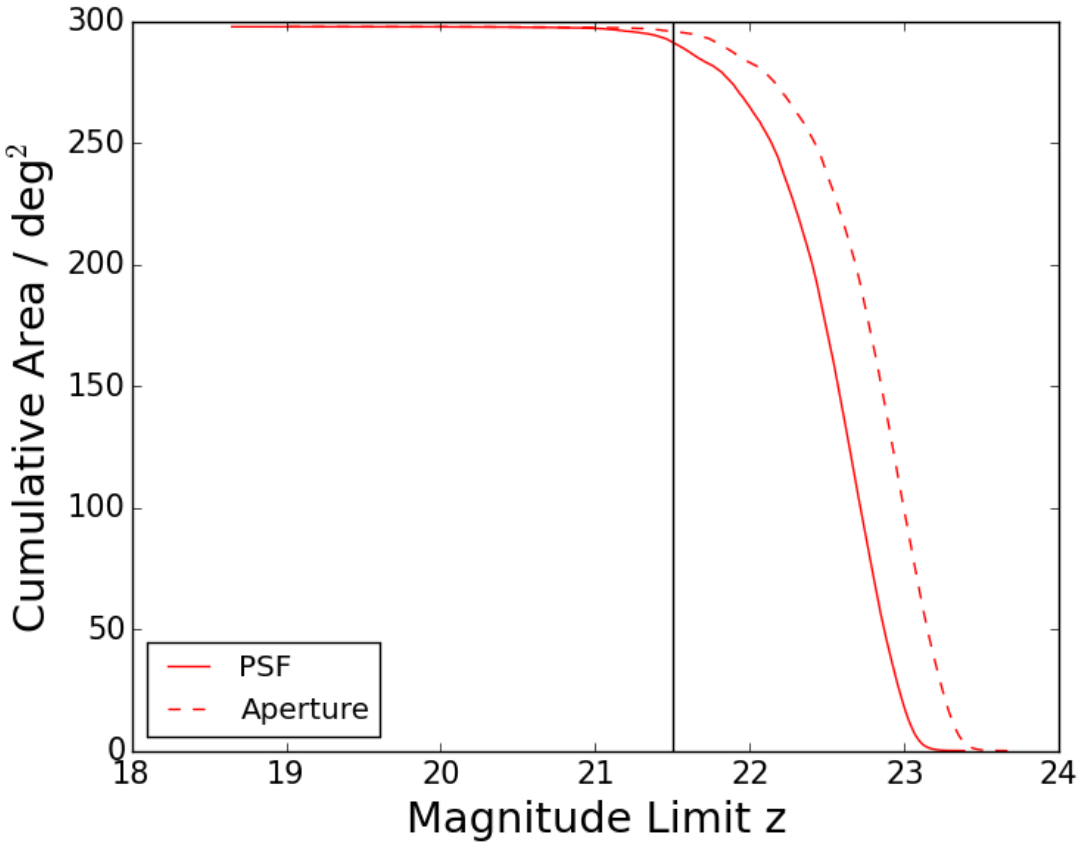

Figure 2.6 Cumulative area versus 10σ z-band depth in a 2 arcsecond diameter aperture and PSF magnitudes for the DES SVA1 data. The aperture magnitudes were converted to PSF magnitudes using the median offset between PSF magnitude and aperture magnitude for point sources from the whole SVA1 dataset. Our magnitude limit of $z_{PSF} < 21.5$ is shown as the vertical line. The aperture magnitude limits were taken from the DES Mangle (Swanson et al., 2008) products.

and consists of 3707 coadded tiles covering two contiguous regions; one overlapping the Stripe 82 area imaged by the SDSS and one overlapping with the area covered by the South Pole Telescope (SPT). The tiles are coadd images made up of between 1 and 5 exposures in each of the 5 wavebands with an average coverage of 3.5 exposures making up each tile.

A magnitude limit of $z_{PSF} \leq 21.0$ corresponds to an area of 1835 deg^2. Figure 2.7 shows the cumulative area against depth for the dataset in 2 arcsec diameter aperture, PSF and auto magnitudes for stellar objects where we define stellar objects based on the definition given in Section 3.1.2. Whilst auto magnitudes are intended to give the most precise estimate of total magnitudes for galaxies they can also be used for stellar objects. The SExtractor implementation of the routine is based on Kron (1980). I do not use auto magnitudes in this Thesis although they are included

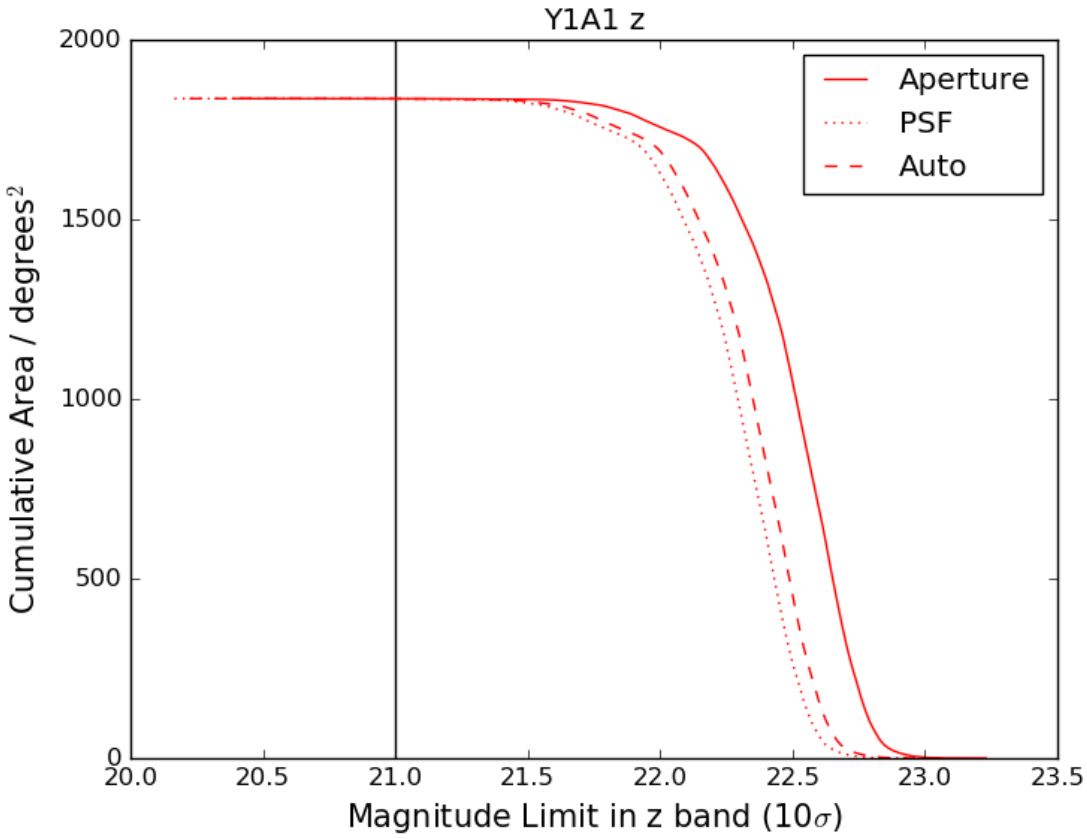

Figure 2.7 Cumulative area versus 10σ z-band depth in a 2 arcsecond diameter aperture (solid line), PSF magnitudes (dotted line) and auto magnitudes (dashed line) for the DES Y1 data. The aperture magnitudes were converted to PSF and auto magnitudes using the median offset between PSF (or auto) magnitude and aperture magnitude for point sources from the whole Y1 dataset. Our magnitude limit of $z_{PSF} < 21.0$ is shown as the vertical line. Auto magnitudes are intended to give the most precise estimate of total magnitudes for galaxies. We do not use auto magnitudes in the analysis and they are included here for comparison with other work.

for comparison with other work noting the small offset for point sources between auto magnitudes and PSF magnitudes, which may indicate a systematic overestimate in the auto fluxes. The z band limit used here is shown as the vertical line and is well above the 10σ limit. As only the DES area covered by VHS as of the 1st February 2014 ($\sim$84%) was used the total area available was reduced to 1533 deg^2. The overlap and location of these two surveys is shown in Figure 2.8.

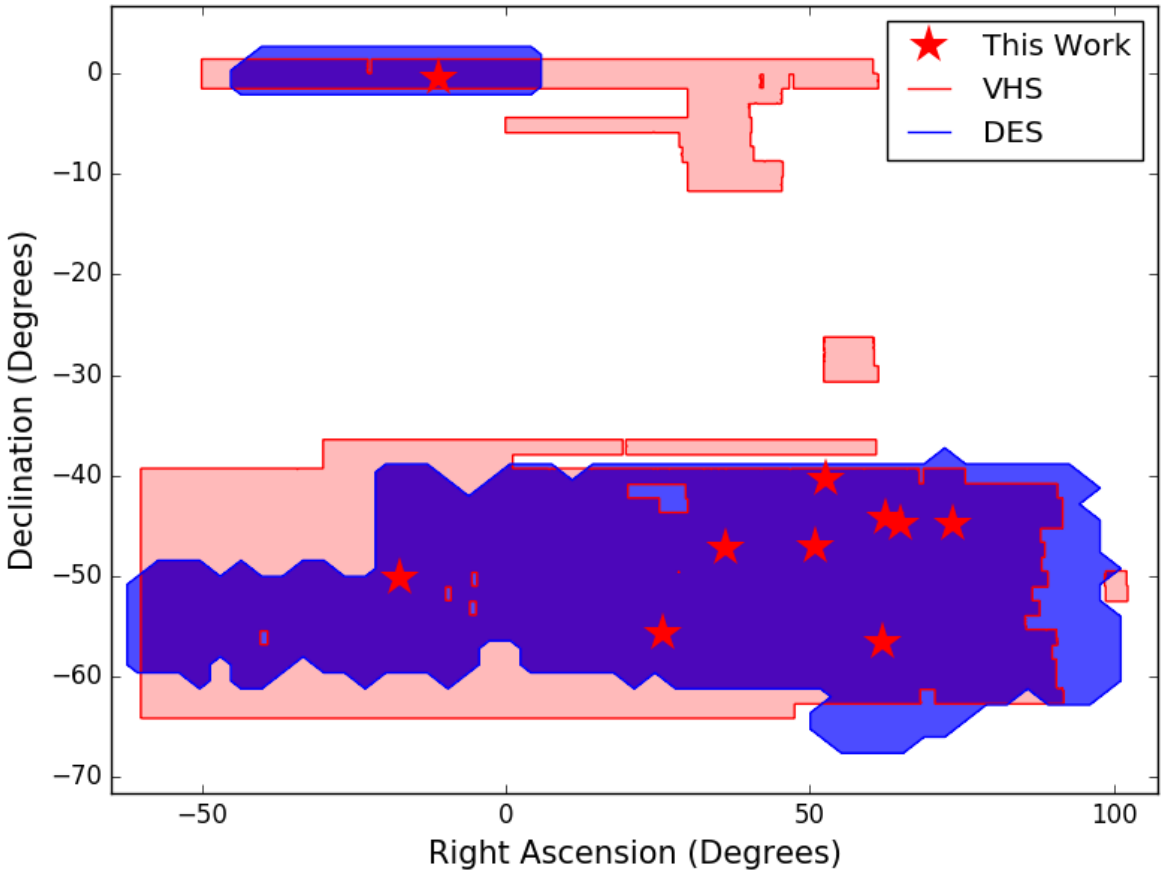

Figure 2.8 The sky coverage of the DES and VHS data used in this work. The blue area shows the DES footprint and the red area shows the VHS footprint. The overlap between the two surveys is shown in purple. The VHS data shown here were taken between 2009 November 4$^{\text{th}}$ and 2014 February 1$^{\text{st}}$. The stars show the positions of the quasars discovered in Section 4.

2.2.4 Year Three Annual Release

The Year 3 (Y3) data release included data taken throughout the previous observing campaigns as well as data taken since the release of the Y1 data to the collaboration. The Y3 data covers an area of $\sim$5000 deg^2 and is shown in Figure 2.9 along with the overlapping VHS data.

When the work in this Thesis was done the Y3 data was not available in its finalised form. Many of the tiles had been reduced multiple times with slightly different versions of the processing pipeline. As it was not obvious which of these reductions was the best, all of the duplicate images were included in the data reduction done in Chapters 4 and 5. These multiple versions of the same image led to duplicate objects in the catalogue, which were removed in the final steps of the selection. The selection methods run on the Y3 data used PSF magnitudes and 2 arcsecond diameter aperture fluxes.

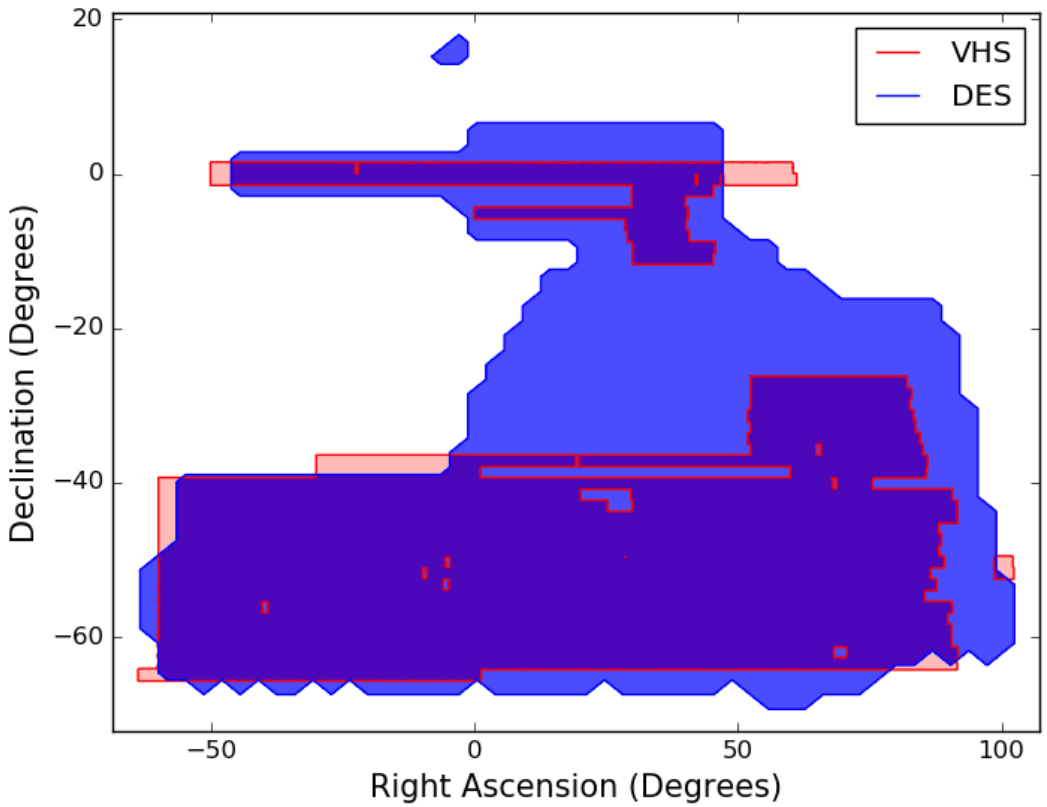

Figure 2.9 The overlap (purple) between the DES Y3 data (blue) and the VHS data (red) used in this selection.

2.3 Wide Infrared Survey Explorer Data

Longer wavelength data at 3.4, 4.6, 12 and 22μm (known as W1, W2, W3 and W4 respectively) were used from the all-sky Wide Infrared Survey Explorer (*WISE*) (Wright et al., 2010). The *WISE* satellite uses a 40cm telescope with a camera containing four 1024 x 1024 arrays with a median pixel size of 2.757 arcsecs and a field of view of 47 x 47 arcminutes. The telescope scanned the sky and took multiple images in all four bands until the coolant ran out. Once the cryogenic fuel was exhausted in 2010 the telescope continued to survey the sky in the two shortest bands as part of the post-cryogenic *NEOWISE* mission phase. The two datasets were combined into the 2013 *WISE* AllWISE Data Release giving coadd 5σ point source depths of $W1_{\rm AB}$ = 19.6, $W2_{\rm AB}$ = 19.3, $W3_{\rm AB}$ = 16.7 and $W4_{\rm AB}$ = 14.7. The coadd images have FWHM of 6.1, 6.8, 7.4 and 12.0 arcsecs in the W1, W2, W3 and W4 bands respectively. The AllWISE coadd images are 4095 $\times$ 4095 pixels at 1.375 arcsec per pixel. The W1 and W2 filters that are used in this Thesis are shown in Figure 2.10.

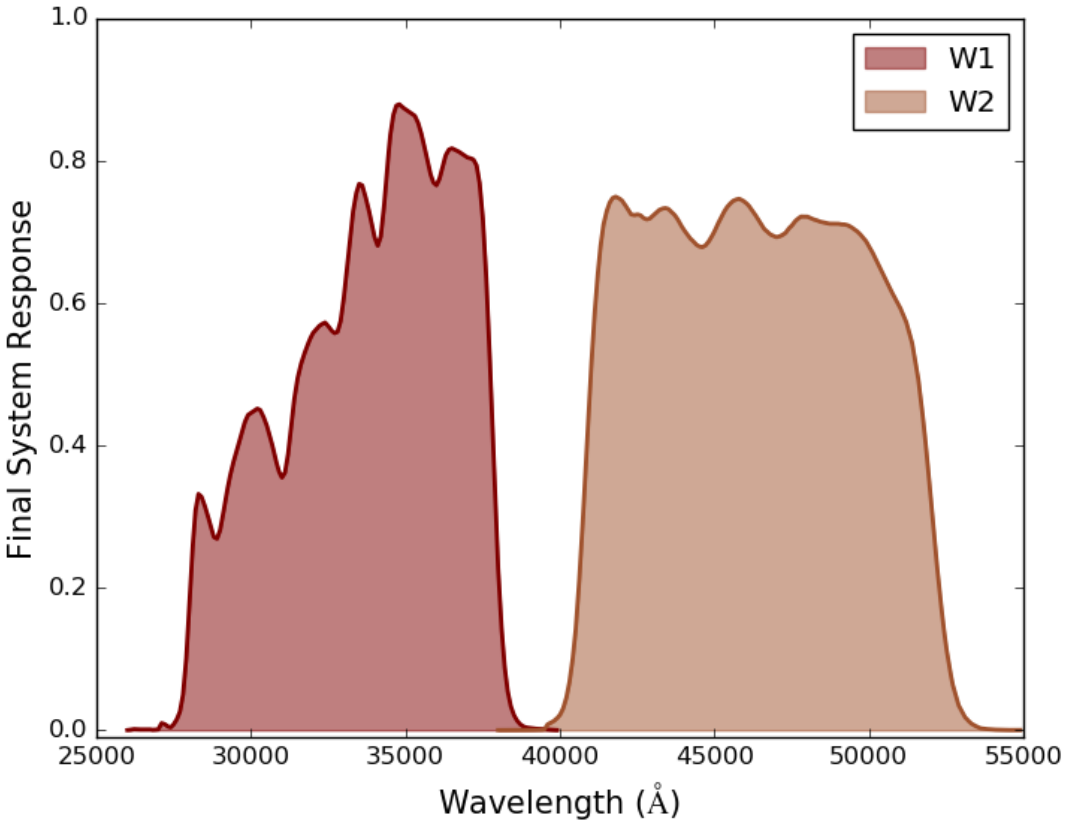

Figure 2.10 The wavelength coverage and system response of the WISE filter set.

The Vega to AB conversions for the ALLWISE data are $W1_{AB} = W1_{Vega} + 2.699$ and $W2_{AB} = W2_{Vega} + 3.339$ which are given in Jarrett et al. (2011) and in the *ALLWISE* explanatory supplement. [3]

[3]The *ALLWISE* explanatory supplement, (continued on next page) http://wise2.ipac.caltech.edu/docs/release/allwise/expsup/sec5_3e.html, directs the reader to the *WISE All-Sky* explanatory supplement for the conversions; http://wise2.ipac.caltech.edu/docs/release/allsky/expsup/sec4_4h.html#summary.

3

Discovery of the First z $\geq$ 6 Quasar from the Dark Energy Survey

As discussed in Section 2.2 the Dark Energy Survey (DES) will provide an important dataset to search for quasars at z $\geq$ 6.0 due to the large area ($\sim$ 5000 deg^2) covered and the redder sensitivity of its detectors compared to previous surveys such as SDSS.

In this Chapter the process that lead to the discovery of the first quasar from DES is described. The discovery of the first quasar is an important test of the validity of the selection method, the quality of the data and the suitability of the data for the purpose of finding high redshift quasars.

Initially an area of $\sim$300 deg^2 was released to the collaboration in the form of the Science Verification (SV) data. This data, combined with data from the VISTA Hemisphere Survey (VHS) and the Wide-Field Infrared Survey Explorer (WISE) telescope, provided a good dataset to develop and test high redshift (z > 6) quasar selection methods. The datasets used are detailed in Chapter 2.

3.1 Quasar Candidate Selection

At redshifts $\geq$ 6 quasars have very distinctive spectral features shortward of the Lyα emission line caused by absorption due to neutral hydrogen in the intergalactic medium in front of the quasar. The observed frame optical colours of high redshift quasars are influenced by this absorption and the redshifting of the Lymanα line. Figure 3.1 shows an example spectrum of a z = 6.21 quasar discovered as part of the work detailed in this Thesis. In this spectrum you can see the characteristic flux deficit blueward of the redshifted Lyα emission line. The absence of flux at short wavelengths

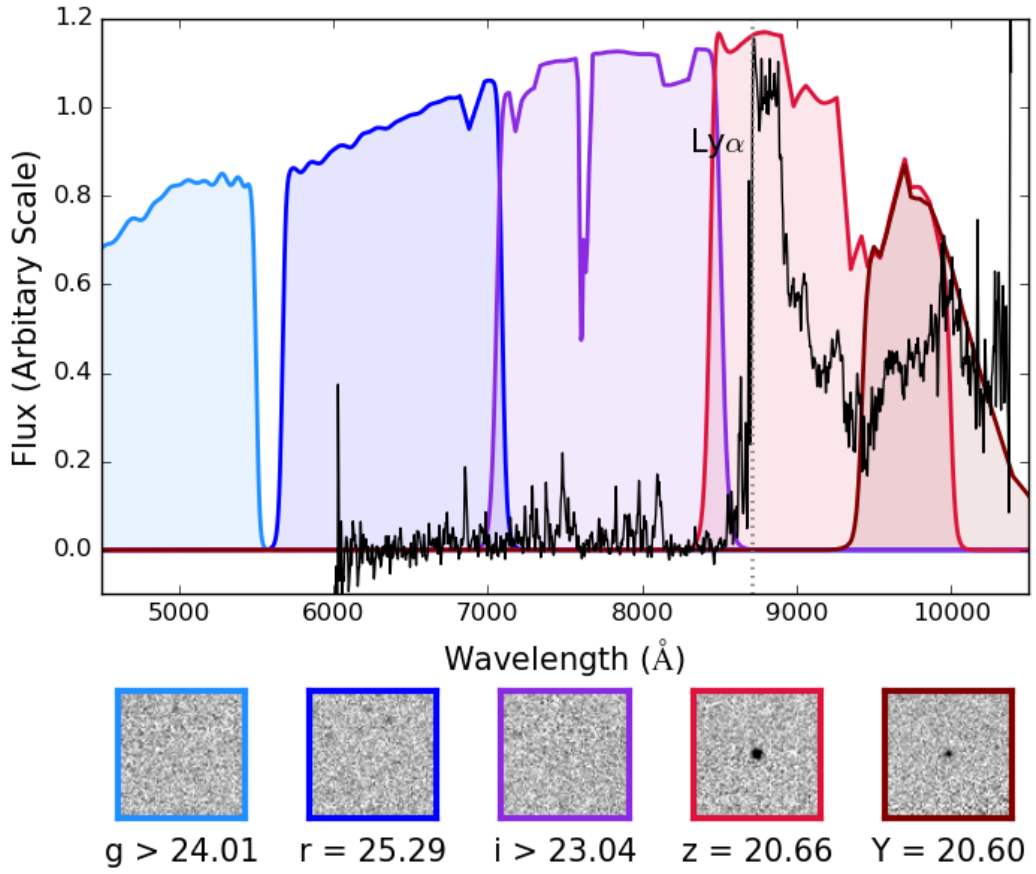

Figure 3.1 The top panel shows a spectrum of a z = 6.21 quasar discovered during the work discussed in Chapter 4. The Lyα line is marked with a grey dotted line and the flux deficit blueward of this can be easily seen. The shaded areas show the DES system response in each band and the colours correspond to the borders of the image cutouts below which show the photometric data for this object in each band. These cutouts are 20 arseconds across.

followed by the sharp increase at the redder end of the spectrum gives rise to the photometry illustrated in the cutout images below the spectrum. There the object can be clearly seen in the z and Y bands but not at all in g, r or i.

The distinctive photometry of high redshift quasars means they can be selected using a drop out technique which searches for objects that are much brighter in one band than the other. At z $\sim$ 6 this dropout is between the i and z bands leading to very red i - z colours. This was first used in (Fan et al., 2000) and developed further here to find the first high redshift quasar from DES. In this Chapter the selection method used to find the first DES high redshift quasar is outlined. In this analysis all magnitudes are PSF unless otherwise stated.

Table 3.1 A summary of the imaging flags produced by SExtractor.

Value	Description
1	The object has neighbours, bright and close enough to significantly bias the MAG AUTO photometry, or bad pixels (more than 10% of the integrated area affected)
2	The object was originally blended with another one
4	At least one pixel of the object is saturated (or very close to)
8	The object is truncated (too close to an image boundary)
16	Object's aperture data are incomplete or corrupted
32	Object's isophotal data are incomplete or corrupted
64	A memory overflow occurred during deblending
128	A memory overflow occurred during extraction

3.1.1 Exploratory Data Analysis

High-redshift quasar and other rare object searches are often contaminated by a large number of artefacts. These spurious sources often dominate outlier regions of colour space that are also populated by smaller numbers of real objects. In fact it is safe to assume that most outliers in an unfiltered catalogue are junk (such as imaging artefacts, cosmic rays and saturation effects). The first step therefore involved artefact removal at the catalogue level. This required investigating and understanding the response of the processing pipeline to these artefacts and finding out if the flagging in the catalogue could be trusted.

Flags

The internal bitwise flags that are produced by SExtractor are given in Table 3.1. These values were taken from the SExtractor documentation. The utility of bitwise flags is that they can be uniquely combined to attribute multiple properties to a value, for example an object flagged as 1 and 2 would be a 3.

These flags are produced for each band and are included in the DES DM database products. As high redshift quasars do not have flux in all of the bands they can be flagged incorrectly, inconsistently and unreliably.

A large number of objects with different values in both the weight flag and the imaging flag were studied to understand the best way to use these flags. Figure 3.2 shows examples of objects that are flagged with a value of 3 (1 + 2) in the DES imaging flags. As can be seen most of these objects are junk rather than valid candidates. The left-most cutout shows an object that is undetected in that band which is exactly the

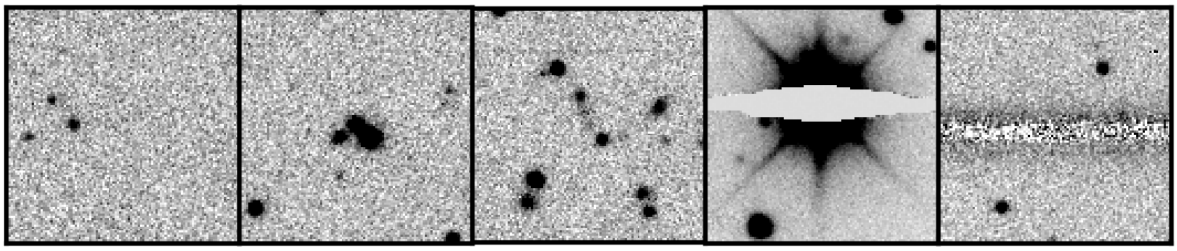

Figure 3.2 All of the objects shown here are flagged with a 3 in the DES flags. It can be seen that all of these objects have very different problems with them and that the first cutout shows an object that we would want to keep in if it looked like that in the g or r band. These cutouts are 30" by 30" and all taken from the z band images. The flagging was found to be similar across all the bands and objects shown here have many analogues in the other bands.

sort of object that should be kept, in the g and r bands, as it corresponds to a high redshift quasar candidate. The weight flags were then used to distinguish between objects that were undetected and those that were contaminants. It was found that non detections were flagged as clean in the weight flags but that the artefacts were not. This led to the criteria that objects that were flagged by the DES data management SVA1 pipeline as 1, 2 or 4 (flag definitions are given in Table 3.1) were provisionally labelled as junk. If they were also flagged as having at least one low-weight pixel in the measurement image within the isophotal footprint or in the filtered detection image then this was confirmed and they were removed. The number removed by the flag cuts (3,170,496), and at every other step, is given in Table 3.2.

Once the list had been cleaned up as far as it could be using the fast catalogue based steps a flux limited sample was created down to a magnitude limit of $z_{PSF} \leq 21.5$ and $\sigma_z < 0.1$. Colour, magnitude and error cuts were then applied to this list.

3.1.2 Catalogue Based Selection

Once a clean, flux limited sample had been produced a variety of astrophysically driven catalogue based steps were used to narrow down the list. The list was first narrowed down to point sources as quasars are expected to be point sources. Objects were required to satisfy:

$$z_{PSF} - z_{model} < 0.145 \tag{3.1}$$

which is the star-galaxy classifier defined in the SDSS photometric survey (Stoughton et al. (2002)) and SDSS quasar selection (Richards et al. (2002a)). This star-galaxy separation criterion is shown in Figure 3.3. The stellar locus is clearly situated at $z_{PSF} - z_{model} \sim 0$. It can be seen that the star-galaxy separation starts to become less reliable at fainter magnitudes but the stellar locus is still clearly visible down to z < 21.5, which is the flux limit imposed on our sample.

The primary selection step used was an i - z colour criterion, which was based on the selection used by Fan et al. (2001). The Fan et al. (2001) SDSS selection of i - z > 2.2 was transformed onto the DES filter system as follows. First point-like objects were selected in the area of overlap between the DES and SDSS surveys. Point sources were defined as those having $z_{PSF} - z_{model} < 0.145$. The DES and SDSS sources were matched using a radius of 2.16 arcseconds (0.006°). A least squares linear fit was then carried out on a running median of the colours. A window size of 50 was used for the median and the data were sorted by $(i-z)_{SDSS}$ and then sparsely sampled along the $(i-z)_{SDSS}$ direction with a stride of 10 to determine the colour-term between the two surveys:

$$(i-z)_{DES} = 0.72(i-z)_{SDSS} + 0.111 \tag{3.2}$$

Based on this and the Fan et al. (2001) selection criterion an equivalent colour criterion of $(i-z)_{DES} > 1.694$ was derived.

After this the colour cut derived was applied to select red objects. As quasars have no obvious flux in the g or r bands, shown in Figure 3.1, a requirement that $g_{PSF} > 23.0$ and $r_{PSF} > 23.0$ was imposed. These limits were chosen as they ruled out almost all of the objects that were reliably detected without removing undetected sources in regions of particularly deep photometry. When the candidate list was visually inspected after this step it was found that there were a few objects that were very faint in the g or r band but were in a very deep part of the survey and still had a reliable detection in these bluer bands. To remove these detected objects an error threshold of σ_g and $\sigma_r > 0.1$ was used. i.e. Objects with σ_g and $\sigma_r \sim 0.2$ (5σ detections) are retained since there is a finite probability that they have zero flux. Examples of these objects are shown in Figure 3.4.

The cut of $\sigma_{g/r} > 0.1$ was used as it was empirically found from the data that this was a good balance between keeping a few faint objects and not throwing away objects that were falsely detected in g or r. Positive noise at the site of the object can cause SExtractor to register a magnitude for the object when there is not a clean detection. This is shown in the cutouts in Figure 3.5. As high redshift quasars are unlikely to be detected in the g or r bands it is important that objects with a false

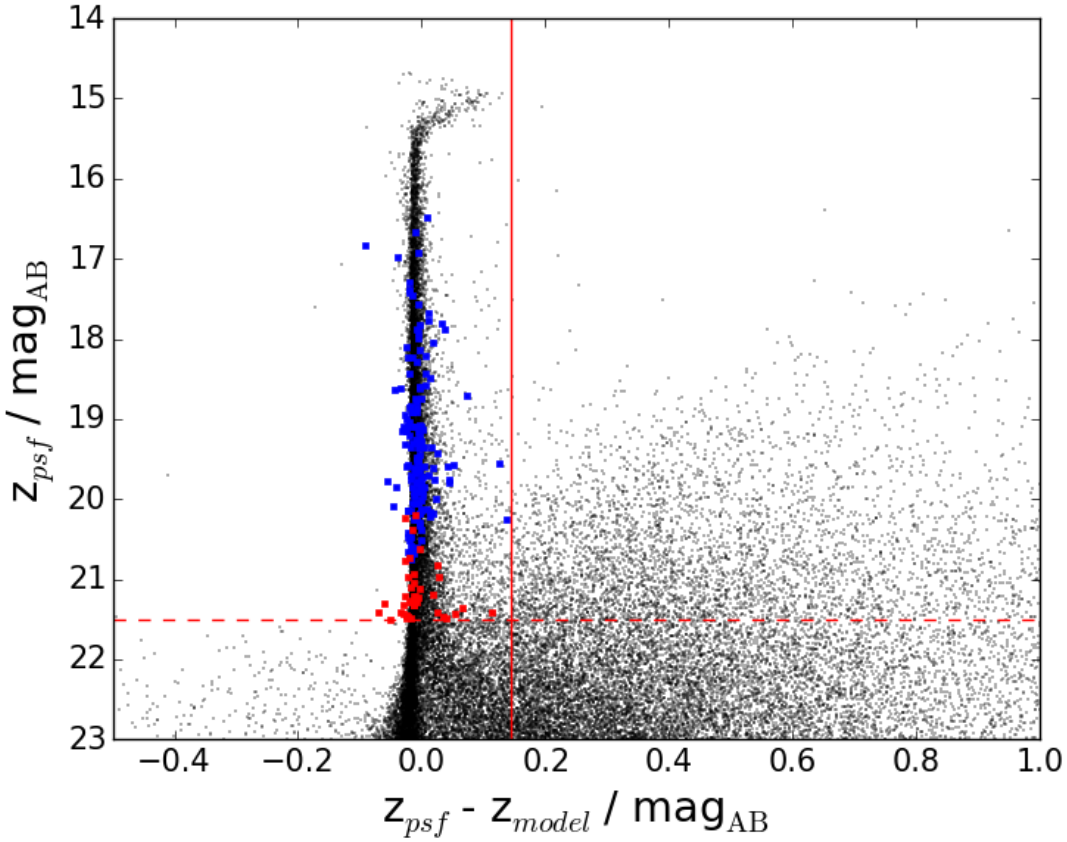

Figure 3.3 The black points are all the objects on one tile from the survey and the red points show the quasar candidates after the final stage of the selection in section 4.1. A clear locus can be seen at 0.0 on the horizontal axis. The blue points are known quasars taken from the catalogue given in Véron-Cetty & Véron (2010) with z > 2.0. Below this redshift host galaxy contamination can occur. The median of the Veron 2010 sample is 0.015 and the σ_{MAD} = 0.052. The solid vertical line shows the cut used to select point sources. The dashed horizontal line shows the magnitude limit used.

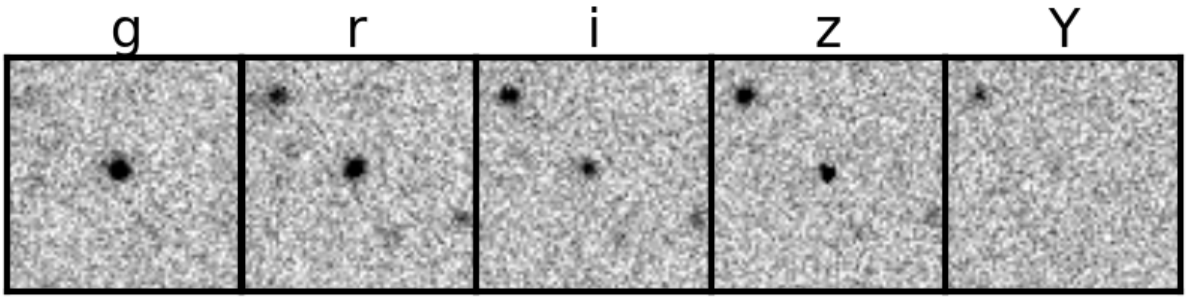

Figure 3.4 In these cutouts an object is shown with g_{PSF} = 23.16 ± 0.03 and r_{PSF} = 23.02 ± 0.03. The source is obviously detected in the g and r band despite having a magnitude below our limit.

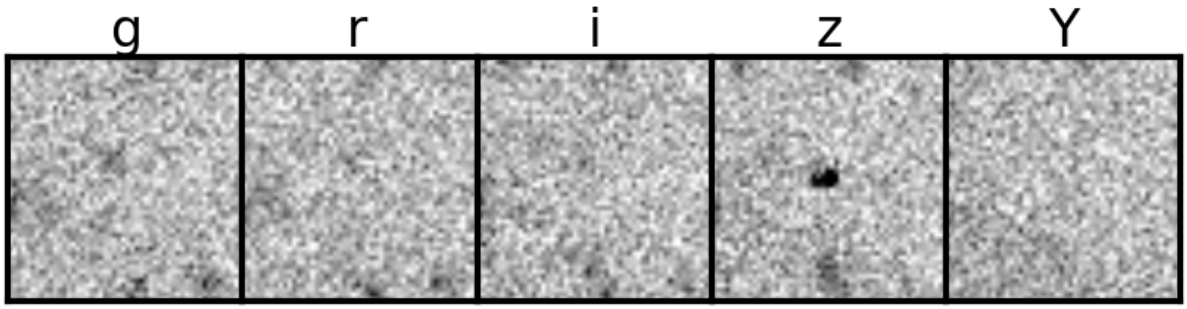

Figure 3.5 This object has no discernible flux in the g band but a catalogue entry of $g_{PSF} = 24.88 \pm 0.15$. In the r band the object appears visually similar to in the g band but has been assigned a magnitude of 99 as a flag for missing or negative flux. Due to their only being noise at the position of the object there is a chance there will be a small amount of positive or negative flux at this position, these two situations are treated differently by the catalogue despite being visually similar. This demonstrates how the selection technique for dropouts has to take into account the multiple ways of treating objects at the detection threshold.

detection in g or r are kept.

The main astrophysical contaminants of high redshift quasar searches are cool stars, such as L and T dwarfs, in our own Milky Way. These were removed using a colour cut of $z_{PSF} - Y_{PSF} < 0.5$. Figure 3.6 shows a cool star spectrum and its corresponding imaging. This shows how a cool star can mimic a high redshift quasar. Due to the continual increase in the stellar spectrum the z - Y colour is much redder than the predicted quasar colours in the absence of significant reddening.

The colour selection can be seen in Figure 3.7 which shows the cool dwarf locus clearly distinct from the selection box in terms of the z-Y colour. This z - Y cut will also potentially remove higher redshift objects with z > 6.5 at which point the Lyα emission line begins to move into the Y band making the z - Y colour redder. This method is not designed to pick up these higher redshift objects and selection of these will be discussed in Chapter 5.

At this stage many of the objects left were bright artefacts in the z band which were not present in any of the other bands. To limit the numbers of these that were present in the sample two Y band magnitude cuts were used. First objects with bad Y band photometry ($Y_{PSF} = 99$) were removed and then those with $Y_{PSF} > 23.0$. These cuts ensured that objects were detected in the Y band as well reducing their likelihood of being a z band artefact or moving object that was only in that position at the time of the z band image. Moving objects can contaminate the selection in this way as the DES images are not contemporaneous, meaning that objects can be present in only one waveband as they have moved between the exposures. These Y band requirements

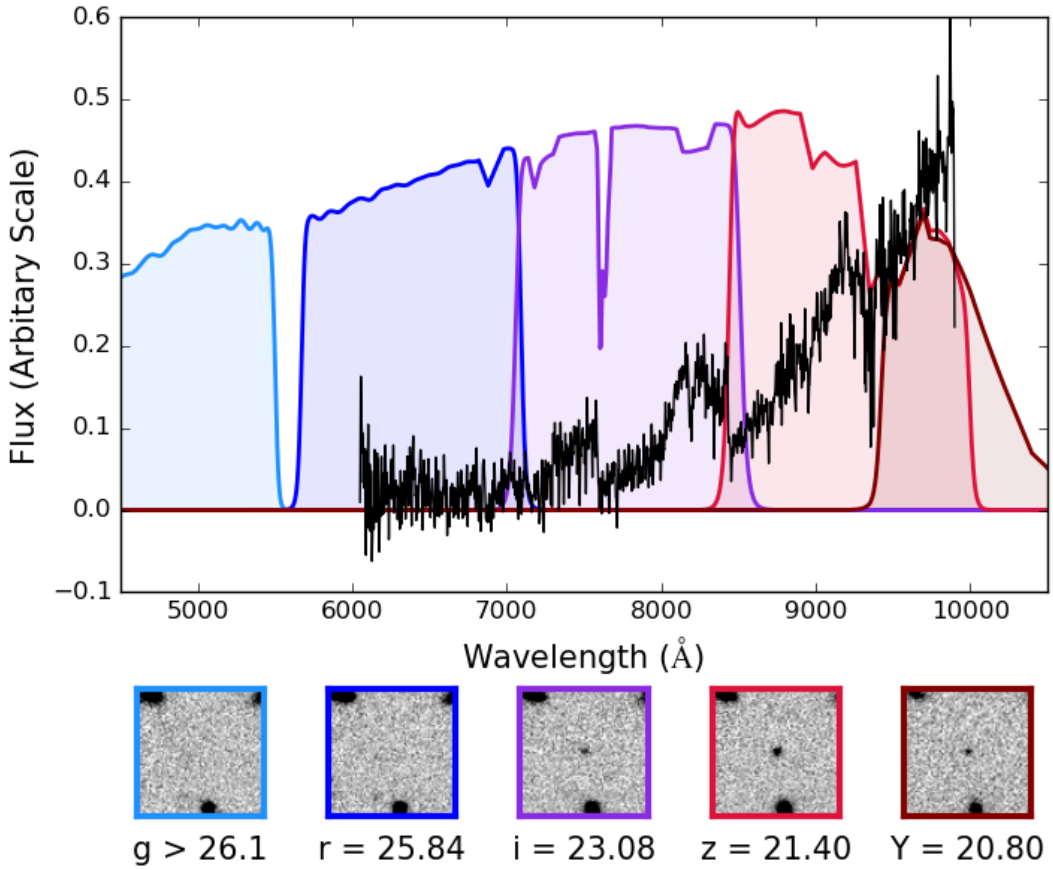

Figure 3.6 The top panel shows a spectrum of a cool star. The spectrum shows the increasing flux that can mimic a high redshift quasar in colour space. The shaded areas show the DES system response in each band and the colours correspond to the borders of the image cutouts below which show the photometric data for this object in each band. These cutouts are 20 arseconds across.

removed 9231 objects from the list.

3.1.3 g and r Band Detections

Once the catalogue based steps had been run the remaining candidates were visually inspected. During this it was found that many of these objects had a $g/r_{PSF} = 99$ (which can mean a non detection) but were actually very bright, saturated objects. An example of this is shown in Figure 3.8.

The object in Figure 3.8 has the same r band magnitude in the DES catalogue as the object shown in Figure 3.5. To remove these bright objects a crude version of listdriven (aperture photometry performed at predefined positions) forced photometry was applied on the r bands images. For each object we identified the brightest pixel in a box of 3x3 pixels centred on the position of the object and required that it was no

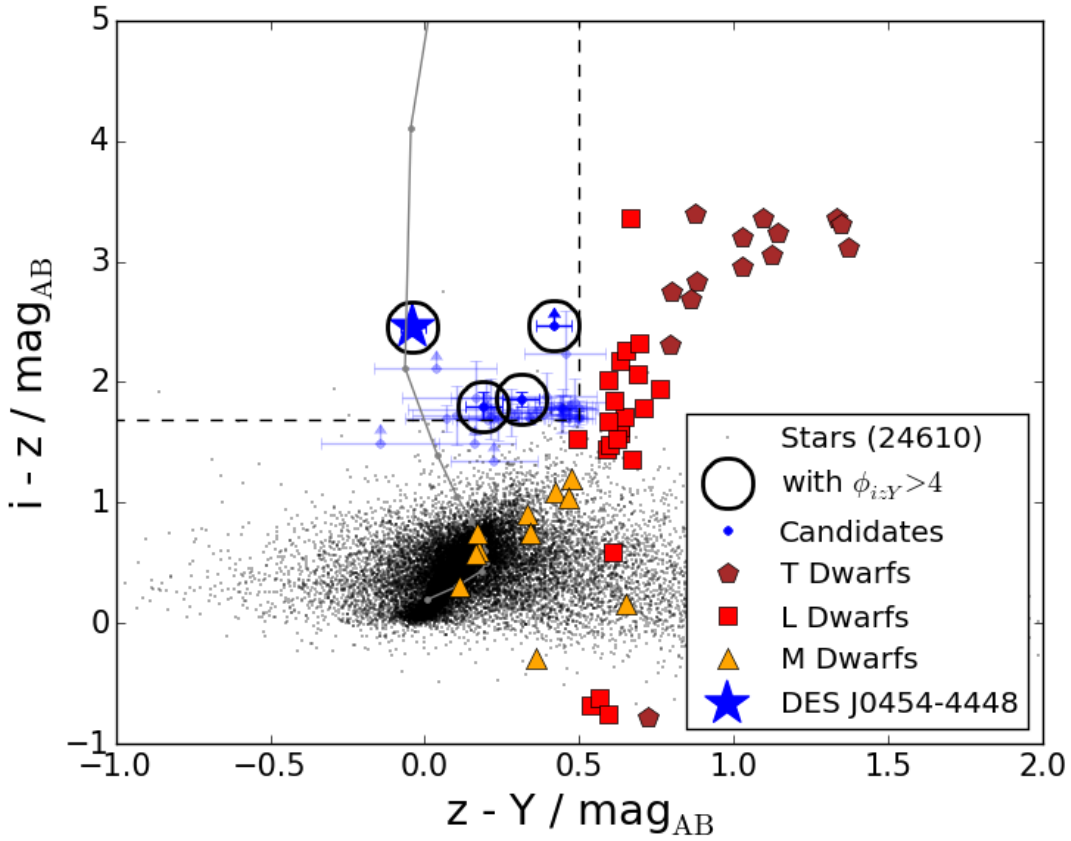

Figure 3.7 The black points represent all objects that have $z_{PSF} - z_{model} < 0.145$ and are detected in the i, z and Y bands from one tile of the survey. The blue points are the candidate objects that satisfy the first 11 steps of the selection criteria. The objects that pass the final step are circled while the others are faded. The blue star shows the location of the confirmed quasar. The grey line shows a simulated quasar track starting from z = 5 and incrementing by 0.1 to z = 6.4. Objects that have i = 99 (are undetected in the i band) pass the selection criteria and are here plotted with arrows to indicate that they are lower limits in i-z. The objects outside the selection box are limits in the i band where the survey is particularly shallow. Many of the objects are situated at the lower right of the selection box which suggests that they are cool stars scattered in by random photometric errors. This is supported by the large errors that many of them have which overlap the selection box edges. The red, orange and brown points are known brown dwarfs found with UKIDSS and converted using their spectra and the DES band passes.

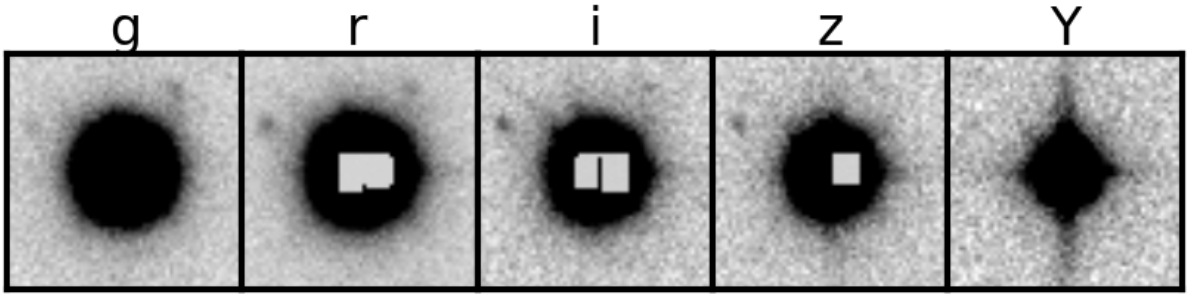

Figure 3.8 Here an object which has saturated in the r, i and z bands is shown. While it is obviously present in all the bands its PSF magnitudes are 99. This object has g_{PSF} = 99.0 $\pm$ 1.0, r_{PSF} = 99.0 $\pm$ 1.0, i_{PSF} = 99.0 $\pm$ 1.0 and z_{PSF} = 14.7326 $\pm$ 0.0001 which makes it look like a viable high redshift quasar candidate.

more than 10 analog to digital units greater than the median value in a 30 arcsecond box around the object.

This threshold was derived from looking at the σ_{MAD} and the background level of the images in the data release. The background level was calculated by taking the median of a 30 arsecond box around the object. A threshold of 10 corresponds roughly to three times the median σ_{MAD} (3.06) above the median background level of the images (0.147). A conservative threshold of 10 was used to filter these bright objects to ensure that any faint objects which may correspond to high-redshift quasars, were not removed. As the difference in flux values for these corrupt objects and the genuine non detections is very dramatic and the r band magnitudes were not required a complicated method of accurate forced photometry was not needed.

3.1.4 Cosmic Ray Removal

The next most common contaminant that remained at this stage was cosmic ray detections in the z band. A cosmic ray hit in the z band can cause an object to pass the selection criteria as it looks like a very extreme i - z dropout. An example cosmic ray detection is shown in Figure 3.9, this shows the irregular shape of the detection. The first step in removing these objects was to require the objects to have a Y band magnitude. As the Y band data is shallower and more variable than the other bands no error cut was used. This retained objects that were false detections in the Y band (such as the object in Figure 3.9 which has Y_{PSF} = 20.54 $\pm$ 1.0) and the candidate list was still swamped with cosmic rays. These were removed based on the differences between adjacent pixels (as a proxy for the local pixel gradients) as a cosmic

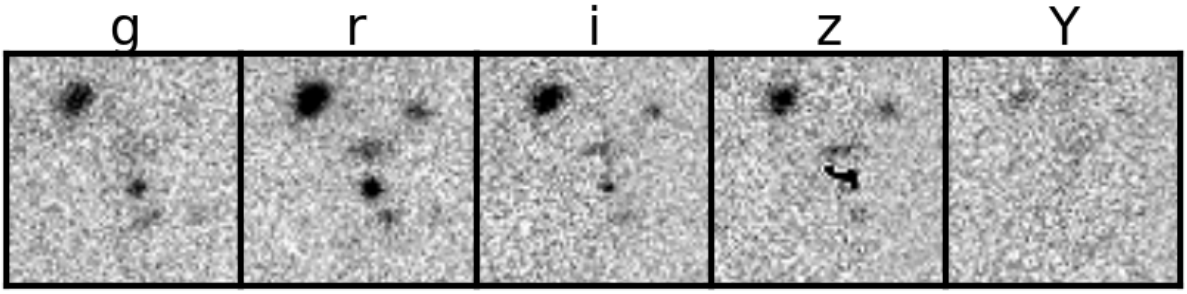

Figure 3.9 Cosmic ray hits in the z band create objects that pass the selection due to looking like extremely red i - z dropouts. These cutouts show the odd shape of the cosmic ray as well as demonstrating that they are not smoothed out by the PSF.

ray would be more abrupt in terms of its pixel gradient than a real object. In later DES data releases a new method of cosmic ray rejection was included in the pipeline processing and this step was no longer necessary.

3.1.5 Visual Inspection and Ranking

The above steps (including the numbers removed in each stage) are summarised in Table 3.2. Following these steps there were few enough candidates to cut down by systematic visual inspection. The visual inspection stage removed spurious sources such as cosmic rays, satellite trails and diffraction spikes. At the end of this stage we have 43 candidate high-redshift quasars. These were then ranked candidates based on an error weighted photometric selection metric for follow up spectroscopy. The selection metrics φ_{iz} and φ_{zY} combine to give φ_{izY} which essentially constitutes a error-weighted measure of how far into the colour-selection box, shown in Figure 3.7, each candidate lies.

$$\varphi_{iz} = \frac{(i_{PSF} - z_{PSF}) - 1.694}{\sqrt{i_{err}^2 + z_{err}^2}} \tag{3.3}$$

$$\varphi_{zY} = \frac{0.5 - (z_{PSF} - Y_{PSF})}{\sqrt{z_{err}^2 + Y_{err}^2}} \tag{3.4}$$

$$\varphi_{izY} = \sqrt{\frac{\varphi_{iz}}{|\varphi_{iz}|}\varphi_{iz}^2 + \frac{\varphi_{zY}}{|\varphi_{zY}|}\varphi_{zY}^2} \tag{3.5}$$

For those sources undetected in the i band, the i band magnitude limit at the source position was used instead in the computation of φ_{iz} and the error set to 0.2. An error

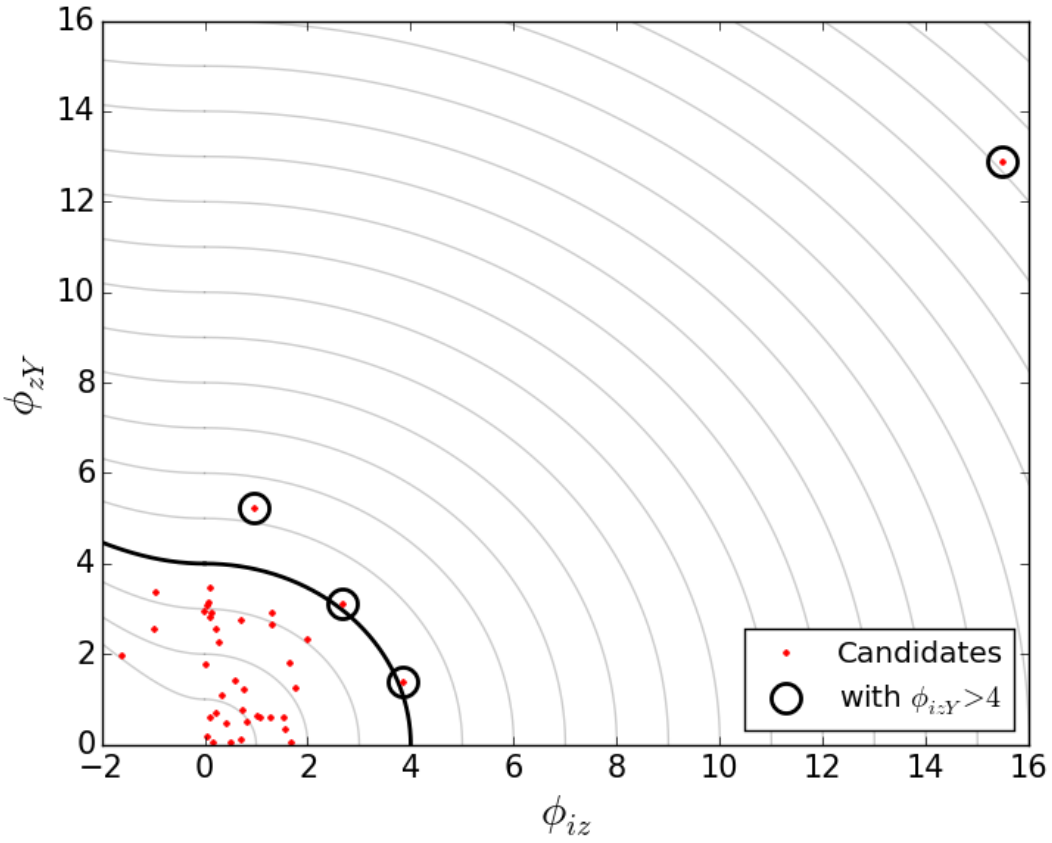

Figure 3.10 The φ_{izY} selection metric. Here the x axis is the φ_{iz} defined in equation 3.3 and the y axis is φ_{zY}. The four objects with $\varphi_{izY} > 4$ are circled and the object that was confirmed as a quasar has the highest value of both Φ_{iz} and Φ_{zY} in the Figure.

of 0.2 was used as it corresponded roughly to the median error of objects which were detected at the median magnitude limit.

This selection led to prioritising four of the 43 candidates as highly viable high-redshift quasar candidates with $\varphi_{izY} > 4$ from the 291 deg^2 region. The distribution of φ values can be seen in Figure 3.10 where the four candidates have been circled. One of these candidates clearly has much larger values of φ than the other three and this object (DES J0454-4448) with $z_{AB} = 20.2$ was therefore selected for follow up spectroscopy as the most promising first high-redshift quasar candidate from the DES data. DES J0454-4448 is shown across the DES and VISTA bands in Figure 3.11. In these cutout images the absence of flux in the g and r bands can be clearly seen along with the increase in brightness from the i to z bands.

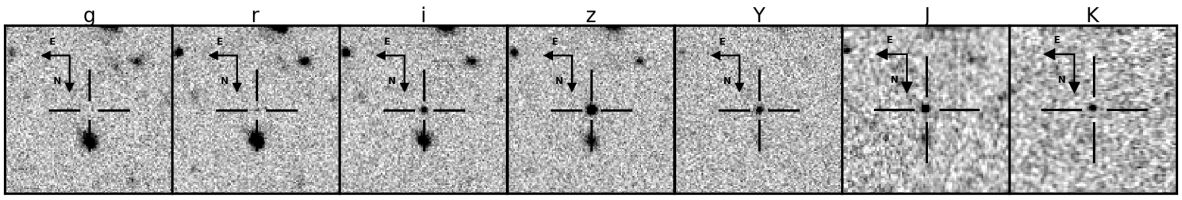

Figure 3.11 Cutouts of the spectroscopically confirmed quasar, DESJ0454-4448 in each of the DES (g, r, i, z and Y) and VHS (J and K) wavebands. The boxes are 30" across and the quasar is the central object.

Table 3.2 Summary of the steps in the high-redshift quasar selection process

Step	Description	Number Removed	Number Remaining
	Number of objects in database		40,129,963
1	Flag criteria	3,170,496	36,959,467
2	$z_{PSF} \leq 21.5$ and $\sigma_z < 0.1$	29,760,121	7,199,346
3	$z_{PSF} - z_{model} < 0.145$	2,409,240	4,790,106
4	i_{PSF} - $z_{PSF} > 1.694$	4,766,589	23,517
5	g_{PSF} and $r_{PSF} > 23.0$	12,985	10,532
6	σ_g and $\sigma_r > 0.1$	371	10,161
7	z_{PSF} - $Y_{PSF} < 0.5$	92	10,069
8a	Y_{PSF} not equal to 99	8725	1344
8b	$Y_{PSF} < 23.0$	506	838
9	Forced photometry in r band	372	466
10	Cosmic ray removal	489	77
11	Visual Inspection	34	43
12	$\varphi_{izY} > 4$	39	4

3.2 DES J0454–4448

The photometric data for DES J0454-4448 is summarised in Table 3.3. This includes the DES photometry (g, r, i, z and Y) as well as infrared magnitudes from the VISTA Hemisphere Survey (J and K) and the *AllWISE* data release of the *WISE* All-Sky Survey (Wright et al., 2010) (W1 and W2). Blain et al. (2013) have studied the infrared *WISE* colours of known high-redshift quasars finding that they are typically bluer than the $W1_{AB}$ - $W2_{AB} > 0.16$ selection cut used to select lower redshift AGN such as in Stern et al. (2012). The colour ($W1_{AB}$ - $W2_{AB}$ = 0.05) of this object supports this and agrees with the locus of known high redshift quasars matched to the WISE data. The colour also agrees with the predicted track in Assef et al. (2010) as shown in Figure 3.13. As the resolution of WISE (6.1" and 6.4" in W1 and W2 respectively) is quite large compared to the separation of the object and its nearest neighbour (4.89") it is

debatable if the magnitude corresponds solely to the quasar.

Spectroscopic follow up of DESJ0454-4448 was conducted using the Magellan Echellete (MagE) spectrograph (Marshall et al., 2008) on the 6.5m Clay telescope at the Las Campanas Observatory in Chile. Two 10 minute exposures were taken on the night of December 2nd 2013 in variable conditions. George Becker reduced the data and combined the one-dimensional spectrum using a custom set of IDL routines. The discovery spectrum for the quasar can be seen in Fig. 3.14.

Measuring the quasar redshift from emission lines in the present spectrum is difficult due to the strong attenuation of Lyα ($\lambda_{\rm rest}$ = 1215.67Å) and the modest quality and limited wavelength range of the data which does not cover the wavelength range to detect CIV (1549Å) or SiIV+OIV] (1400Å) which at z $\geq$ 6.00 have observed wavelength that $\lambda \geq 9800$Å. Therefore the apparent onset of the Lyα forest absorption was used to estimate the redshift. This approach has been previously used for weak lined quasars such as BL Lac objects (Danforth et al., 2010).

A series of absorption lines appears over 8530 $\lesssim \lambda \lesssim$ 8630 Å, which is interpreted as the expected Lyα absorption in the quasar's near zone. The reddest of these lines falls at 8626 Å, which corresponds to a Lyα redshift of z = 6.096. There is a tentative detection of the quasar's SiII 1260Å emission line with a peak wavelength near 8920 Å, though it is contaminated by skyline subtraction residuals, corresponding to a redshift of 6.077. Combining these estimates gives a mean redshift and standard deviation: z = 6.09 $\pm$ 0.01. To reflect the systematic uncertainty in the redshift we follow Fan et al. (2006a) and adopt an total uncertainty of 0.02 to take account of the observed offsets in redshifts between low and high ionization lines in quasars.

The quasar continuum is strongly attenuated at $\lambda \leq$ 8530 Å. Following the method outlined in Fan et al. (2006b), we take the edge of the near zone to be the point where the ratio between the continuum flux and the spectrum first falls below 0.1 blueward of the Lyα emission line. Here the intrinsic continuum is roughly estimated using a composite from low-redshift SDSS spectrum (as used in Mortlock et al. (2011)) normalized to the flux between 1268Åand 1295Å. The nearzone size for an edge at 8530 Å and the quasar redshift estimated above is $4.1^{+1.1}_{-1.2}$ proper Mpc, the error in this measurement is dominated by the error in the redshift. In Figure 3.12 the normalised flux and the extent of the nearzone are shown. The corrected nearzone size of this object is found to be consistent with the measured relationship in the Carilli et al. (2010) study.

Quasar near zones are used as a probe to study the neutral hydrogen level in the Universe at the redshift of the quasar. Measuring the near zone size of this quasar can be used to place inference on the environment around the quasar. While the

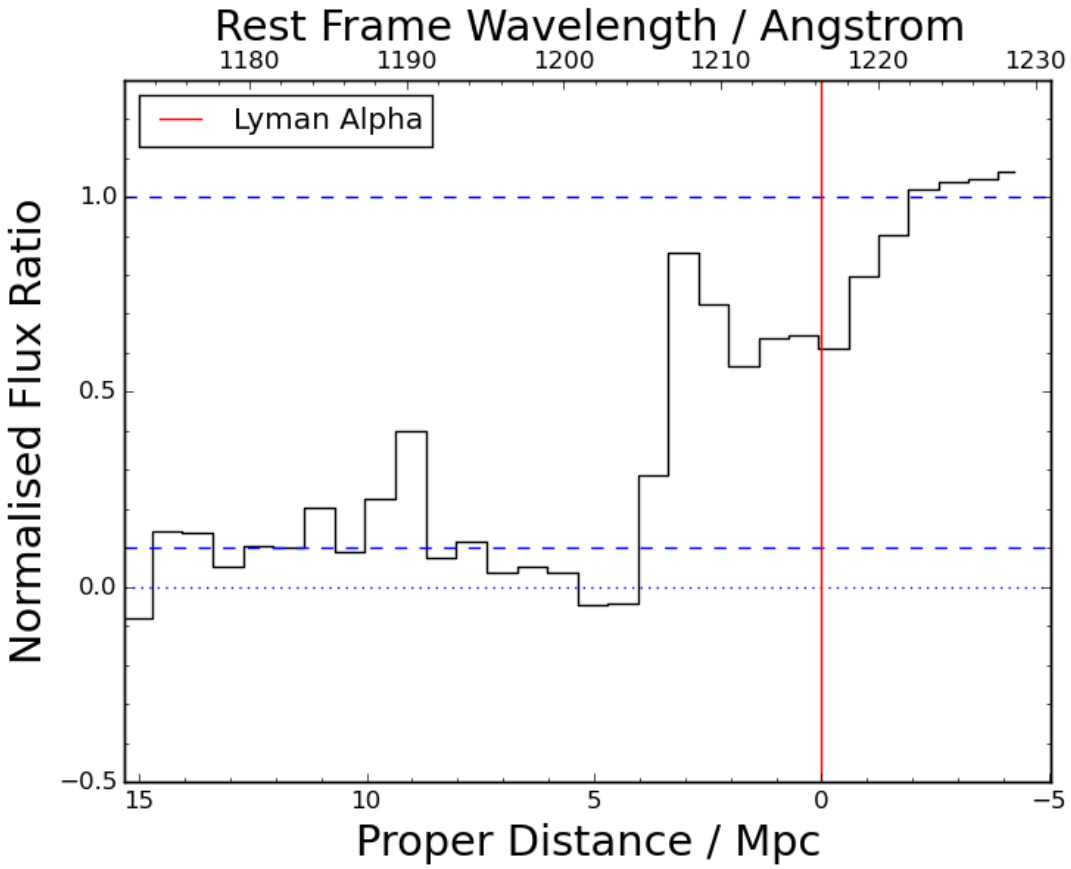

Figure 3.12 In this plot the ratio of the continuum flux and the spectrum is shown. The red vertical line shows the position of the Lyman alpha emission line. The dashed blue line is at a flux ratio of 0.1 and the dotted blue line show the zero level. The nearzone has a size of $4.1^{+1.1}_{-1.2}$ proper Mpc.

measurement of one near zone does not lead to strong constraints calculating it is a good proof of concept that the discovery spectrum can be used to measure the near zone size. This will be further investigated in Chapter 6.

3.3 Discussion

Estimates from the Willott et al. (2010) and McGreer et al. (2013) luminosity functions suggest that there are 5 to 10 quasars with 5.7 < z < 6.5 in the SVA1 area with z band magnitude brighter than 21.5. Our selection method gives 43 other candidate objects and suggests four as higher priority than the others. This final selection step is biased towards bright objects, due to them having smaller errors than fainter candidates, and is not designed to find a complete sample. To find all the quasars in this area with a high purity would require full Bayesian analysis of the quasar population and the

Table 3.3 Properties of DES J0454-4448. The g band magnitude is given as a 2σ magnitude limit for a 2" aperture. The $R_{NZ,corrected}$ size is calculated using the equation given in Section 4.4.

	DES J0454-4448
DES Tilename	DES0453-4457
RA (J2000)	73.50745 ($04^h54^m01.79^s$)
DEC (J2000)	-44.80864 (-44°48'31.1")
Redshift	6.09 ± 0.02
g	> 25.16
r	25.30 ± 0.25 [AB]
i	22.66 ± 0.05 [AB]
z	20.20 ± 0.01 [AB]
Y	20.24 ± 0.04 [AB]
J	20.24 ± 0.07 [AB]
Ks	20.12 ± 0.17 [AB]
W1	19.68 ± 0.08 [AB]
W2	19.62 ± 0.14 [AB]
M_{1450}	-26.48 ± 0.03
R_{NZ}	$4.1\ ^{+1.1}_{-1.2}$ Mpc
$R_{NZ,corrected}$	$4.8^{+1.3}_{-1.4}$ Mpc

brown dwarfs.

The discovery of the first quasar from DES is an important milestone towards finding bright high redshift objects suitable for follow up studies and towards the selection of a larger sample of z > 6 quasars.

The redshift determination method introduced here will be developed further in Section 4.3. A method of redshift determination that works accurately on the, generally low quality, optical discovery spectra that are the normal first step in identifying high redshift quasars was developed. The ability to get a reproducible redshift from optical data allows prioritisation of candidates before follow up spectroscopy is taken. It also means that optical spectra can be used to get accurate redshifts for any large samples of high redshift quasars that are to be used for statistical purposes.

3.4 Summary and Conclusions

Presented here are the results of the first search for high-redshift quasars in the Dark Energy Survey using 291 deg^2 of optical imaging data from the DES SV observations. The aim was to find one z > 6 quasar from this area as a proof of concept of the methodology presented here. This led to the discovery and spectroscopic con-

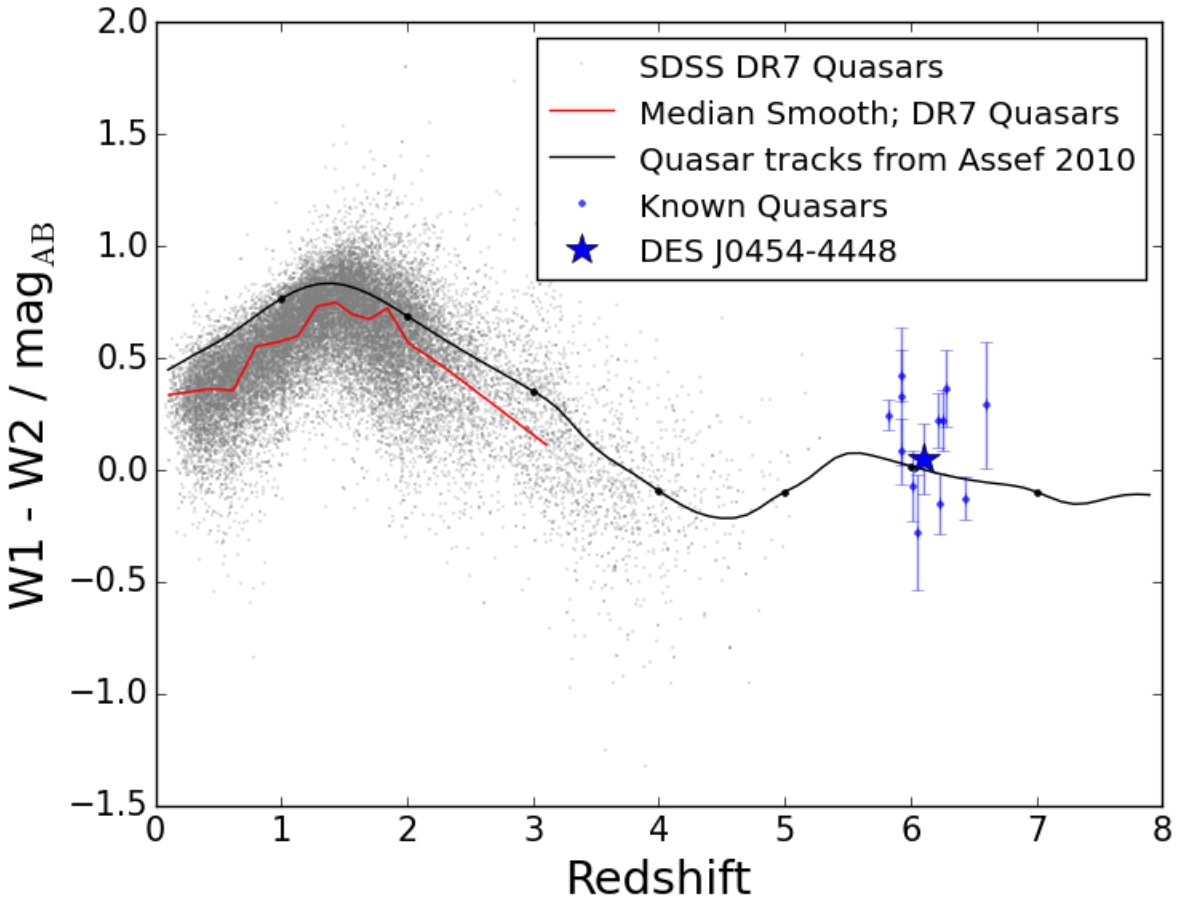

Figure 3.13 The Figure shows the evolution in W1 - W2 colour with redshift of known quasars. The grey points are known low-redshift quasars from SDSS DR7 with the red line being a median smooth of these data. This allows comparison with the predicted track, from Assef et al. (2010), which is shown by the black line. The blue points are a sub sample of the known high redshift quasars matched to WISE, these objects were matched to the ALLWISE data and then visually inspected to remove blended sources in WISE. The large blue star is DES J0545-4448.

firmation of DES J0454-4448 a quasar at z = 6.09±0.02 (based on the onset of the Lyα forest) with z_{AB}, Y_{AB} = 20.2, 20.2 (M_{1450} = –26.5). This quasar was the brightest of our candidates and was identified for spectroscopic follow up solely based on the DES i - z and z - Y colours. The algorithms summarised in this chapter have proved to be effective in removing image artefacts and spurious sources such as cosmic rays and satellite trails that can populate the same regions of colour space as rare objects in the data.

The method presented here builds on the simple colour cuts used in previous searches to develop a selection with a high success rate. Based on the DES photometric data alone, it was possible to reduce the number of candidates in this region to a size suitable for visual inspection. Unlike previous searches for high redshift quasars

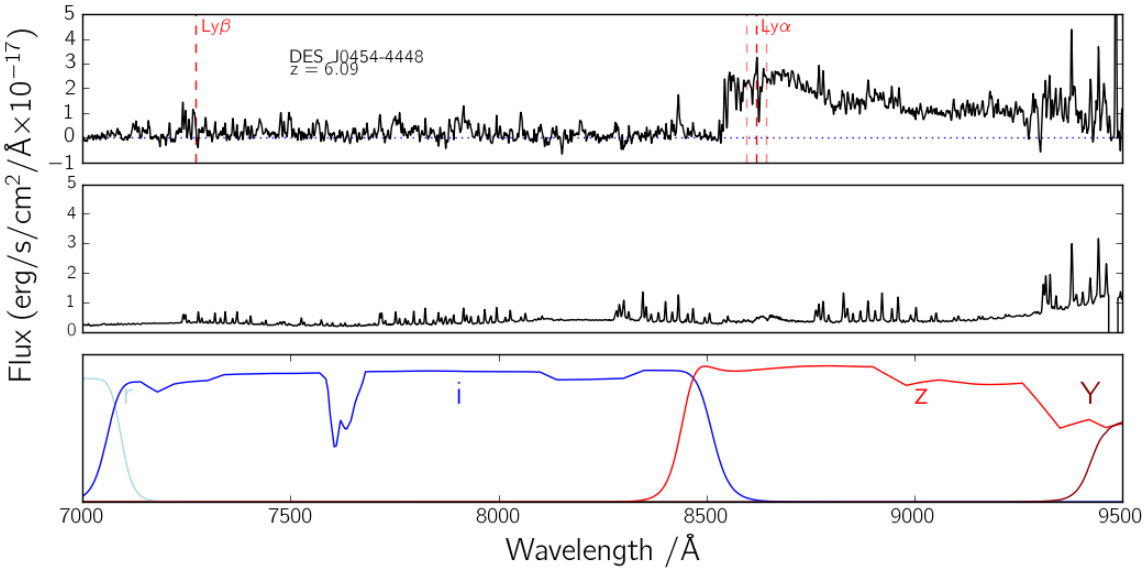

Figure 3.14 The discovery spectrum of DES J0454-4448 at z = 6.09. It shows the characteristic flux deficit blueward of Lyman alpha indicative of a high redshift quasar. The red vertical lines over the spectrum show the positions of the Ly-β and the Ly-α emission line redshifted to z = 6.09 as well as the errors on the position of Ly-α from the error in the redshift. The middle plot shows the error spectra and the bottom plot indicates the efficiencies of the DES filters as a function of wavelength. Both the object spectra and associated error spectra have been smoothed to the same degree using a Gaussian filter.

the selection presented in this Chapter does not require additional confirmation photometry. With the advent of large area surveys that will produce very large numbers of quasar candidates it will become more important to have clean candidate lists that do not require lots of telescope time as an intermediate step.

A photometric error-weighted colour selection metric was introduced as a method of ranking candidates according to the probability of being high-redshift quasars. The highest ranked candidate, DESJ0454–4448 was spectroscopically confirmed to be a high redshift quasar at z = 6.10. This method will be developed further in chapter 4 and extended to the full DES area covered by the Year 1 (Y1) and Year 3 (Y3) data releases.

4

High Redshift Quasar Selection via SED Model Fitting

Following on from the approach introduced in Chapter 3 a method was developed to fit the full multiwavelength photometric data to a range of quasar models and to a series of cool dwarf star templates. This method was refined on the Y1 data and then applied to the Year 3 (Y3) data when it was released. The Y3 data covered the full DES footprint of $\sim$5000 deg^2. This Chapter covers the development of this method and its application to DES Y1 and Y3 data to discover 13 new quasars. The Y1 and Y3 data releases for DES are discussed in Sections 2.2.3 and 2.2.4 respectively along with the overlapping VHS data used.

4.1 Quasar Candidate Selection

The basis for the spectral energy distribution (SED) fitting selection was the work done in Chapter 3 which derived basic colour cuts to narrow down the candidate list, developed data clean up techniques and used a preliminary prioritisation method to finalise the candidate list. The starting point for the selection was the first eight steps outlined in Section 3.1.2 and is summarised in Table 4.1. Then the candidate list was matched to the VHS catalogue data to give J and K band magnitudes for the objects which was a fast way to remove artefacts such as cosmic rays that were present in only one of the surveys. Matching to VHS and keeping only objects with Y_{AB} - J_{AB} < 1.0 left 960 candidates from the original 4,195 that satisfied the first stages of the selection. The cuts used are shown in Figure 4.1 and 4.2. The z - Y and Y - J cuts were chosen to be the reddest cuts that excluded all known dwarf stars used in this analysis. Dwarf stars were taken from Kirkpatrick et al. (2011).

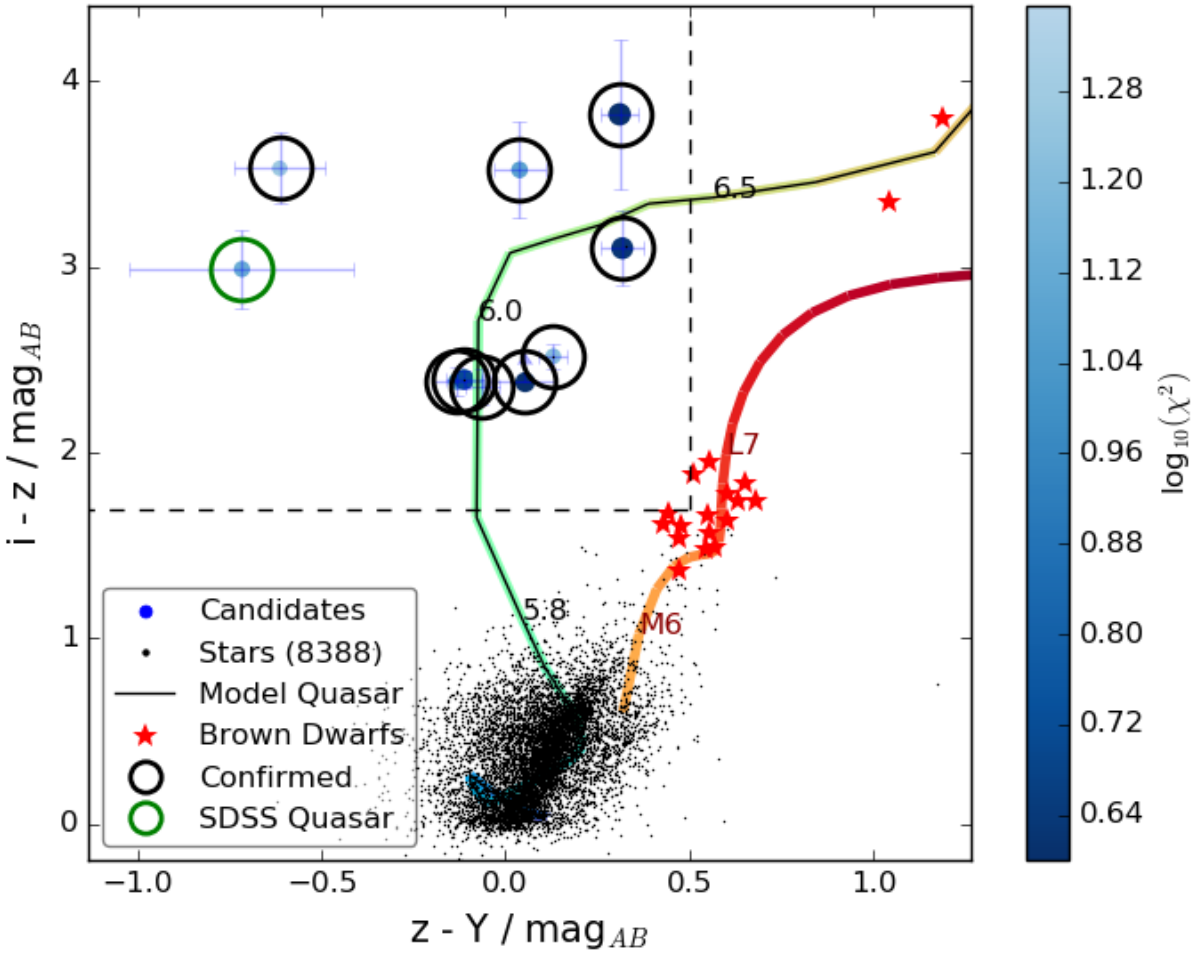

Figure 4.1 z - Y versus i - z colour - colour diagram shows the colour space used for the selection. The dashed lines show the z - Y and i - z colour cut limits used. This colour cut limit is the same as was used in Chapter 3 and was designed to help remove cool stars. The black points are stars taken from three tiles of DES Y1 data and the red stars are known brown dwarfs from Kirkpatrick et al. (2011) matched to the DES data. The red line shows the derived colour track for dwarf stars and the blue-green line shows one of the quasar tracks used. The blue points give our candidate objects with higher ranked objects being darker in colour and larger in size. The black circled objects were followed up spectroscopically, the green circle shows the known SDSS quasar. Objects with a good fit to the brown dwarf model are not shown on this plot. A large colour region around the predicted colour line is probed to account for the intrinsic variation in the SEDs of quasars as well as line of sight extinction in the sources and the uncertainties in the photometry for each object.

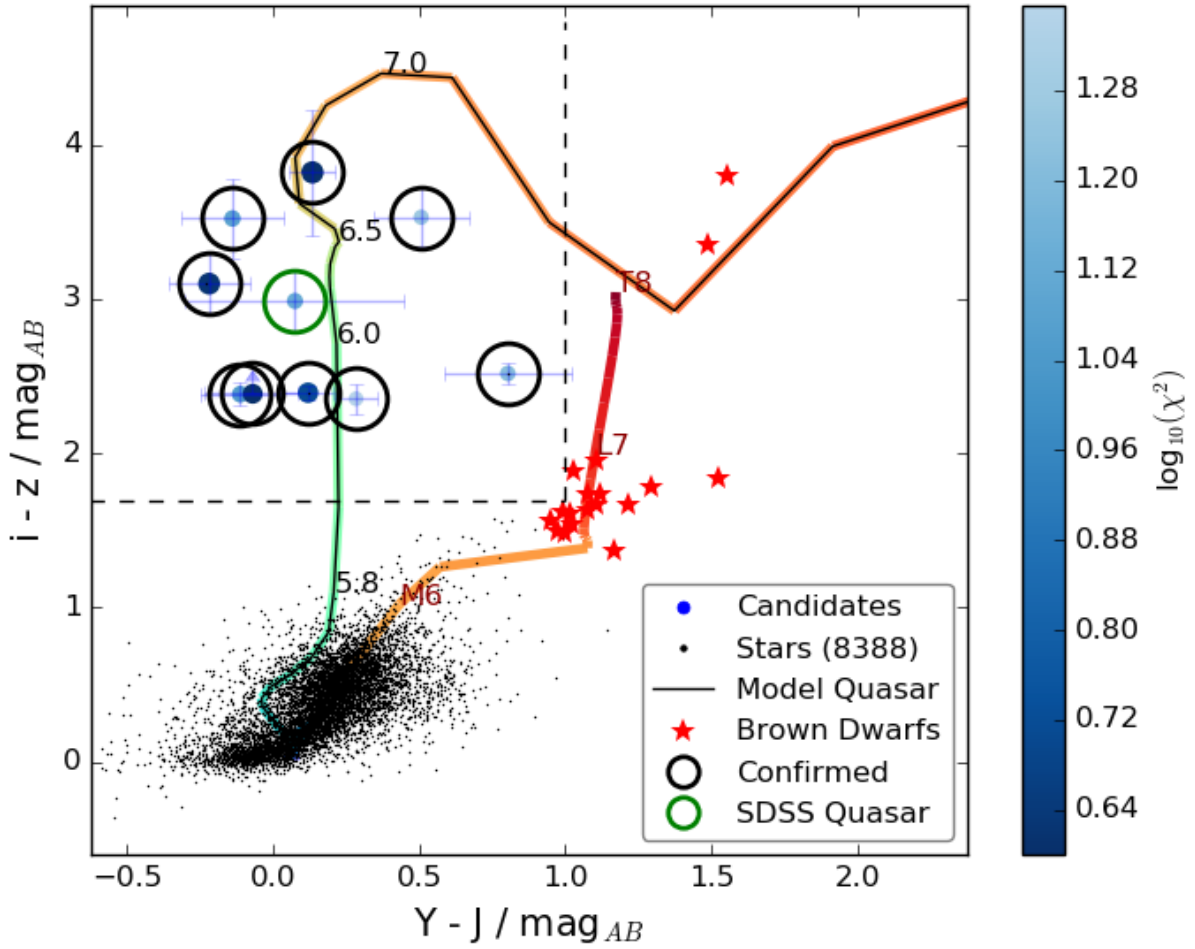

Figure 4.2 Y - J versus i - z colour - colour plot showing the reasoning behind the Y - J colour cut. A colour limit of 1.0 (marked with a dashed line) removes all known cool dwarf stars while allowing us to probe as much parameter space as possible. In future work we hope to loosen or remove this colour cut. The points in this Figure follow the same schema as in Figure 4.1. Objects with a good fit to the brown dwarf model are not shown on this plot.

4.1.1 *WISE* List Driven Aperture Photometry

As the W1 - W2 colour is a discriminant between quasars and cool stars, list driven aperture photometry code was run on the unWISE images (Lang, 2014). The unblurred coadds from the *WISE* Atlas images were used. The unWISE coadd images are 2048 $\times$ 2048 pixels at the nominal native pixel scale, 2.75 per arcsec pixel, rather than the rebinned 4095 $\times$ 4095 images at 1.375 per pixel chosen in the AllWISE Release. The AllWISE images are convolved by a model of the PSF to create images that are better suited for source detection but the unblurred unWISE coadds used here have better resolution, and are therefore more appropriate for forced, list-driven photometry at known positions on the sky (Lang, 2014). Forced photometry

Table 4.1 Summary of the steps in the high-redshift quasar selection process. The individual parts of step one are detailed fully in Section 4.1 and are not differentiated here.

Step	Description	Number Removed	Number Remaining
	Number of objects in database		139,142,161
1	Steps 1-8b from Chapter 3[†]		
	$z_{PSF} \leq 21.0$ and $\sigma_z < 0.1$		
	i_{PSF} - $z_{PSF} < 1.694$		
	g_{PSF} and $r_{PSF} > 23.0$		
	σ_g and $\sigma_r > 0.1$		
	z_{PSF} - $Y_{PSF} < 0.5$		
	$Y_{PSF} < 23.0$	139,135,538	4,195
2	Y - J < 1.0	3,235	960
3	Remove Chip Edges in z Band	498	462
4	Remove Bad Image Areas	105	393
5	Remove Objects Bright in r	246	147

[†] A magnitude limit of z = 21 was used rather than 21.5 in Section 4.1 and no point source separation.

was done using imcore_list from version 1.0.26 of the CASUTOOLS software package (Irwin, 1985) [1]. The code was run for all objects in the VHS catalogue where the VHS sources were used as inputs as they are closer in wavelength than the DES sources so were more likely to have a corresponding *WISE* source. The approach of using the J band positions will also allow these same catalogues to be used as the search is pushed to higher redshift where we expect quasar candidates to no longer be detected in the shorter (riz) wavelength DES bands at all. An aperture radius of 2.5 pixels ($\sim$ 6.9") was used for the list driven photometry on the WISE images. This was chosen to match the aperture size used for the published *WISE* catalogues. While a smaller aperture size would help to ensure that the flux came only from the specified object it would also miss more of the WISE flux that is outside the aperture due to the point spread function of *WISE*. A larger aperture can also include flux from neighbouring objects. An alternative approach would be to estimate the WISE fluxes using PSF based weighting. To do this the PSF of the images would need to be characterised (for example using PSFEx (Bertin, 2011)) and then used to ensure that all the flux from the object was accounted for.

The output catalogues were then compared with the published *WISE* catalogues to check the reduction. The forced photometry catalogues were found to give consistent magnitudes with the published catalogues when the same aperture size was used.

[1] http://casu.ast.cam.ac.uk/surveys-projects/software-release

4.1.2 Photometric SED Modelling, Redshifts and Stellar Classification

To prioritise the candidates a photometric redshift fit was carried out using a series of model spectral energy distributions (SEDs). Four quasar models (Maddox et al., 2012) based on the spectral templates in Maddox & Hewett (2006), with different levels of intrinsic reddening (E(B−V) = 0.0, 0.025, 0.05, 0.10 in the restframe quasar spectrum) were used in 0.1 redshift increments between 4.0 and 8.0 for the model fitting. The model is a parametric model where the continuum consists of two power laws (with slopes -0.42 and -0.17) that are joined at 2340Å. Longward of one micron the flux is dominated by a single temperature black body with T = 1236K. On top of this is an empirical quasar emission line spectrum. Shortward of the Lyα emission line the continuum flux is suppressed by a model of the Lyα forest absorption which is redshift dependent. All the flux shortward of the restframe Lyman-limit (912Å) is removed. Lyα, Lyβ and Lyγ flux is removed to match the empirical levels found in Fan et al. (2006b). Above z = 5.5 the optical depth is treated differently and is chosen to match the observed optical depths from Fan et al. (2006b) which rise more steeply with redshift at z > 5.5 than at lower redshift. Thus at all redshifts above z = 5; there should be zero flux in the DES g band which has <1% of peak transmission at λ > 5530Å (corresponding to 912Å at z $\sim$ 5). The flux from the model was integrated over all the DES and VHS wavebands as well as the *WISE* W1 and W2 bands. As the DES aperture fluxes do not include aperture corrections by default and SExtractor (Bertin & Arnouts, 1996) does not return negative fluxes for PSF fluxes, aperture corrections were calculated to account for any flux that fell outside the aperture. It was necessary to have good measurements of the flux for very faint/undetected objects as all of our candidates are not present in the bluest DES bands. The aperture corrections were calculated using the median of the $\frac{\text{PSF flux}}{\text{Aperture flux}}$ for stellar objects. They were calculated for each individual DES image tile and applied separately for each tile. The objects were also compared to the derived brown dwarf colours from Skrzypek et al. (2015). As these colours were given in the UKIRT Infrared Deep Sky Survey (UKIDSS) Large Area Survey (LAS) and SDSS pass bands, colour terms (given in Appendix A.2) were calculated between the surveys using the overlap between DES, UKIDSS, VHS and SDSS in Stripe 82. The colours were then converted onto the AB system using the offsets given in Hewett et al. (2006). The reduced χ^2 (χ^2_{reduced}) values were derived using the formula below:

$$\chi^2_{i,\mathrm{reduced}} = \sum_{n=1}^{N} \left(\frac{\mathrm{data}_n - \mathrm{f}_n(\mathrm{model}_i)}{\sigma(\mathrm{data})_n} \right)^2 \Big/ (N-1) \tag{4.1}$$

where for each model_i we sum over n = 1...N wavebands with N-1 degrees of freedom.

When the photometric fitting method was first run it was found that objects with unreliable non-Gaussian errors in their photometry, due for example to CCD chip edges and saturated objects, were contaminating the candidate list. These objects were then removed using image based techniques. To remove objects with photometry affected by chip edges the pixel values in a 30" box around the object were analyzed and if more than a third had the same value the object was rejected; this also removes areas which have been masked with zeros in the image (such as saturated areas and bleed trails). It was found that a large number of the candidates appeared to have no measured flux in the g, r, or i bands but there were also no other objects present with a region with radius of 30 arcseconds around the location of the candidate in the image. It was found that these patches of image had very different noise properties compared to other parts of the image. To remove these the median and the median absolute deviation (MAD) of the pixel values in a 30 arcsec box around the object were calculated. The MAD was used as it gives a robust estimate of the statistical dispersion of the data and is related to the standard deviation (σ) through σ = 1.4826MAD The pixel MAD was studied for a large number of images and the distribution of MAD values from 30 arcsec boxes across these images was found to be bimodal with a dip at $\sim$ 0.7 shown in Figure 4.3. Objects with a MAD value less than this empirically derived threshold of 0.7 were removed. The bright r band objects were removed as detailed in Section 3.1.3. These pixel level filtering steps are done after catalogue level selection as the image based techniques are more computationally intensive than the catalogue ones so it is more efficient to run them on the reduced candidate list rather than to create a completely clean list from the beginning. Furthermore, if the images are not available colocated to computational resources, network transfers can be prohibitive. Table 4.1 lists the numbers of candidates removed by each selection stage.

The photometric fitting was then run again on the 147 remaining candidates. Candidates were first ranked based only on their quasar reduced χ^2 values with the smallest reduced χ^2 sources having the highest ranking. Following this ranking, the candidates were visually inspected in ranked order to remove artefacts and junk sources, and also compared the quasar reduced χ^2 values to those obtained from a brown dwarf fit to the photometry. The likelihood of being a brown dwarf was calculated from the polynomial fits in Skrzypek et al. (2015). Objects where the reduced χ^2 to be a

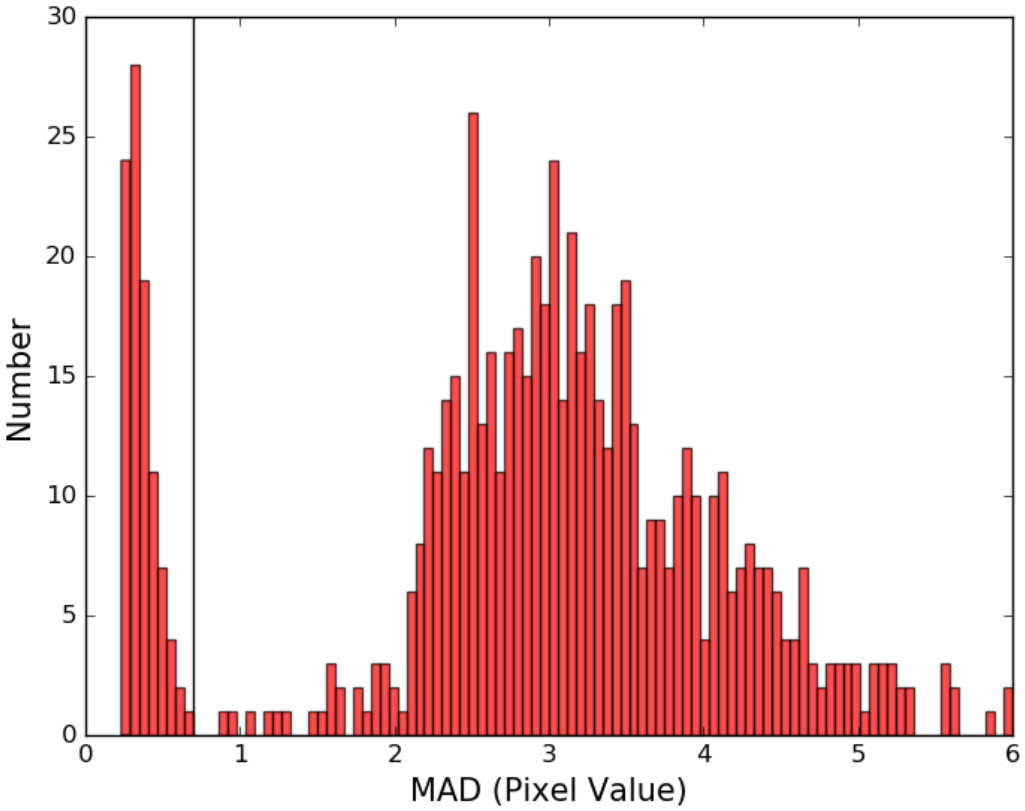

Figure 4.3 The distribution of MAD values from 30 arcsec boxes across the images containing quasar candidates. It can be seen that the distribution is bimodal.

brown dwarf was comparable to or higher than that to be a quasar were removed.

It was found that the reduced χ^2 values for the best fitting quasar and low mass star models often exceeded 3 and hence were ruled out at > 99%. At face value this is indicative that neither model fitted the data. This could be interpreted to mean that the photometric measurements had systematic errors or the range of SED models being considered was not representative of the underlying true distribution. A pragmatic approach was taken and a systematic photometric uncertainty was added to the statistical uncertainty in each waveband. Percentage errors in flux of 10%, 10%, 10%, 20%, 5%, 5%, 5%, 5%, 20% and 20% in g, r, i, z, Y, J, H, Ks, W1 and W2 respectively were added in quadrature to the statistical uncertainties as show in Equation 4.2. This errors reflect both the data quality and the observed spread in quasar fluxes in each band. The large error used in the z band, despite the good data quality in this band, was included to cover the wide range of properties observed in the Lyα emission line which are not fully covered by the models used.

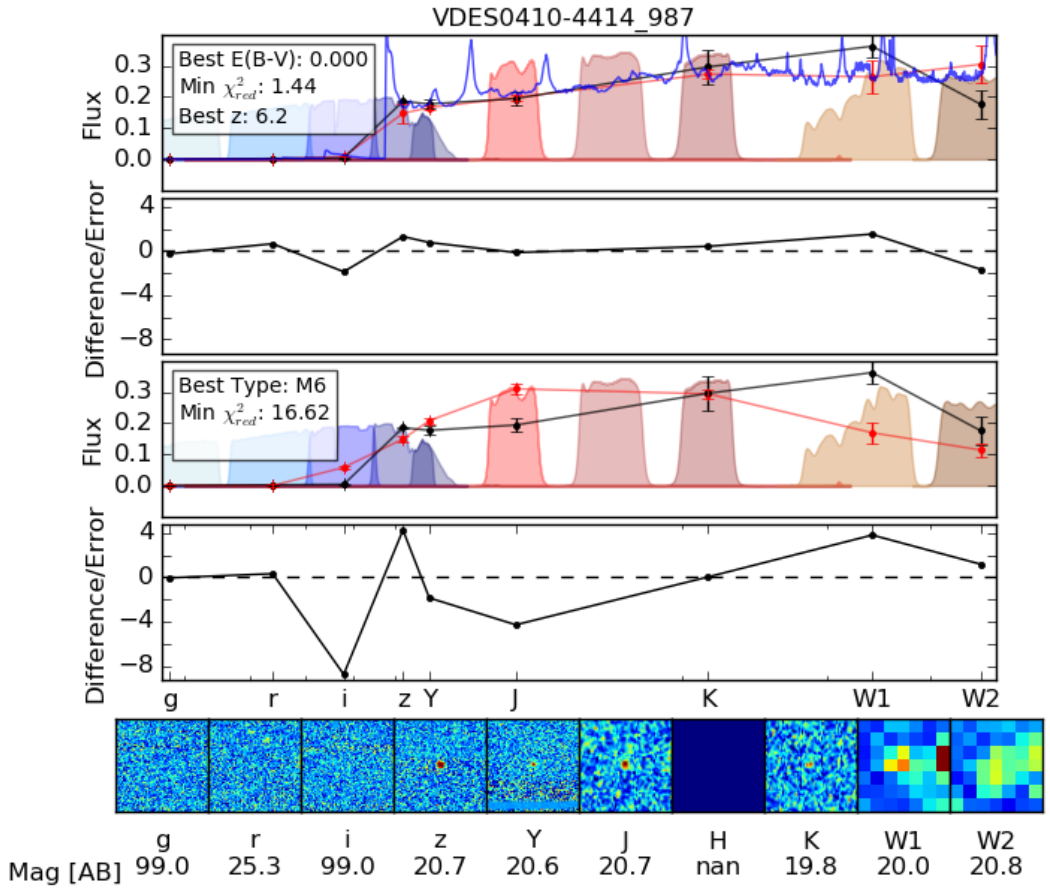

Figure 4.4 An example of the model fitting results for the highest ranked quasar in the sample. The top panel shows the best fitting quasar model in red and the data with associated uncertainties in black. The filled areas show the filters for DES, VHS and *WISE*. The blue line shows the model quasar spectra used. The second panel down shows the residuals from the fit divided by the uncertainties on each point. The third and fourth panels show the same thing for the best fitting cool star model. Along the bottom of the Figure are 20 arcsec cutouts in each band with the AB magnitude in that band beneath.

$$\chi^2_{i,\text{reduced}} = \sum_{n=1}^{N} \left(\frac{\text{data}_n - f_n(\text{model}_i)}{\sigma(\text{data} + \text{model})_n} \right)^2 \Big/ (N-1) \tag{4.2}$$

The resultant χ^2 values for the 10 highest ranked quasar candidates are shown in Table 4.2. The 10 objects with highest low mass star SED probability are listed in Table 4.3 and have a range of best fit spectral types from M5 to L3. Figures 4.4 and 4.5 show the results of the model fitting for the highest ranked quasar candidate and a probable low mass star with spectral type M7.

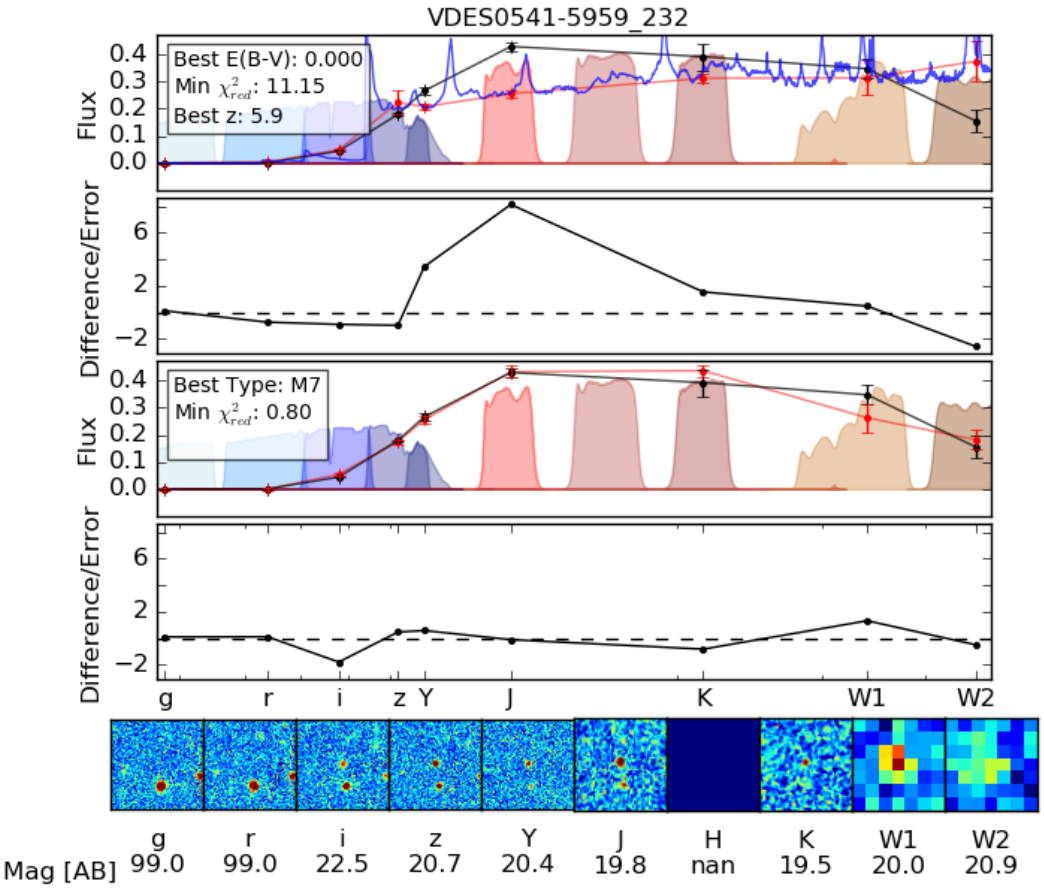

Figure 4.5 An example of the fitting results for the highest ranked low mass cool star in the sample. The colours and lines are the same as in Figure 4.4.

Table 4.2 Parameters from the fitting process for the confirmed quasars.

Name	Rank	χ^2_{red} of Best Quasar Model	Best E(B-V)	Best Redshift	Spectroscopic Redshift	χ^2_{red} of Best Brown Dwarf Model	Best Type	$\frac{\chi^2_Q}{\chi^2_{BD}}$
VDES J0143-5545	9	3.15	0.100	6.1	6.25	38.87	M7	0.081
VDES J0224-4711	3	1.62	0.050	6.4	6.50	32.24	M7	0.050
VDES J0323-4701	10	3.35	0.000	6.1	6.25	15.02	M5	0.223
VDES J0330-4025	5	2.24	0.025	6.2	6.25	18.71	M7	0.120
VDES J0408-5632	8	3.10	0.000	6.0	6.03	13.76	M6	0.225
VDES J0410-4414	1	1.44	0.000	6.2	6.21	16.62	M6	0.087
VDES J0420-4453	6	2.54	0.000	6.0	6.07	19.44	M6	0.131
VDES J0454-4448†	2	1.55	0.000	6.0	6.10	18.81	M6	0.082
VDES J2250-5015	4	1.78	0.050	6.0	6.00	12.20	M8	0.146
VDES J2315-0023⋆	7	2.67	0.000	6.0	6.12	30.92	M5	0.086

† This object was found in Chapter 3.

⋆ This object is SDSS J231546.57+002358.1 found in Jiang et al. (2008).

Table 4.3 Parameters from the fitting process for the ten objects ranked highest to be low mass cool stars or brown dwarfs. Only objects with photometry in all the available bands were included here.

Name	χ^2_{red} of Best Quasar Model	Best E(B-V)	Best Redshift	χ^2_{red} of Best Brown Dwarf Model	Best Type	$\frac{\chi^2_Q}{\chi^2_{BD}}$
VDES J0419-5033	18.55	0.000	6.0	1.05	L0	17.67
VDES J0440-5258	11.48	0.000	6.0	1.43	L0	8.03
VDES J0516-5433	9.25	0.050	6.0	1.38	L3	4.53
VDES J0524-5710	19.37	0.000	5.9	0.82	M7	23.62
VDES J0541-5959	11.15	0.000	5.9	0.80	M7	13.94
VDES J2138-5853	18.69	0.000	5.9	1.36	M7	13.75
VDES J2248-4639	12.36	0.025	6.0	1.31	L1	9.44
VDES J2300-4432	13.88	0.000	6.0	1.06	M9	13.10
VDES J2307-0044	24.54	0.000	6.0	1.07	L0	22.93
VDES J2321-5655	6.66	0.000	5.2	1.10	M5	6.05

4.2 Spectroscopic Observations

Spectroscopic observations of the eight unconfirmed candidates from Section 4.1.2 were obtained between 2015 October and November using the European Southern Observatory's (ESO) 3.58m New Technology Telescope (NTT) and the 8.1m Gemini-South Telescope. The other two objects from the selection are already confirmed quasars, one found in Chapter 3 and one in Jiang et al. (2008). The confirmed quasars from these spectroscopic follow up runs are listed in Table 4.2. A summary of the observations, including the exposure times and grism/grating used, is given in Table 4.4 and a summary of the objects' properties are given in Tables 4.5 and 4.6. Four of the objects were observed with the NTT at ESO's La Silla observatory over three nights from the 2015 October 7th to the 9th. The spectra were taken with the ESO Faint Object Spectrograph and Camera 2 (EFOSC2) (Buzzoni et al., 1984) and reduced using a custom set of python routines detailed below. Calibration data were taken either during the afternoon preceding the observations or taken as part of the PESSTO project (Smartt et al., 2015). A 1.5" width slit was used and the data was binned 2x2 on data readout. Due to the inclemency of the weather (cloud coverage) and the smaller mirror aperture the NTT data are of modest quality compared to the Gemini observations of the rest of the sample. Four of the objects were observed with the Gemini Multi-Object Spectrograph (GMOS) (Hook et al., 2004) at the Gemini South Telescope as part of the 2015B queue observations using a 0.75" mask and reduced with a custom python reduction code.

Table 4.4 Details of the spectroscopic observations

Name	Telescope	Instrument	Exposure Time (Seconds)	Date	Filter	Grating/ Grism
VDES J0143-5545	NTT	EFOSC2	1200 + 1200 = 2400	09/11/2015	OG530	Gr#16
VDES J0224-4711	NTT	EFOSC2	1800 + 1800 = 3600	07/11/2015	OG530	Gr#16
VDES J0323-4701	GEMINI-S	GMOS-S	600 + 600 + 600 + 600 = 2400	22/11/2015	RG610_G0331	R400+_G5325
VDES J0330-4025	GEMINI-S	GMOS-S	600 + 600 + 600 + 600 = 2400	22/11/2015	RG610_G0331	R400+_G5325
VDES J0408-5632	NTT	EFOSC2	1200 + 1200 = 2400	08/11/2015	OG530	Gr#16
VDES J0410-4414	GEMINI-S	GMOS-S	600 + 600 + 600 + 600 = 2400	11/09/2015	RG610_G0331	R400+_G5325
VDES J0420-4453	GEMINI-S	GMOS-S	600 + 600 + 600 + 600 = 2400	04/09/2015	RG610_G0331	R400+_G5325
VDES J2250-5015	NTT	EFOSC2	1800 + 1800 = 3600	07/11/2015	OG530	Gr#16

Table 4.5 Properties of the quasars in this sample. Upper limits are given for the magnitude in a 2 arcsec diameter aperture. All magnitudes are given in AB.

Name	Ranking	DES Tilename	RA (J2000)	DEC (J2000)
VDES J0143-5545	9	DES0145-5540	25.79265	-55.75297
			$01^h43^m10.24^s$	-55°45'10.68"
VDES J0224-4711	3	DES0222-4706	36.11057	-47.19149
			$02^h24^m26.54^s$	-47°11'29.4"
VDES J0323-4701	10	DES0325-4706	50.91808	-47.02226
			$03^h23^m40.34^s$	-47°01'20.13"
VDES J0330-4025	5	DES0329-4040	52.61632	-40.42121
			$03^h30^m27.92^s$	-40°25'16.4"
VDES J0408-5632	8	DES0407-5622	62.08012	-56.54134
			$04^h08^m19.23^s$	-56°32'28.82"
VDES J0410-4414	1	DES0409-4414	62.51345	-44.24464
			$04^h10^m03.23^s$	-44°14'40.7"
VDES J0420-4453	6	DES0421-4457	65.04727	-44.88993
			$04^h20^m11.34^s$	-44°53'23.8"
VDES J0454-4448†	2	DES0453-4457	73.50744	-44.80864
			$04^h54^m01.79^s$	-44°48'31.1"
VDES J2250-5015	4	DES2250-4957	342.50837	-50.26171
			$22^h50^m02.01^s$	-50°15'42.15"
VDES J2315-0023⋆	7	DES2316-0041	348.94409	-0.39938
			$23^h15^m46.58^s$	00°23'57.78"

† This quasar was found in Chapter 3.2 and it is included here for completeness and to allow comparison between the different DES data releases and the different *WISE* reductions used.

⋆ This is a known object (SDSS J231546.57-002358.1) discovered in Jiang et al. (2008)

Table 4.6 Properties of the quasars in this sample. Two σ upper limits are given for the magnitude in a 2 arcsec diameter aperture. All magnitudes are given in AB.

Name	g	r	i	z	Y	J	Ks	W1	W2
VDES J0143-5545	> 25.97	> 25.58	24.03 ± 0.19	20.50 ± 0.02	21.11 ± 0.12	20.61 ± 0.11	20.09 ± 0.18	19.39 ± 0.09	19.00 ± 0.10
VDES J0224-4711	> 24.97	> 25.01	24.02 ± 0.40	20.20 ± 0.02	19.89 ± 0.05	19.75 ± 0.06	18.99 ± 0.06	18.75 ± 0.05	18.64 ± 0.14
VDES J0323-4701	> 26.15	> 25.85	24.30 ± 0.26	20.78 ± 0.02	20.74 ± 0.07	20.88 ± 0.16	20.51 ± 0.26	20.31 ± 0.17	20.51 ± 0.30
VDES J0330-4025	24.98 ± 0.37	> 25.55	23.76 ± 0.20	20.66 ± 0.02	20.34 ± 0.06	20.56 ± 0.13	19.99 ± 0.18	19.55 ± 0.09	19.58 ± 0.14
VDES J0408-5632	> 25.79	24.89 ± 0.42	22.48 ± 0.10	20.13 ± 0.01	20.19 ± 0.05	19.91 ± 0.06	19.70 ± 0.14	20.30 ± 0.15	19.74 ± 0.13
VDES J0410-4414	> 25.76	25.31 ± 0.45	> 24.79	20.65 ± 0.02	20.61 ± 0.09	20.68 ± 0.13	20.22 ± 0.22	20.00 ± 0.12	20.79 ± 0.34
VDES J0420-4453	> 26.02	24.98 ± 0.27	22.71 ± 0.07	20.32 ± 0.02	20.46 ± 0.06	20.57 ± 0.12	20.04 ± 0.19	19.73 ± 0.10	20.12 ± 0.21
VDES J0454-4448†	> 26.21	> 25.84	22.64 ± 0.05	20.24 ± 0.01	20.36 ± 0.05	20.24 ± 0.07	20.11 ± 0.18	19.62 ± 0.10	19.70 ± 0.15
VDES J2250-5015	> 25.35	> 25.43	22.63 ± 0.06	20.11 ± 0.01	19.98 ± 0.04	19.18 ± 0.21	19.00 ± 0.14	18.71 ± 0.06	19.04 ± 0.12
VDES J2315-0023⋆	24.00 ± 1.86	> 25.37	23.81 ± 0.20	20.83 ± 0.03	21.54 ± 0.30	21.47 ± 0.22	-	20.65 ± 0.31	-

† This quasar was found in Chapter 3.2 and it is included here for completeness and to allow comparison between the different DES data releases and the different *WISE* reductions used.

⋆ This is a known object (SDSS J231546.57-002358.1) discovered in Jiang et al. (2008)

4.2.1 NTT EFOSC2 Two Dimensional Data Reduction

Wavelength Calibration

Helium Argon arcs were taken each night and these were used to calibrate the wavelength scale. A gaussian profile was fitted to each line detected at $2 \times \sigma_{MAD}$ above a median filter of the surrounding 101 pixels. The wavelength of these lines was then identified by comparing them to the line lists given for each grism on the ESO website[2]. To calculate the wavelength solution a 3^{th} order Chebyshev polynomial series was fitted to the relationship, this fit and a comparison to a linear fit are shown in Figure 4.6.

As the NTT is prone to position dependent flexure the calibration was then fine tuned using a comparison between the sky lines and a calibrated sky spectrum. This was done by correlating three different sections of the sky spectrum calculated from the science spectra with the corresponding chunks of the calibrated sky spectra. The median of the offsets calculated from this was then applied to the wavelength calibration.

Flat Fielding

Flat field images were taken in the afternoon before the observations began. These had the large scale structure removed from them by dividing through by a median in the spatial direction. All the flats were then median combined to give a master flat. The 2D spectrum was then divided by the master flat.

Dark Subtraction

Dark images were also taken in the afternoon preceding the observations. These dark images were median combined to give a master dark which was then subtracted from the 2D science spectrum.

Cosmic Ray Removal

The cosmic rays were removed from the two dimensional spectra using cosmics.py (van Dokkum, 2001). This uses Laplacian edge detection to find the sharp edges of cosmic rays and is thus largely independent of morphology. Each cosmic ray pixel

[2]https://www.eso.org/sci/facilities/lasilla/instruments/efosc/inst/Perf_HeAr.html#HeArIdentifications

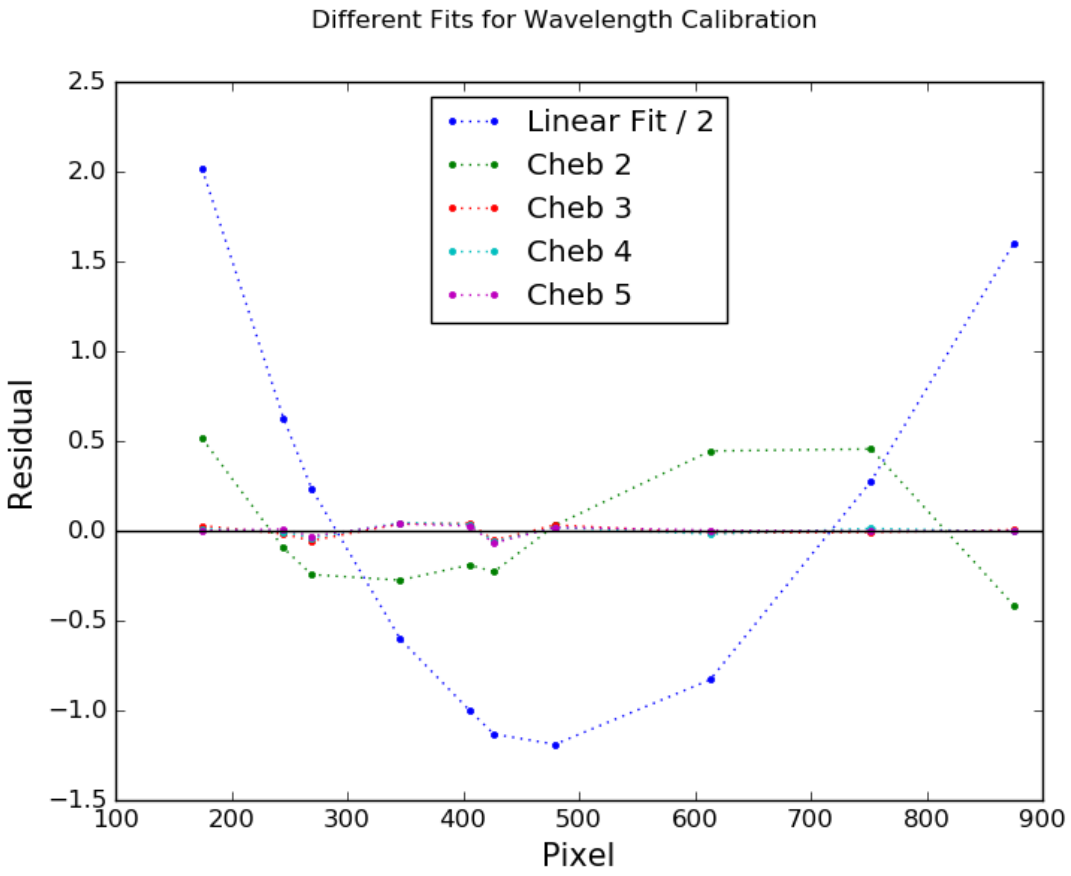

Figure 4.6 This figure shows the residuals from different fits to the wavelength calibration. It can be seen that the linear fit does not reproduce the data well. It was decided that a 3rd order Chebyshev gave a good fit to the data as this was the lowest order where the residuals did not exhibit wavelength dependent structure. Note that the residuals from the linear fit have been divided by two to allow for better visualisation.

found is replaced by the median of the surrounding pixels. The process can then be applied iteratively to remove cosmic rays that cover large numbers of pixels. To prevent the removal of undersampled emission lines in the spectra the Laplacian image is divided by a fine structure image. This is made of a combination of median filters at different scales. Small cosmic rays do not appear in this as the bright pixels are surrounded by noise. This means that the divided image (laplacian/fine structure) looks very different for cosmic rays and emission lines.

The two dimensional data can be seen pre and post cleaning in Figure 4.7. VDES J0224-4711, at z = 6.5 is used as the example in this Figure and the limited wavelength range with detectable emission can be clearly seen.

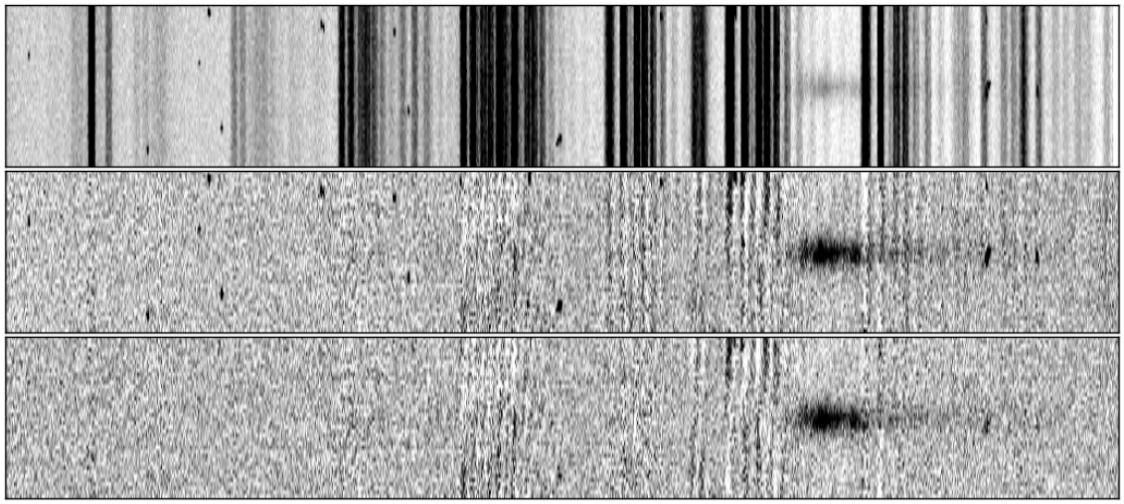

Figure 4.7 A 1030 by 40 pixel slice of the EFOSC data centred on the z = 6.5 quasar. The top panel shows the raw data, the middle panel is after sky subtraction but before any of the steps in Section 4.2.1 and the bottom panel is the data after the cleaning steps. In the bottom panel some sky residuals can still be seen but the prominent cosmic ray hits have been removed.

Object Identification

An automated method for finding the object in the 2-dimensional spectrum was developed. The spectrum was trimmed in the wavelength direction to give only the area we expected to see flux from the object in. This was done by passing the code an estimated value of the redshift of the object and then using the section of the 2d spectrum that was redward of the expected position of Lyα. This trimmed spectra was then summed in the wavelength direction, shown in Figure 4.8, to give increased signal to noise for the object. If this was done over the full wavelength range of the spectra then the additional noise from the wavelengths in which the object was not present could wash out the signal. (High redshift quasars have no flux blueward of the Lyα emission line which means that at z $\sim$ 6 they are not present in much of an optical spectra.) The sections of this wavelength collapsed image of the possible objects that had a 3σ detection were then taken as positions to be extracted.

Object Extraction

The centroid of the object's spectrum can vary across the wavelength range of the spectrum. As the high signal to noise parts of the quasar spectrum did not cover the full wavelength range of the observation they could not be traced across the CCD.

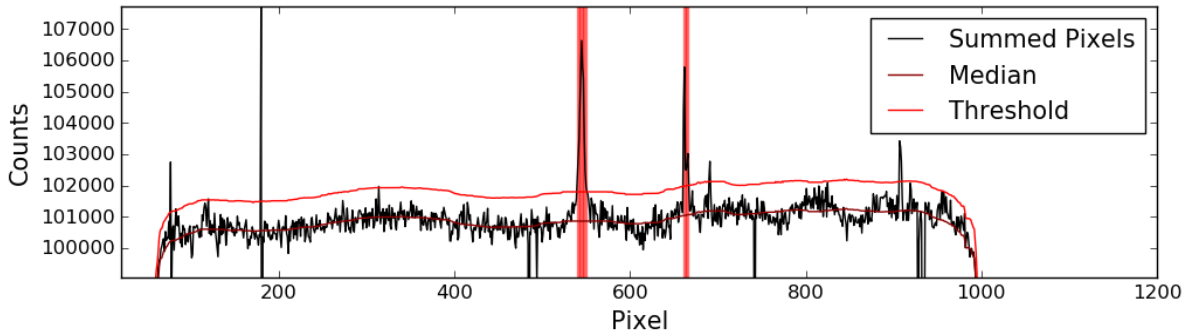

Figure 4.8 The summed pixels used for object detection. A clear detection of the object can be seen as well as a lower signal to noise erroneous detection. A conservative threshold that allowed some spurious detections through was required to detect some of the poor signal to noise, faint sources. The object detection was done before the data was flat fielded or dark subtracted but cosmic rays were removed. The red vertical bars show the locations of the potential objects that passed the threshold to have their 1D spectra extracted.

To alleviate this bright objects were traced across the CCD. This was done for five observations of standard stars observed within a few days of our observations. The traces of these objects were then fitted with a broken power law and compared.

As is shown in Figure 4.9 this equation reproduces the data well. The reasons for the turnover in the trace were then studied further. The 2D spectrum of the standard star L745A was compared to a reduce spectrum downloaded from the AAT. The 2D EFOSC spectrum and the calibrated AAT spectrum are shown in Figure 4.10. From this it can be seen that the spectrum appears to get brighter at the red end while the calibrated spectrum shows that the object flux decreases into the red wavelengths. The response of the grism also decreases with increasing wavelength so it is unlikely that this effect is due to the response of the system. As second order light can be a problem a blocking filter was used during the observations. The brightening of the spectrum at the red end could be due to the blocking filter not fully blocking out the second/higher order light. As this affected a very small area of the data, was in a low signal to noise area of the data due to the decreased response of the system to red light and was away from the main features (Lyα and NV lines) of the data it was decided to discard the data longward of the turnover point.

The turnover point of the trace was found and then the data blueward of this were fitted with a ninth order Chebyshev polynomial fit. This was done for five different observations taken within a few days of our observations to see how the trace of the object varied. These are shown in Figure 4.11. It can be seen from this that the trace varies by about half a pixel between different objects and different nights. This suggests that for the level of accuracy required a single object can be used to generate

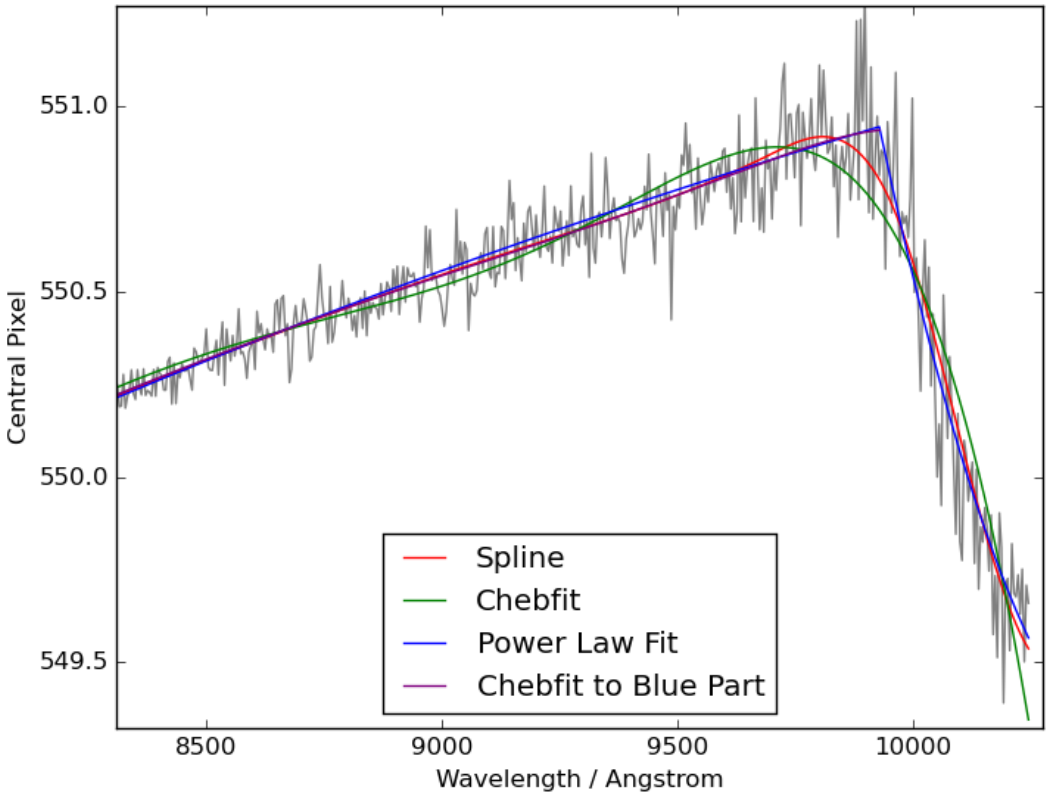

Figure 4.9 A variety of fits to the object trace zoomed in around the turnover point. From this it can be seen that a broken power law reproduces the turnover point the best. While a spline through the data works fairly well for this object it was not found to be reliable across all the objects tested.

the expected trace for these observations.

The section of the object spectrum where the centroid could be calculated at more than three σ_{MAD} consistently was compared to the predicted trace to calculate an offset. This offset was then applied to the trace to give the predicted central pixel at each wavelength bin. For the range of data where the centroid was consistently detected at > 3σ the centroid calculated from the data was used. For the rest of the spectrum the centroid predicted from the trace of the standard object was used. At the position predicted from the trace a Gaussian profile was used to weight the extraction of the spectrum.

To correct for the wavelength dependent response of the detector and instrument a standard star was used. A standard star observation (L745A) was reduced using the above method. This was then compared to a reduced and calibrated version from the Anglo Australian Telescope (AAT). This gave a baseline for what the spectrum should look like upon reduction. The initial data reduction does not account for wavelength

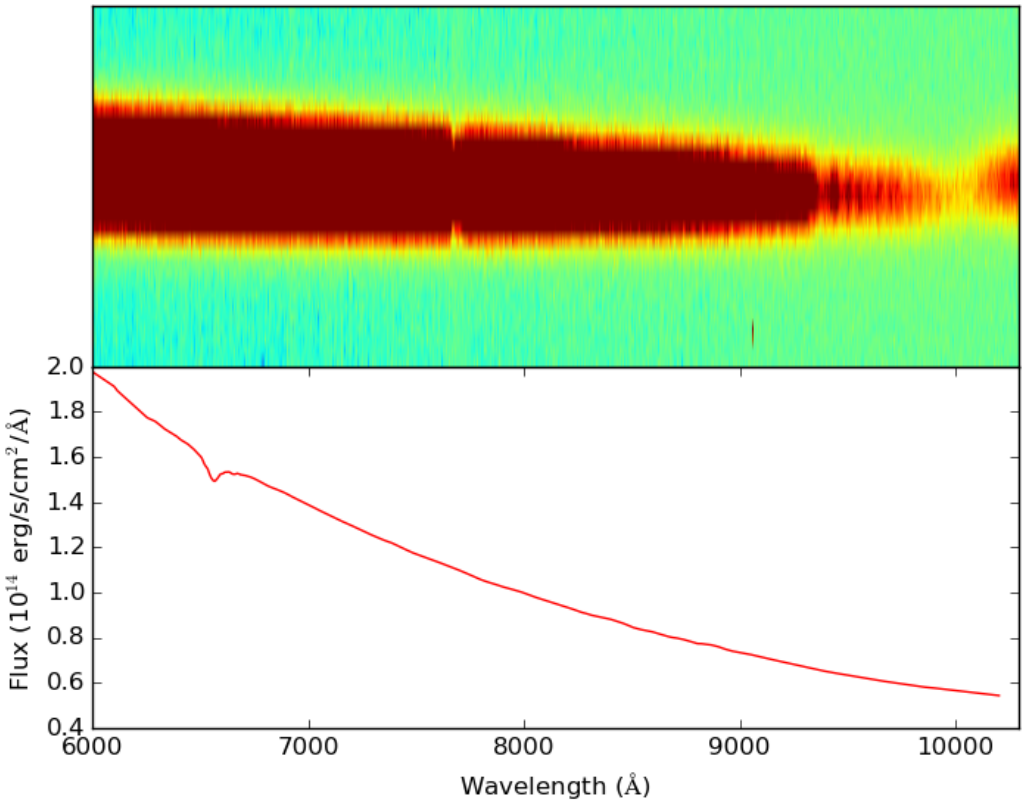

Figure 4.10 The top panel shows the 2D spectrum with the sky lines removed, the bottom panel show the fully reduced calibration data downloaded from the AAT. It can be seen that the 2D data abruptly gets brighter while the calibrated data keeps getting fainter. The change in position of the centroid coincides with the increase in flux.

dependence of the detector or for sky absorption features. To account for this the response function was calculated from comparing the calibrated and corrected standard star spectrum to the reduction done here of the same star. The response function was then used to correct the observations for the system response.

4.2.2 Gemini Data

The data taken with the Gemini telescope (GMOS-S) was reduced in a similar way to the EFOSC data. Four exposures were taken of each object two at each of two different central wavelengths. The spectra from the same central wavelength were reduced and then summed. The offset in central wavelength means that the patches of the spectra that fall in the gaps in the detector are at different wavelengths. To give full wavelength coverage the summed spectra were mean combined everywhere

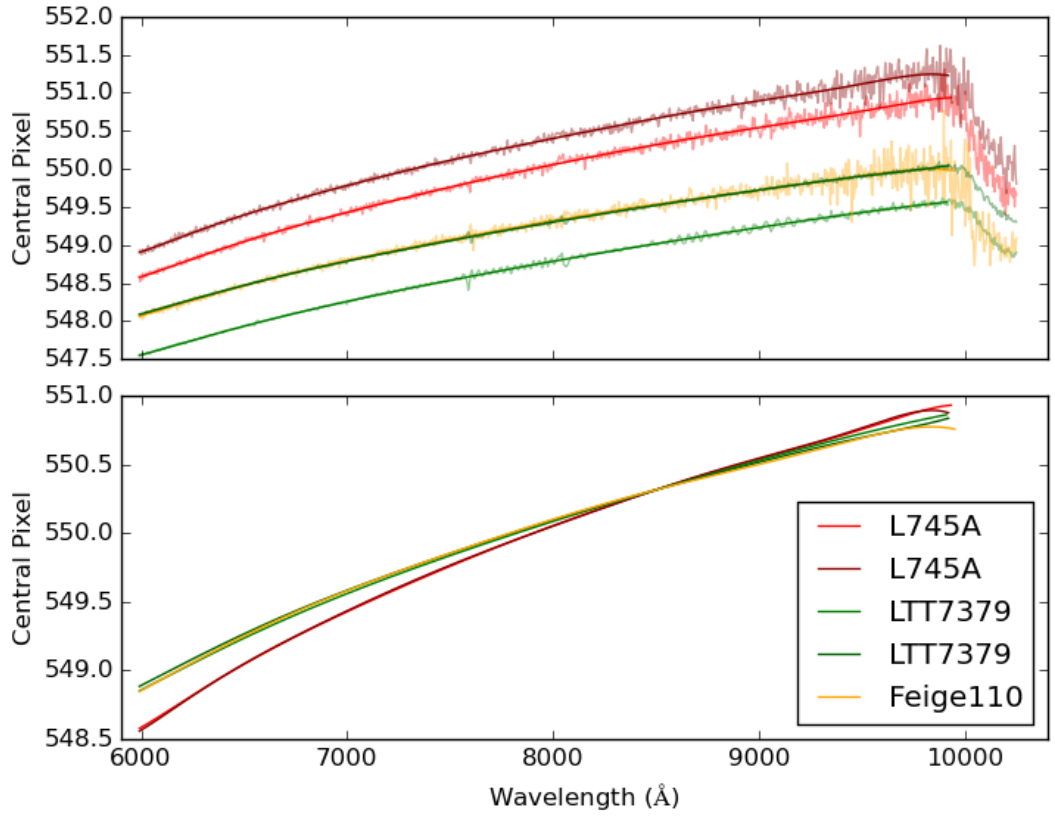

Figure 4.11 The top panel shows the five standard observations used. For each the turning point was calculated and then a ninth order Chebyshev polynomial was fitted to the data blueward of this turning point. The bottom panel shows these different fits with an offset applied so that they are equal at 8500. This gives a difference of under half a pixel at the blue and red ends of the data.

except in the gaps where the one with coverage was used.

The final reduction of all the candidates is shown in Figure 4.12 along with the object discovered in Chapter 3 as it was rediscovered in this sample.

4.3 Redshift Determination

Redshifts were calculated by fitting a quasar model to the spectroscopic data. The section of the spectra blueward of Lyα was modelled using an exponential to account for the rapid decay to zero flux. A Gaussian centred at 1025.7Å was used to approximate the Lyβ emission feature seen in some of the spectra. Lyα emission was modelled using half a Gaussian which matched onto the exponential at 1215.67Å. Redward of Lyα the NV, OI and SiIV+OIV lines were added using Gaussians centered

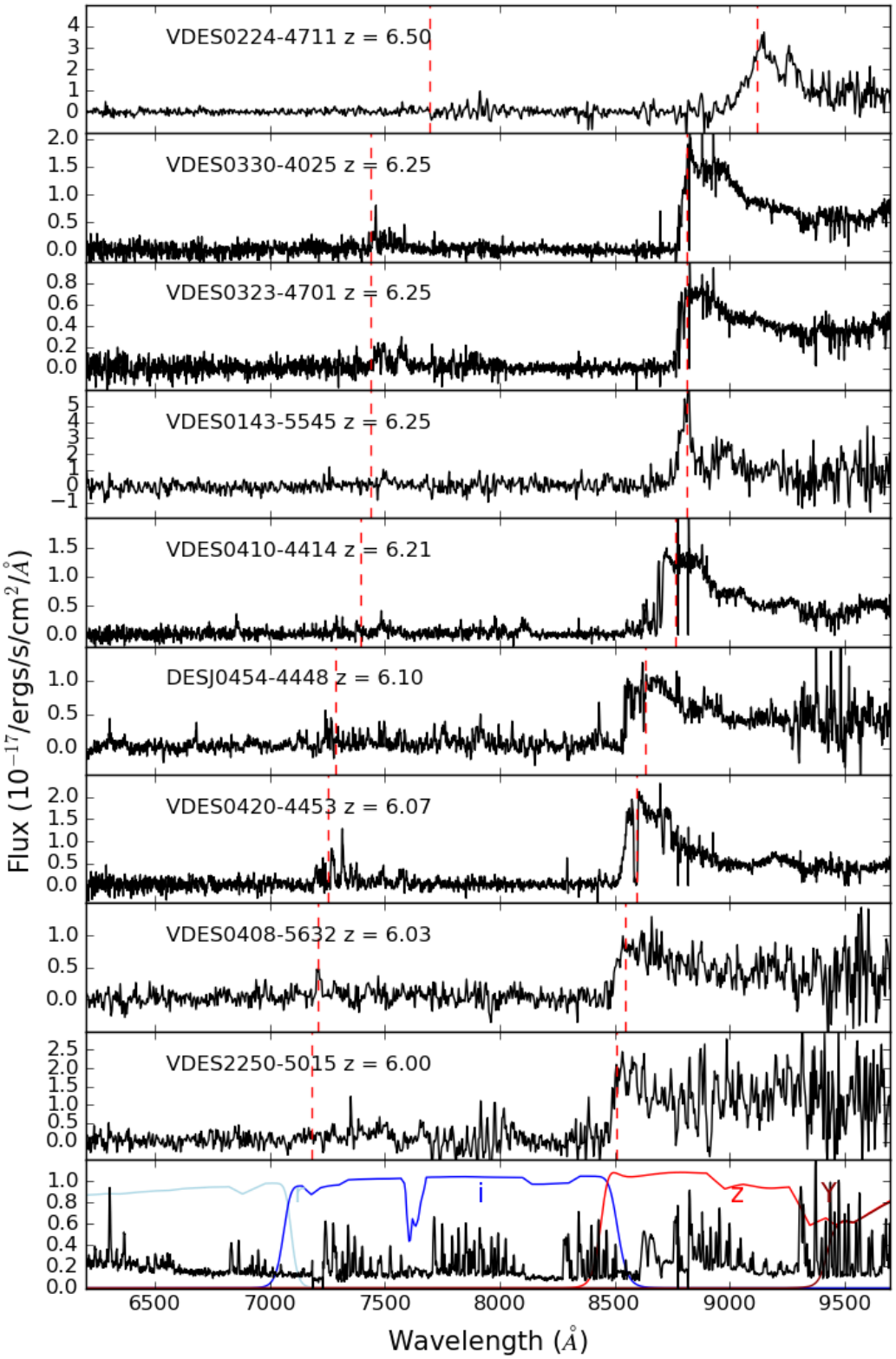

Figure 4.12 Reduced spectra of all the objects in this sample as well as the quasar discovered in Chapter 3.2 (DES J0454-4448); presented in redshift order. The vertical lines show the positions of Lyα and Lyβ. The bottom plot gives an example error spectrum taken from one of the quasars (VDES J0410-4414) and has the DES filters over plotted. Note the different y axis scales for each panel.

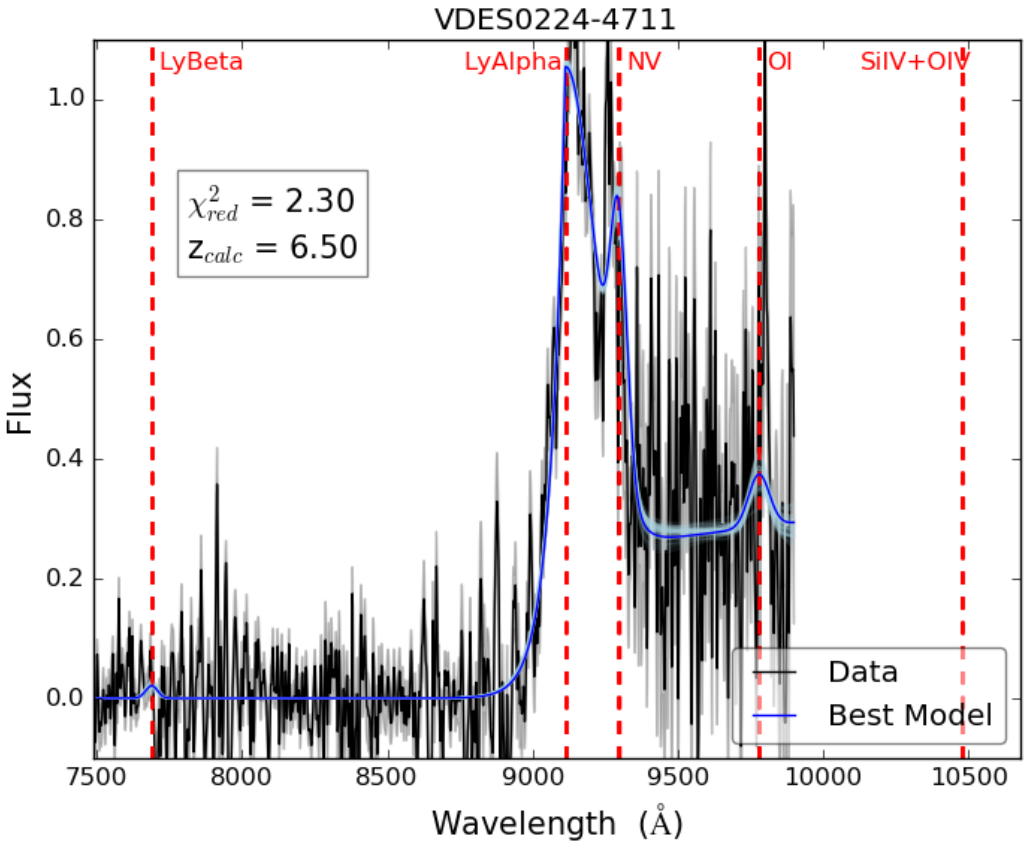

Figure 4.13 A model fit for the highest redshift quasar in this sample. The dashed lines show the centres of the lines used in the model. The data shown in black is the unsmoothed spectrum and the grey shaded area shows the uncertainty at each wavelength. The dark blue line is the best fitting model and the light blue lines show 100 example model fits found during the fitting iterations. The reduced χ^2 from the fit and the calculated redshift are given in the inset panel.

at 1240.1, 1304.46 and 1397.8 Å respectively (Tytler & Fan, 1992). The section longward of 1215.67Å then had a power law and a constant offset added, both of which were allowed to vary, to model the continuum emission.

This model was tested using the spectroscopic data from Fan et al. (2006b). While the spectroscopic data presented here do not cover the full range of lines input into the model some of the test data covered the full range. This model was then fitted to the data using a χ^2 minimisation to give the best estimate of the redshift. An example of the redshift fitting process is shown in Figure 4.13.

During these tests the method was found to recover the redshifts presented with a median difference of -0.01 with σ_{MAD} = 0.01. The σ_{MAD} (median absolute deviation (MAD)) is used as a robust estimator of the Gaussian standard deviation where σ_{MAD} = 1.4826 $\times$ MAD. σ_{MAD} was used to give an estimate of the systematic uncer-

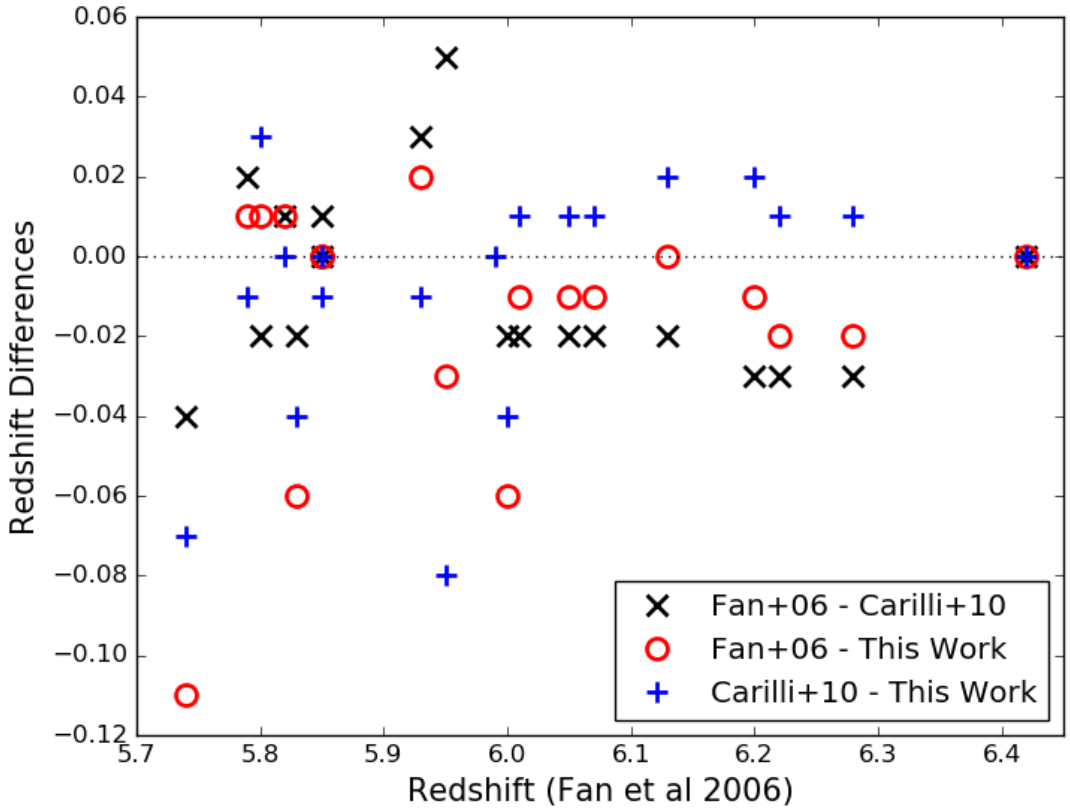

Figure 4.14 A comparison of the differences in redshifts between the fitting method used here and the results from Fan et al. (2006b) and Carilli et al. (2010). The dashed line indicates the zero line.

tainty in the redshifts of 0.01 which is far larger the statistical uncertainties from the fitting. As the data quality varies across the sample the uncertainties are going to be underestimated for the nosiest data. The calculated redshifts and the redshifts from Fan et al. (2006b) were also compared with the redshifts presented in Carilli et al. (2010); as shown in Figure 4.14. The median difference between our calculated redshifts and the redshifts from Carilli et al. (2010) was found to be 0.0 with σ_{MAD} = 0.01 while the median difference between the redshifts from Carilli et al. (2010) and Fan et al. (2006b) was -0.02 with σ_{MAD} = 0.01.

4.4 Quasar Ionization Near Zones

The observed spectra of z > 6 quasars are characterised by intrinsic quasar continuum emission and emission lines longward of the Lyα emission line in the quasar restframe. Shortward of Lyα in the quasar restframe the most distinctive feature of the spectrum

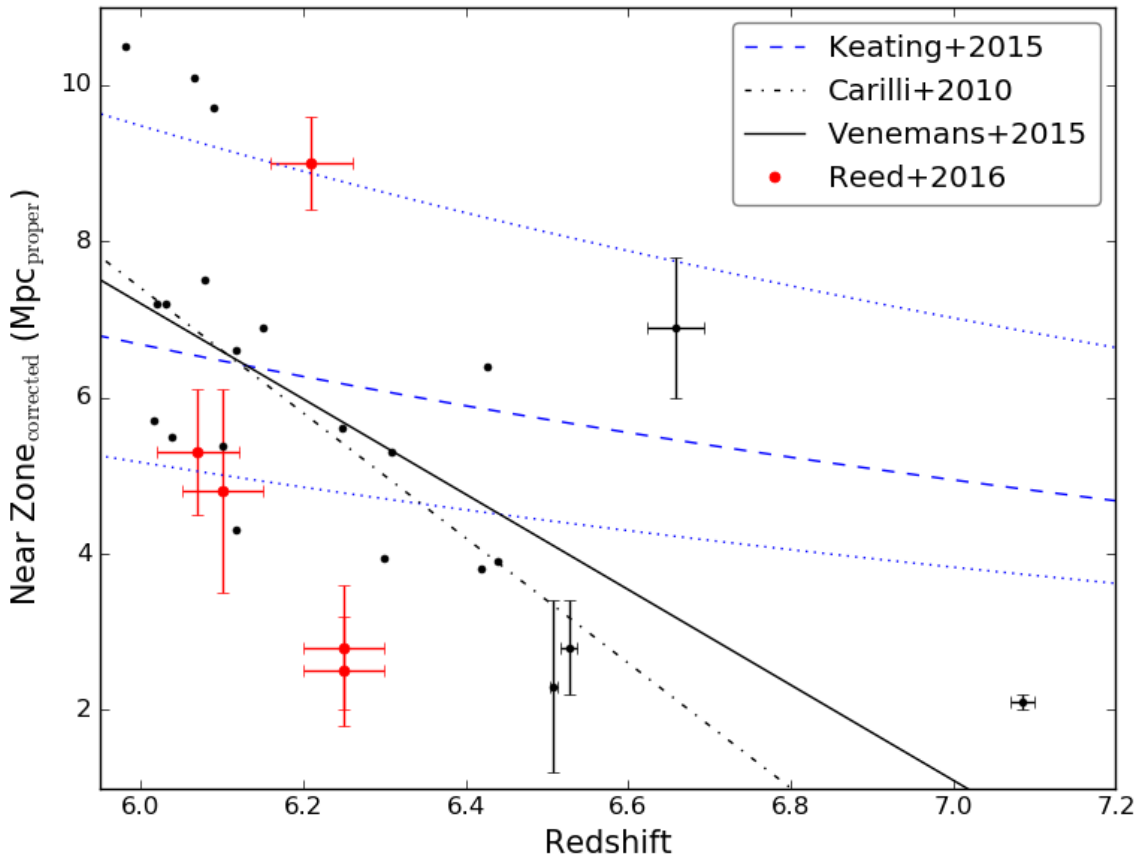

Figure 4.15 A comparison of the theoretical predictions and observations for high redshift quasar near zone sizes. The black line shows the fit to the observational data from Carilli et al. (2010) and the black dot-dashed line is the fit from Venemans et al. (2015b). The blue dashed line shows the theoretical fit from Keating et al. (2015) and the blue dotted lines are the 15$^{\text{th}}$ and 85$^{\text{th}}$ percentile for the range of near zones sizes that they found. The black points show near zone sizes from known quasars in the literature. The red points are some of the quasars in this sample. Objects with poor signal to noise spectra were not included here.

is the deficit of continuum emission due to HI Lyα and Lyman series absorption by the cosmologically distributed intervening Lyα forest. At z > 6 the optical depth from this neutral HI absorption is considerable and is often called the 'Gunn Peterson trough' where the neutral hydrogen fraction (f_{HI}) is $f_{HI} > 10^{-3}$. Closer to the quasar the UV radiation from the quasar ionizes HI and the HI opacity is decreased. This highly ionized HII region called a near zone and the size of this region is determined by the large scale structure or clumpiness of the HI, the average neutral fraction, the UV luminosity of the quasar and the age of the expanding UV radiation front emitted by the quasar. Observations of the distribution of near zone sizes and the evolution with redshift of this distribution are an important probe of the Universe in the epoch of reionisation.

Near zones sizes were calculated using the method described in Section 3.2 which follows Fan et al. (2006b) where the edge of the near zone is taken to be the point where the ratio of the observed spectra to the extrapolated continuum flux first falls below 0.1 blueward of the Lyα emission line. The spectral resolution and signal to noise of our four NTT spectra are too low to measure near zones sizes. Measured near zone sizes (R_{NZ}) from the four Gemini spectra and from VDESJ0454-4448 (Section 3.2) are presented in Table 4.7. The near zone size of a quasar in a cosmologically expanding medium will depend on the intrinsic UV flux of the quasar below the Lα transition at 1216Å. Following Carilli et al. (2010) we normalise the measured near zone sizes (R_{NZ}) to a constant UV absolute magnitude M_{1450} = –27 with the equation below.

$$R_{NZ,corrected} = R_{NZ} \times 10^{0.4(27.0+M_{1450})/3}$$

Figure 4.15 shows the distribution of corrected near zone size for 18 quasars with 6.0 < z < 6.5 from Carilli et al. (2010) and 4 z > 6.5 quasars from Venemans et al. (2015b) and Mortlock et al. (2011) along with our new sample with 6.0 < z < 6.5.

The blue dashed line is the analytic solution from Keating et al. (2015) for the evolution of the normalised near zone sizes with redshift where the quasar has constant luminosity and the neutral fraction is not evolving with redshift. The decrease in size with increasing redshift is solely due to the increase in mean HI density as the Universe gets smaller in size at earlier redshifts. The dotted blue lines show the 15^{th} and 85^{th} percentiles about the median ($\sim \pm 1\sigma$) derived from simulations (Keating et al. (2015)). The black dashed and solid lines show linear fits by Carilli et al. (2010) and Venemans et al. (2015b) respectively.

The four new near zones that we measure at 6.1 < z < 6.3 span a large range from 3 to 9 Mpc. Two, VDES J0330-4025 and VDES J0323-4701, have relatively small corrected near zone sizes of $\sim$3 Mpc which could indicate that these two quasars are younger than the average quasar at this epoch and have relatively small lifetime ($10^6 - 10^7$ years) and the ionized HII regions have not reached their maximum size due to the time taken for the ionizing radiation fronts to expand into the surrounding HI region. Alternatively if one ignores the effects of quasar lifetime to fully account for the small near zone sizes the objects would need to be situated in regions of the Universe which are a factor of $\sim$10 above average HI density. Similar effects has been reported by Bolton et al. (2011) for the z = 7.085 quasar ULAS J1120+0641. The discovery of two z $\sim$ 6.2 quasars with such small near zones indicates that care needs to taken in interpreting small near zones as evidence for an increase in the neutral fraction. To further address this more observational data is essential.

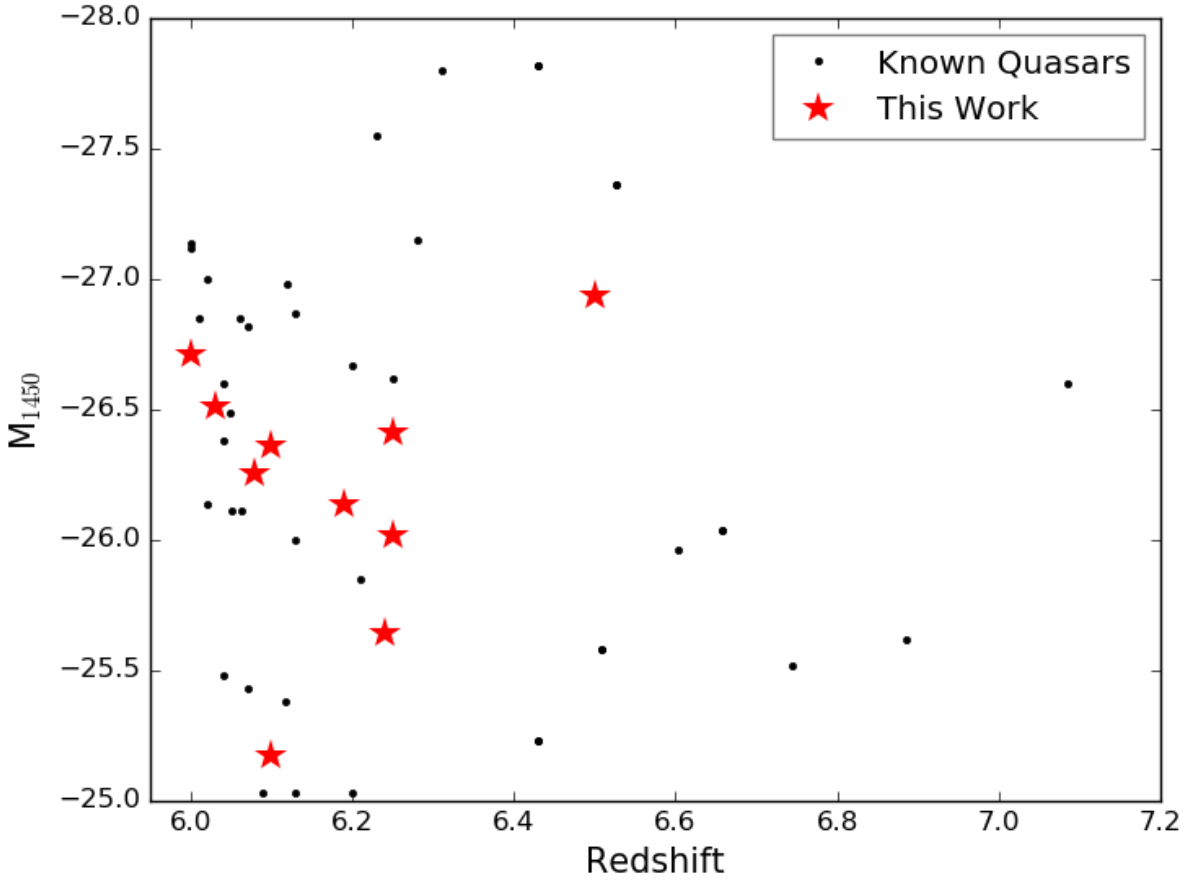

Figure 4.16 Here the absolute magnitude calculated at 1450Å in the restframe is shown against redshift. The M_{1450} was estimated from the Y band magnitude of the objects.

4.5 Properties of Individual Objects

This Section gives more details on some specific objects from this sample. A summary of the derived properties of the quasars presented here is given in Table 4.7. A comparison of these to known quasars is shown in Figures 4.16 and 4.17.

4.5.1 VDES J0143-5545 (z = 6.23)

VDES J0143-5545 was followed up with the NTT and found to have a very strong emission feature at ∼8820Å suggestive of a quasar with z ∼ 6.3. This object was well fit by the model with the highest level of reddening, E(B-V) = 0.100, at z = 6.1. This object has a very blue z - Y of -0.61 due to the presence of the very strong Lyα emission line in the z filter. When the reddening fit was repeated without using the blended *WISE* data the object was best fit by a model with E(B-V) = 0.025 suggesting

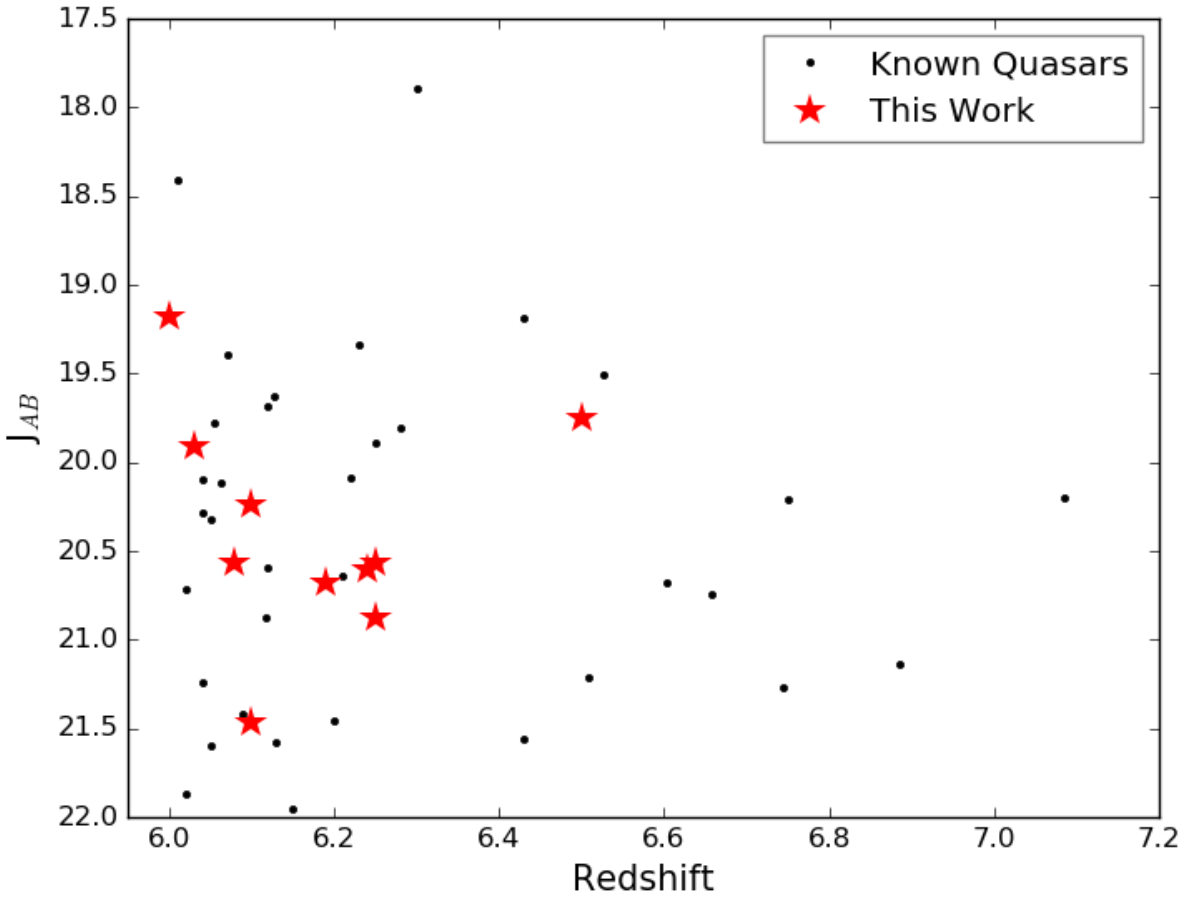

Figure 4.17 The apparent AB magnitude of these quasars in the J band is shown against their redshifts compared with known quasars.

Table 4.7 Derived properties of the quasars in this sample. The near zone sizes for VDES J0454-4448 are taken from Chapter 3. Near zone sizes are not given for all objects as the data quality was not good enough.

Name	Redshift	M_{1450}	R_{NZ}	$R_{NZ,corrected}$
VDES J0143-5545	6.25 ± 0.01	-25.65 ± 0.12		
VDES J0224-4711	6.50 ± 0.01	-26.93 ± 0.05		
VDES J0323-4701	6.25 ± 0.01	-26.02 ± 0.07	$2.1\,^{+0.6}_{-0.5}$ Mpc	$2.8\,^{+0.8}_{-0.7}$ Mpc
VDES J0330-4025	6.25 ± 0.01	-26.42 ± 0.06	$2.1\,^{+0.6}_{-0.5}$ Mpc	$2.5\,^{+0.7}_{-0.6}$ Mpc
VDES J0408-5632	6.03 ± 0.01	-26.51 ± 0.05		
VDES J0410-4414	6.21 ± 0.01	-26.14 ± 0.09	$6.9\,^{+0.5}_{-0.5}$ Mpc	$9.0\,^{+0.6}_{-0.7}$ Mpc
VDES J0420-4453	6.07 ± 0.01	-26.25 ± 0.06	$4.3\,^{+0.6}_{-1.0}$ Mpc	$5.3\,^{+0.8}_{-1.2}$ Mpc
VDES J0454-4448[†]	6.10 ± 0.01	-26.36 ± 0.05	$4.1\,^{+1.1}_{-1.2}$ Mpc	$4.8^{+1.3}_{-1.4}$ Mpc
VDES J2250-5015	6.00 ± 0.01	-26.80 ± 0.04		

[†]This object was found in Chapter 3.

that the W1 and W2 fluxes are affected by a nearby source.

4.5.2 VDES J0224-4711 (z = 6.50)

This candidate was ranked as the third most likely object to be a quasar in the candidate list with a very good fit to a reddened quasar model (E(B-V) = 0.05) at z $\sim$ 6.4. It is quite bright with z = 20.0 and has a very red i – z colour of 3.82. Follow up of this object with the NTT showed a strong emission feature starting at $\sim$9100Å giving a redshift of 6.50. The reddening fit was recalculated with the redshift fixed at the observed spectroscopic redshift of 6.50. At the spectroscopic redshift the photometry was best fit by a reddened model with E(B-V) = 0.05. This object appears to have a very extended near zone but the modest quality of the spectral data means that this measurement has very large uncertainties. This is discussed further in Chapter 5. VDES J0224-4711 has J_{AB} = 19.75 and is the second most luminous quasar known with z $\geq$ 6.5 and is 0.2 magnitudes fainter than the most luminous quasar know with z > 6.5; PSO J0226+0302 with z = 6.53 and J_{AB} = 19.51 Venemans et al. (2015b).

4.5.3 VDES J0323-4701 (z = 6.25)

VDES J0323-4701 was the lowest ranked candidate followed up. Spectroscopic observations with GMOS revealed a quasar at z $\sim$ 6.25. This object had a very red i - z colour of 3.52 and was best fit by a non reddened quasar model with a slightly lower redshift of 6.10 than the spectroscopic one. The measured corrected near zone size of 2.8 proper Mpc which could indicate above average IGM density or a young age for this quasar.

4.5.4 VDES J0454-4448 (z = 6.10)

VDES J0454-4448 was the first z $\sim$ 6 quasar identified from DES and was the subject of Chapter 3.2; details of the spectroscopic observations are included therein. It is included here as it was covered again by the year one release from DES and was the second highest ranked candidate in the independent data analysis in this paper. The redshift was recalculated for this object as part of this analysis and was found to be 6.10 $\pm$ 0.01 which is consistent with the previous value given of 6.09 $\pm$ 0.03.

4.5.5 VDES J2250-5015 (z = 6.00)

This object was ranked fourth by the selection code with a good fit to a model with E(B-V) = 0.05 and a predicted redshift of 6.0. Follow up spectroscopy with the NTT gives a redshift of 6.00. This source was the brightest in our sample with z = 20.11. VDES J2250-5015 has a fairly red i - z colour of 2.52 and has a very red Y - J colour of 0.80. The reddening fit was repeated with the redshift fixed at the calculated one and without using the *WISE* data as the close proximity of another source might be influencing this. This resulted in a model with more reddening (E(B-V) = 0.1) being chosen as the best fit. The red Y - J colour of this object could be due to the reddening.

4.5.6 VDES J2315-0023 (z = 6.12)

The seventh mostly likely ranked candidate was a known quasar (SDSS J231546.57-002358.1) from the SDSS survey for quasars in stripe 82 (Jiang et al., 2008). Their spectroscopic follow up found it to have z = 6.117 which is slightly higher than our photometric estimate of 6.0.

4.6 Analysis of Selection Method

There are seven previously known quasars with $z \geqslant 5.80$ in the area covered by the data used in this study. Two are recovered by the selection criterion, VDES 0454-4448 (z = 6.10) and SDSS J2315+0023 from Jiang et al. (2008) as discussed in section 4.5. The z = 5.8 quasar, SDSS J000552.34000655.8, discovered in Fan et al. (2004) is bluer than the i_{DES} - z_{DES} selection used here and is not selected. This colour is indicative of being at a lower redshift than this selection method probes. The three quasars in Jiang et al. (2009) and the radio selected z = 5.95 quasar (SDSS J222843.54+011032.2) Zeimann et al. (2011) that overlap the area have $z_{DES} > 21.0$ and therefore are fainter than the selection limit used here. A selection limit of $z_{DES} > 21.0$ was used as this selected only objects that were bright enough to be useful for follow up studies. It also reduced the number of candidates that passed the selection while the method was being developed and tested.

The automatic ranking of candidates in the candidate list allows visual inspection to be prioritised. This will be particularly useful once the full DES area is available for study as there will be a large number ($\sim$500) of candidate objects. This also means that looser colour cuts can be used to narrow down the data slightly allowing more

unusual objects to be discovered. One such object is VDES J2250-5015 whose red colour in Y - J would have caused it to be rejected by previous searches (Bañados et al. 2016; Venemans et al. 2015a). The Y and J band photometry of VDES J2250-5015 is reliable and suggests that the very red colour is real and due to intrinsic properties of the object.

The SED model fitting selection method presented here also allows the expansion of the candidate list without increasing the need for visual inspection as objects can be assesed in ranked order. This is because most of the types of junk (cosmic rays, bleed trails, saturation issues etc) that contaminate the list are classified as very unlikely to be quasars. The astrophysical contaminants of the list (primarily cool stars) are also down weighted through this method. The future aim of this work is to be able to run the selection criteria over the entire catalogue without any need for colour cuts and using the reduced χ^2 fits as discriminators. At the moment the colour selection is required to narrow down the list enough to make the image based steps run more rapidly. Improvements in the analysis code will allow this to be done for a larger number of images more rapidly. The catalogue based steps and the fitting steps are both fast enough (10^8 sources from $\sim$1500 deg^2 in less than 24hr on a single 4Ghz core) that they will be easily expanded to the larger $\sim$5000 deg^2 DES dataset when it is released. Figures 4.18 and 4.19 show the fits for the full range of models used in this work for the highest ranked quasar and the highest ranked brown dwarf.

In this version of the selection code objects with a high probability of being a brown dwarf are not rejected automatically but removed on an object by object basis during visual inspection. An improvement to the method would be to have automatic removal of these objects, as this will be more important for larger candidate lists generated either by relaxing the colour cuts or by a larger input dataset. For this selection it was not fully understood which cuts would automatically remove cool stars as there was only a small sample to test the selection method on. Therefore the removal was done on an object by object basis. The confirmed quasars compared to the rest of the sample are shown in terms of reduced χ^2 to be either a star or a quasar in Figure 4.20. It can be seen that the selected objects are well separated from the rest of the sample. Due to the inclement weather we did not have time to follow up any objects further down the ranking so do not know if the dashed lines should be relaxed to select a complete sample. The candidates in the bottom right region are junk (such as cosmic rays and objects effected by saturation) as confirmed by visual inspection.

In Section 4.1.2 our implemented SED fitting included an arbitrary systematic flux uncertainty. Now we have a spectroscopically confirmed sample we analyze the residuals from the best fit models. In Figure 4.21 we show the ratio of the observed flux to

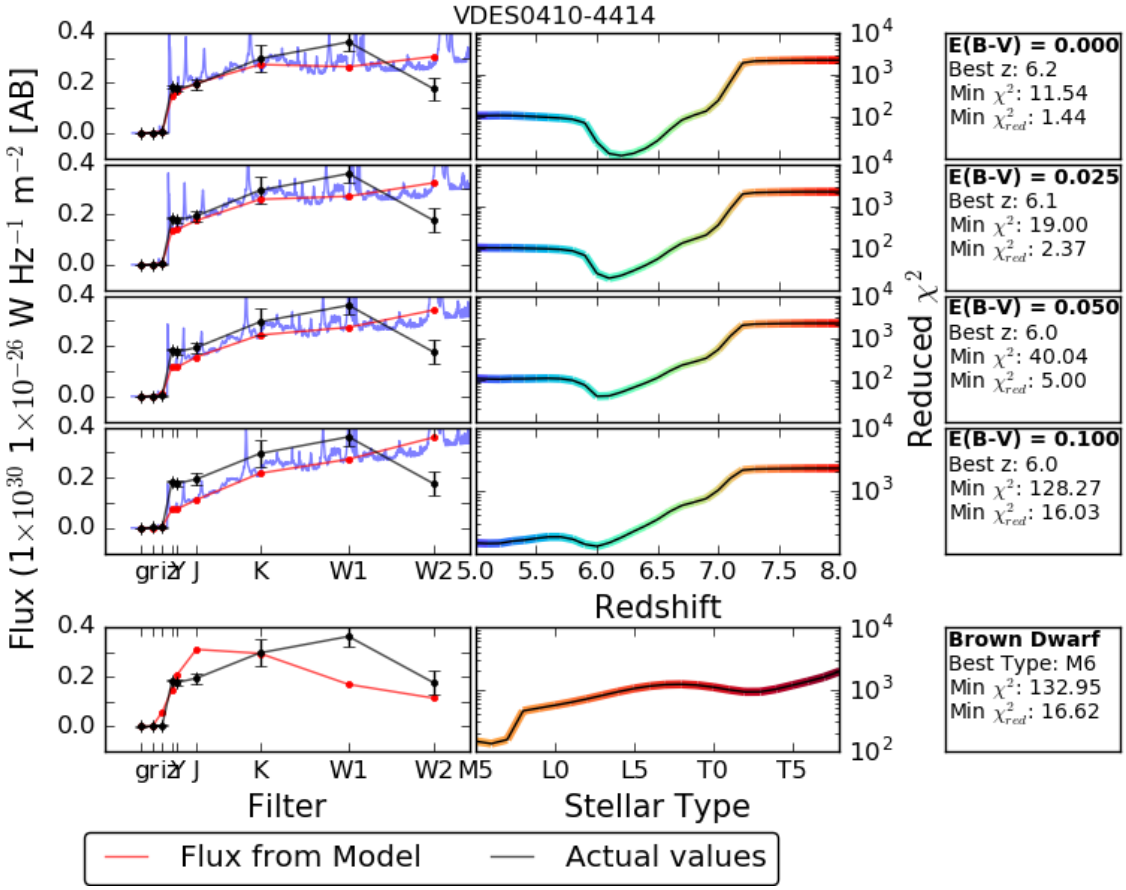

Figure 4.18 An example of the fitting results for the highest ranked quasar in the sample. The four different reddening models and the brown dwarf fit are shown in the left column of plots and the right column shows the reduced χ^2 fits for the range of redshifts/models considered. The brown dwarf model is clearly different to any of the quasar models. Note the different scales on the χ^2 plots.

the best fitting model flux for each quasar, the sample median and the σ_{MAD}. These show that the best fit models agree within the uncertainties.

The scatter in the flux ratios as described by the σ_{MAD} is shown in Figure 4.21. The values for these ratios in the bands that are unaffected by the Lyα forest are similar to the values assumed in the fitting as described in Section 4.1.2. In r and i the large scatter is from stochastic scatter in Lyα forest and photometric statistical errors. In a future paper with a larger sample of confirmed quasars we will investigate the scatter in terms of the model. There is some evidence for excess flux in the W1 band which is probably due to the large aperture used resulting in flux from neighbouring objects. Since quasars are redder in W1 - W2 than the foreground galaxy and stellar populations, the W2 band is less affected.

Figure 4.22 shows the absolute continuum magnitude at a rest frame wavelength of 1450Å calculated from each of the four model quasar spectra used in this work.

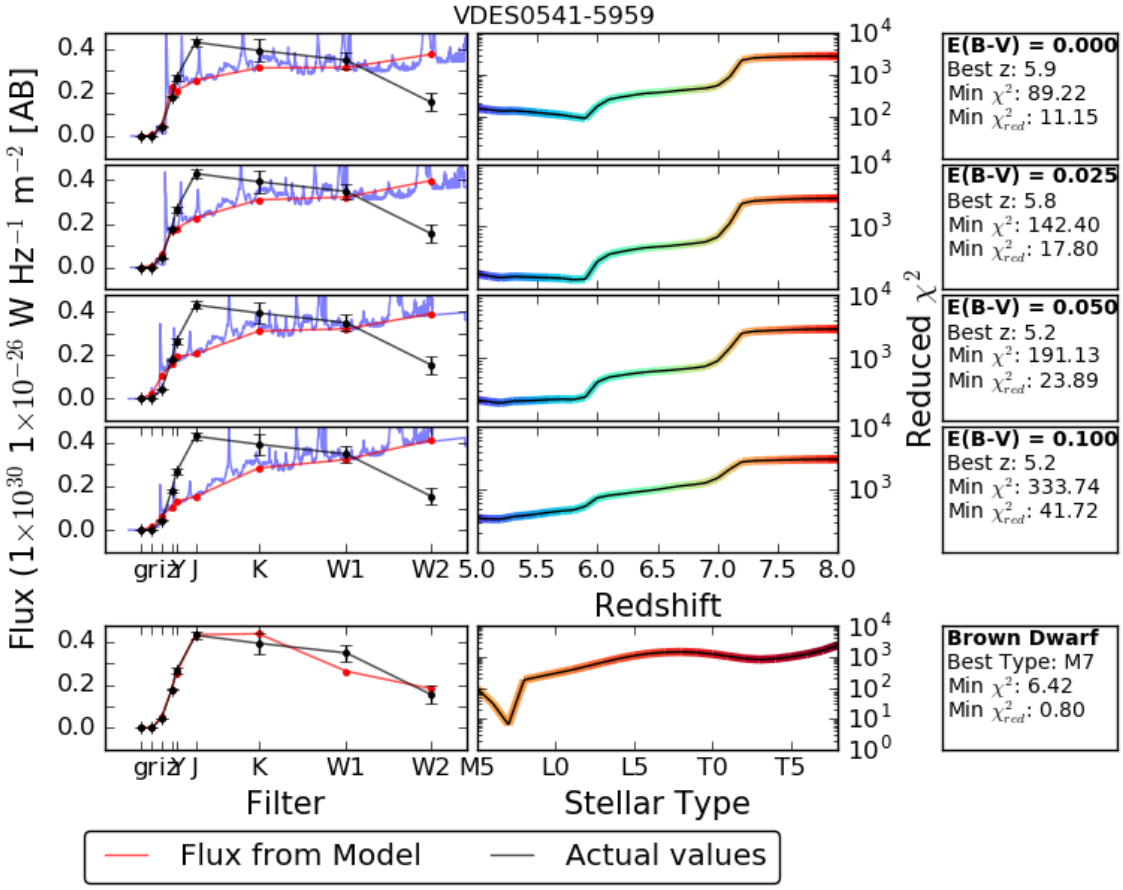

Figure 4.19 An example of the fitting results for a probable brown dwarf found in the sample. The four different reddening models and the brown dwarf fit are shown in the left column of plots and the right column shows the reduced χ^2 fits for the range of redshifts/models considered. It can be seen that the brown dwarf model is closer to the data than any of the quasar models. Note the different scales on the χ^2 plots.

For this calculation the models were scaled to have an observed integrated z band magnitude of 21.0. This figure shows that higher redshift objects need to be intrinsically brighter to still pass the magnitude limit for this selection. The selection criteria presented here is not designed to select objects above z $\sim$ 6.5 due to the z - Y colour limit shown in Figure 4.1.

The code is written to allow different models to be easily inserted and tested meaning that as additional models become available we can also compare to these. This will allow a wider variety of quasar types to be searched for. For example include models with a wider range of extinctions and at a finer sampling in extinction and redshift will be included. Different treatments of the Lyα forest and different properties of the IGM can also be incorporated.

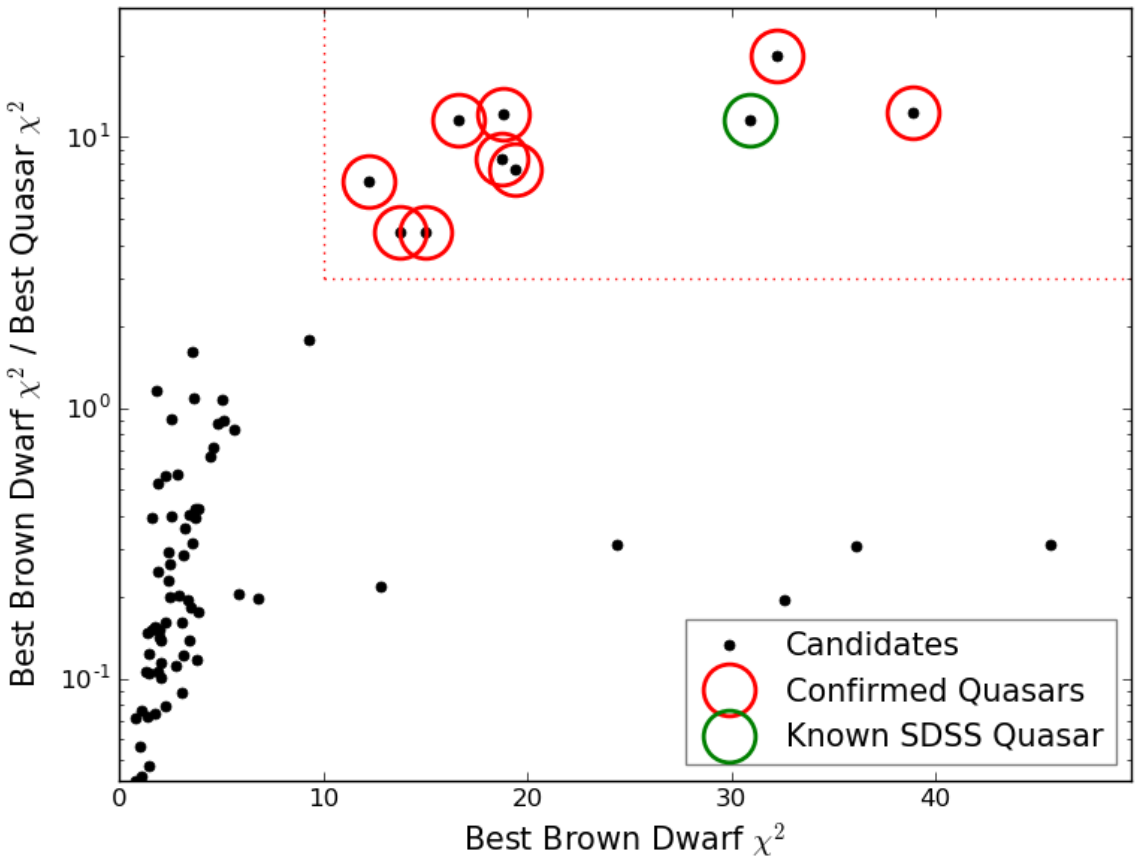

Figure 4.20 The known quasars were used to derive cuts to automatically select quasar candidates. These cuts are shown as the red dotted lines. The points circled in red are DES quasars and the object circled in green is a known SDSS quasar. It can be seen that these cuts separate the known quasars well from the rest of the sample. Due to inclement weather the object between the locus of points and the delimited box has not been followed up.

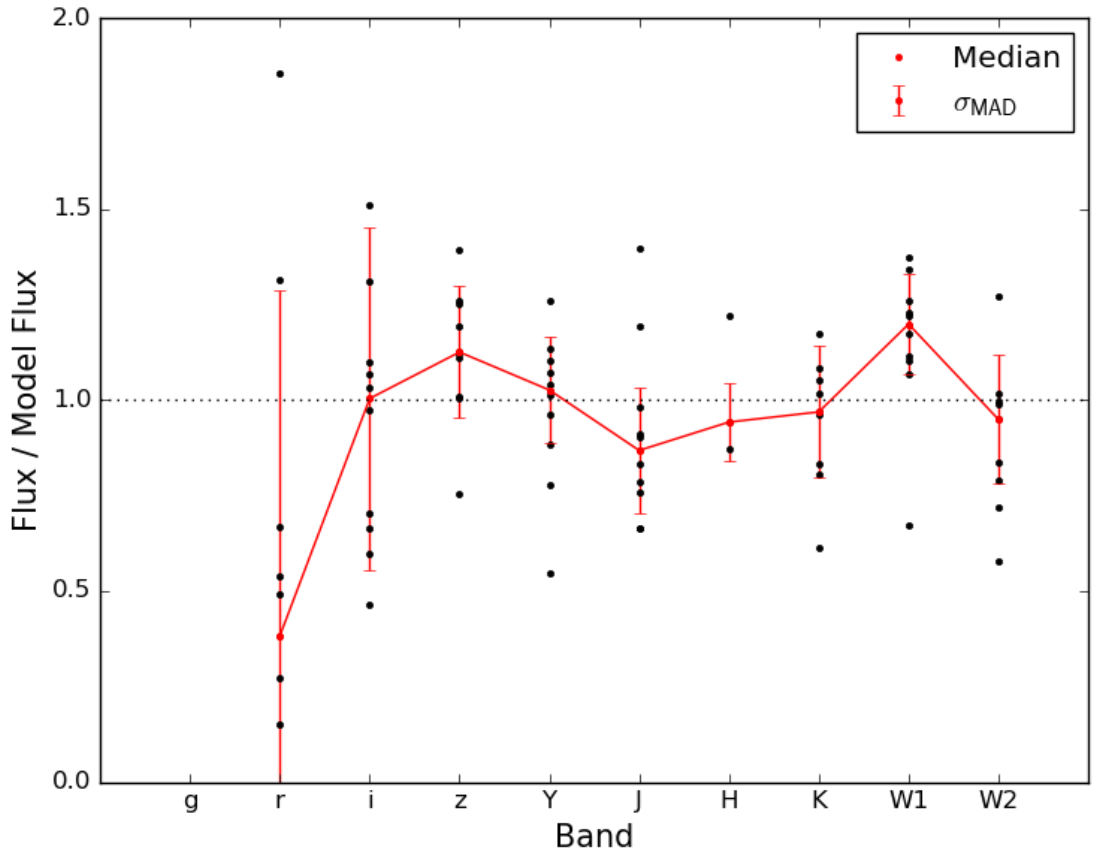

Figure 4.21 The black points are the measured flux values for the sample of 10 quasars divided by the flux derived from the best fitting model. The red points are the medians of the ratio values in each band. The red error bars show the 1σ uncertainty derived from the median absolute deviation. No g band is shown as the model flux was mostly zero.

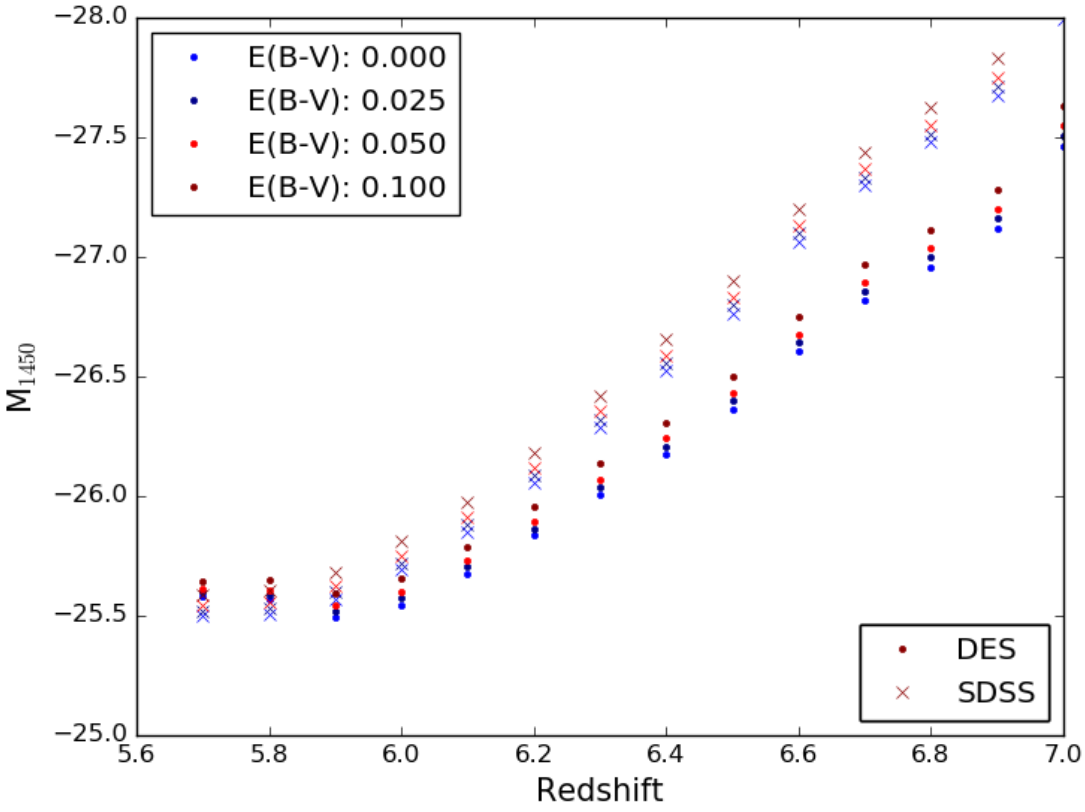

Figure 4.22 The absolute magnitude at 1450Å for our four quasar models shown over a range of resdhifts. The models were scaled to have a z band magnitude of 21.0

Table 4.8 Database properties of the quasars in the Y3 sample.

Name	Ranking	DES Tilename	DES RNUM	DES PNUM	RA (J2000)	DEC (J2000)
VDES J0109-5424		DES0110-5414	r2628	p01	17.28742	-54.40451
					$01^h09^m08.98^s$	-54°24'16.2"
VDES J0122-4609		DES0122-4623	r2624	p01	20.74034	-46.15393
					$01^h22^m57.68^s$	-46°09'14.1"
VDES J0131-3841		DES0130-3832	r2624	p01	22.83261	-38.69474
					$01^h31^m19.83^s$	-38°41'41.1"
VDES J0433-5205		DES0433-5205	r2683	p01	68.31807	-51.89394
					$04^h33^m16.34^s$	-51°89'39.4"
VDES J0532-4401		DES0533-4414	r2689	p01	83.10404	-44.02239
					$05^h32^m24.97^s$	-44°01'20.6"

Table 4.9 Magnitudes of the quasars in the Y3 sample. Upper limits for the g and r bands are the median 2 σ limit for a 2 arcsecond aperture in that tile of DES data. The Ks band magnitude limit is the 50% completeness depth for the survey. Data is not included when the object was not covered by in that survey. All magnitudes are given in AB. W1 and W2 magnitude limits are given as the 2 σ limiting depth for the *ALLWISE* survey. The magnitudes shown here are from the published catalogues rather than the forced photometry catalogues.

Name	g	r	i	z	Y	J	Ks	W1	W2
VDES J0109-5424	24.47 $\pm$ 0.20	22.94 $\pm$ 0.05	22.60 $\pm$ 0.07	19.90 $\pm$ 0.01	19.52 $\pm$ 0.02	19.49 $\pm$ 0.04	18.87 $\pm$ 0.05	19.12 $\pm$ 0.05	18.72 $\pm$ 0.08
VDES J0122-4609	25.62 $\pm$ 0.45	23.84 $\pm$ 0.10	21.64 $\pm$ 0.02	19.84 $\pm$ 0.01	19.90 $\pm$ 0.03	19.69 $\pm$ 0.08	19.36 $\pm$ 0.10	19.41 $\pm$ 0.08	19.40 $\pm$ 0.14
VDES J0131-3841	> 26.11	24.56 $\pm$ 0.21	22.49 $\pm$ 0.05	20.10 $\pm$ 0.01	20.20 $\pm$ 0.04	-	-	20.21 $\pm$ 0.15	19.85 $\pm$ 0.23
VDES J0433-5153	> 26.11	24.97 $\pm$ 0.26	23.02 $\pm$ 0.20	21.24 $\pm$ 0.03	20.65 $\pm$ 0.06	19.69 $\pm$ 0.08	19.58 $\pm$ 0.13	19.31 $\pm$ 0.05	19.42 $\pm$ 0.09
VDES J0532-4401	> 26.08	> 26.01	22.68 $\pm$ 0.06	20.96 $\pm$ 0.02	20.96 $\pm$ 0.11	20.79 $\pm$ 0.14	> 19.52	> 20.35	> 20.05

Table 4.10 Derived properties of the new quasars in the Y3 sample. Calculation and discussion of the near zone sizes is left for Chapter 6

Name	Redshift	M_{1450}
VDES J0109-5423	6.09 ± 0.01	-25.65 ± 0.12
VDES J0122-4609	6.00 ± 0.01	-26.93 ± 0.05
VDES J0131-3841	6.01 ± 0.01	-26.02 ± 0.07
VDES J0433-5153	5.97 ± 0.01	-26.42 ± 0.06
VDES J0532-4401	5.97 ± 0.01	-26.51 ± 0.05

4.7 DES Y3 Selection

The SED based selection method formulated in this Chapter was expanded and applied to the DES Y3 data release (detailed in Section 2.2.4). For this selection the colour and magnitude cuts were relaxed and an automated method to remove cool stars was used. The method was based on the box shown in Figure 4.20 and applied cuts in χ^2 to select the candidates most likely to be quasars. The selection lead to the discovery of five new $z \sim 6$ quasars and the rediscovery of 13 previously known ones. The properties of the new objects are given in Tables 4.8, 4.9 and 4.10 and their spectra are shown in 4.23.

These objects were observed using the NTT between the 22nd and 25th December 2016. The data was reduced in a similar manner to that which is detailed earlier in this Chapter for the 2015 data but with a minor change made to the object tracing method. The slight change made to the pipeline is covered in Chapter 5.3.

Relaxing the selection and using the fitting results to select the candidates for follow up resulted in the selection of objects with a wider variety of properties. For example VDES J0109-5423 has flux detected in the r band with an error of less than 0.1 and would therefore not have passed our initial selection.

4.8 Web Interface

To allow reproducible visual inspection and classification of candidates a database driven web interface was created. This allowed multiple people to record classifications and comments for individual objects that could then be compared and shared. The web interface is an easy to use wrapper on a SQL database that grants users the ability to easily select subsets of the data for more detailed study. The website is discussed further in Appendix A.3. This interface, and other library code developed

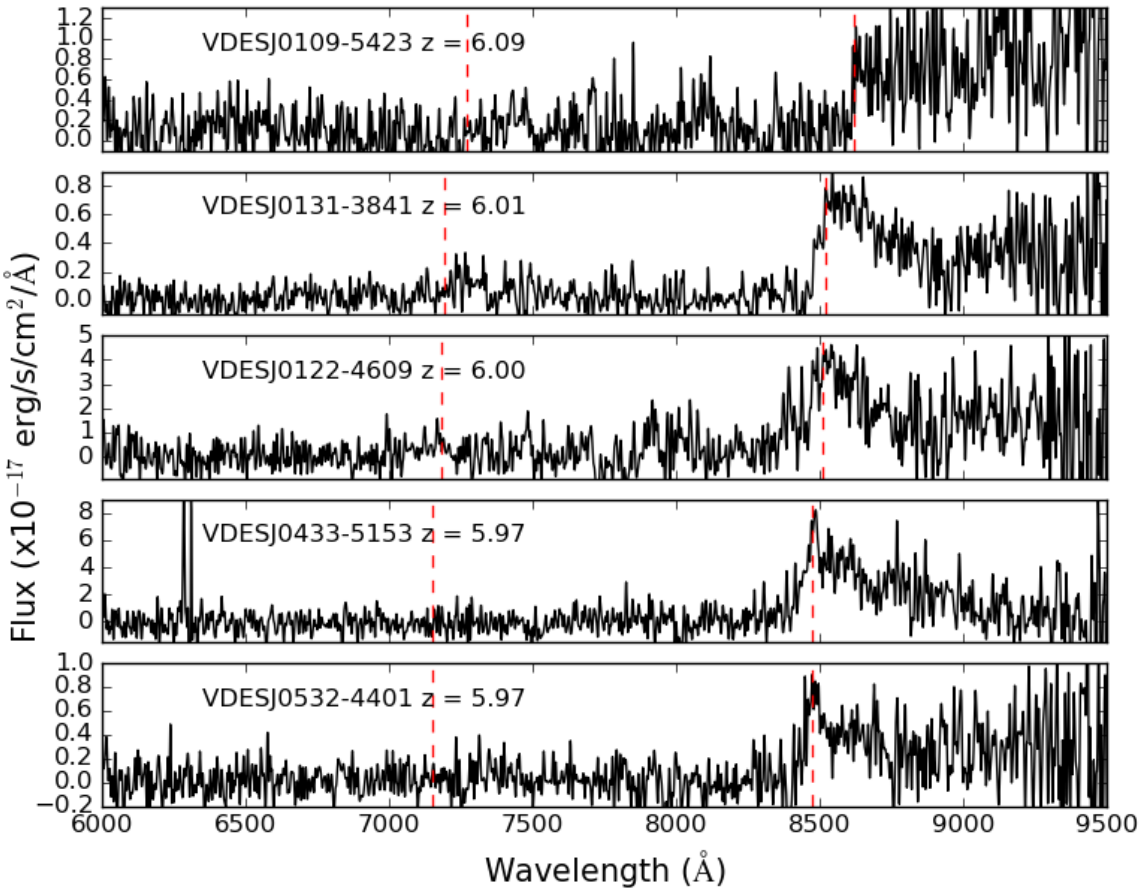

Figure 4.23 The spectra of the 5 new DES quasars from Y3. The vertical, dashed, red lines show the positions of Lyα and Lyβ in the observed frame of the quasar.

during this Thesis, are used as part of ongoing lensed quasar and high redshift galaxy searches.

4.9 Discussion

The number density of z $\sim$ 6 quasars found in this work is compared to previous studies to investigate the completeness of the sample. The most similar of the SDSS quasar surveys to our selection is the method used in Jiang et al. (2008) which found a complete sample between 5.8 < z < 6.5 down to a z band magnitude of 21. Of the 6 quasars they found in 260 deg^2 4 are high enough redshift to be selected by our criteria. This gives a number density of 1 per 65 deg^2. From the CFHT selection there are 2 quasars that would pass our criteria (the rest are fainter than the z < 21 magnitude limit used or at redshifts lower than 5.9) from 498 deg^2 leading to a number density of 1 per 249 deg^2. The selection from the Y1 data in this Chapter found 10 objects in 1533 deg^2 resulting in a number density of 1 per 153 deg^2. This density is

between the number densities of these two previous surveys. The completeness of our search at the low redshift and bright end is not well characterised as the DES data goes deeper than previous surveys and bright sources with Lyα forest transmission are being found to have r band flux. This flux can be picked up in the deep imaging and can cause the objects to fail the $\sigma_r > 0.1$ selection cut. The Y3 observing run loosened the initial magnitude cuts and found 4 other quasars in the Y1 area bringing the number density to 1 per 102 deg^2. The number density of quasars found during this work is very promising considering that the completeness is not fully understood yet and that the spectroscopic observations are not yet complete. The completeness is expected to improve with additional, deeper J band data and through relaxing the χ^2 cuts used to narrow down the candidate list.

4.10 Summary and Conclusions

The photometric selection, statistical classification and spectroscopic confirmation of 13 new high redshift 6.0 < z < 6.5 quasars with $z_{AB} < 21.0$, selected without any morphological star-galaxy classification from $\sim$1500 deg^2 using SED model fitting to photometric data from the Dark Energy Survey (g, r, i, z, Y), the VISTA Hemisphere Survey (J, H, K) and the Wide-Field Infrared Survey Explorer (W1, W2) have been presented. Starting from over 100 million photometric sources we used objective and repeatable machine based techniques to select 147 quasar candidates. Probable cool stars were then removed based on their photometric classification and the candidates ranked before they were observed. Candidates were then visually inspected in their ranked order and those that passed observed. The spectral confirmation success rate is 100% for this search without the need for follow up photometric observations as used in other studies of this type. Combined with automatic removal of the main types of non-astrophysical contaminants the method allows large data sets to be processed without human intervention and without being over run by spurious false candidates. The highest redshift quasars with z = 6.5; VDES J0224–4711 which has $J_{AB} = 19.75$ is the second most luminous quasar known with $z \geq 6.5$ and is 0.2 mag fainter than the most luminous quasar know with z > 6.5; PSO J0226+0302 with z = 6.53 and J_{AB} = 19.51 Venemans et al. (2015b).

Candidates were ranked based on the ratio of reduced χ^2-statistic values for the best fit quasar model compared to the best fit stellar model. This approach is expandable to other photometric systems and imaging surveys (e.g. LSST, Euclid), in contrast to selections based solely colour cut based criteria widely used in other high redshift quasars searches. This method was then extended to use very relaxed selec-

tion cuts and the candidates selected for follow up based off the results of the fitting method. The relaxed selection also had a 100% success rate and found quasars that were missed by the first selection used in this Chapter.

A new quasar redshift determination algorithm has been developed based on the onset of the Lyα forest and a fit to the Lyα emission line using a semi-Gaussian and an exponential. The technique is validated on a sample of quasars that also have CO and MgII emission line redshifts from Carilli et al. (2010) and it is found that the empirical fitting technique has a median difference of 0.00 and the distribution has σ_{MAD} = 0.01.

5

Selection of Quasars with Redshifts > 6.5 and their Emission Line Properties

Quasars above z = 6.5 are even rarer than those between 6.0 and 6.5 but are scientifically more interesting as they give more constraints on reionisation. For previous surveys the redshift range that quasars could be found at was limited by the wavelength coverage of the detectors. The maximum redshifts achieved by previous successful surveys for z > 6 quasars were z = 6.43 for CFHT (CFHQS J2329-0301, (Willott et al., 2007)) and z = 6.43 for SDSS (SDSS J114816.64+525150.3, (Fan et al., 2003)). To increase the accessible redshift range IR surveys have been used to search for z > 6.5 quasars. Venemans et al. (2013) used the near IR survey VIKING, which had photometry in z, Y, J, H and K, to find three new z > 6.5 quasars. Due to the lack of overlapping optical data this search required deep optical follow up photometry to be taken to remove low redshift interlopers from the selection. Mortlock et al. (2011) found the quasar (ULAS J1120, z = 7.085) using a combination of IR data from UKIDSS and optical data from SDSS. DES is the first optical CCD based survey to be sufficiently red sensitive to have a Y band suitable for finding quasars with z > 6.5.

By searching for objects that drop out in z - Y colour in DES the redshift range 6.5 < z < 7.2 can be accessed. To find these objects a similar method is used to that detailed in Chapters 3 and 4. This chapter focusses on the adaptation of these two methods to work at higher redshift. The second part of the Chapter will then discuss the reduction of the infra red spectroscopic data taken of confirmed z $\geq$ 6.5 quasars and what can be learnt from it.

5.1 The First z > 6.5 Quasar From DES

In December 2015 the Year 1 (Y1) data from DES was released to the collaboration. This covered about 1500 deg^2 and was a large enough area that, based off numbers found in previous searches, it was probable to find a bright z > 6.5 quasar. For example in Mortlock et al. (2011) they found one quasar with z > 6.5 in 2,250 deg^2.

5.1.1 DES Y1 Data

The DES Y1 data is discussed fully in Section 2.2.3 and the data used for the first selection at z > 6.5 is the same dataset as was used for the work discussed in Chapter 4. The data are summarised again here. The DES Y1 data cover $\sim$1840 deg^2 of the southern sky to median 10σ point source depths of 23.3, 23.6, 23.1, 22.3 and 20.8 (AB) in the g, r, i, z and Y bands respectively. This data was then reduced by DES data management using SExtractor (Bertin & Arnouts, 1996) in double image mode with a detection image created from a combination of the r, i and z band images. This detection image is sub-optimal for z > 6.5 selection and is discussed further in Section 5.2.2.

5.1.2 Initial Selection

The initial search was performed using a modified version of the method presented in Chapter 3. As in the search for the first z > 6.0 quasar PSF and model magnitudes were used both of which were produced by the DES data management team as part of the Y1 pipeline that processed the data.

The drop out technique used to find objects at z $\sim$ 6 can be extended to find objects at higher redshift. The prominent Lyα peak and the deep absorption trough from the IGM are now redshifted further into the near IR. This means that these objects drop out between the z and Y bands rather than the i and z bands giving rise to a distinctive z - Y colour. For this search the primary selection was a z - Y cut of z - Y > 0.5 which may seem much less dramatic than the corresponding i - z cut used in Section 3.1.2 but due to the overlap in wavelength coverage of the z and Y filters objects have to be at very high redshift before they fully drop out of z. This overlap can be seen in Figure 5.1.

The first step to clean up the catalogue was to apply the flag based cuts described in Section 3.1.1 and then to apply a Y band limit of 21.5 to give a clean flux limited

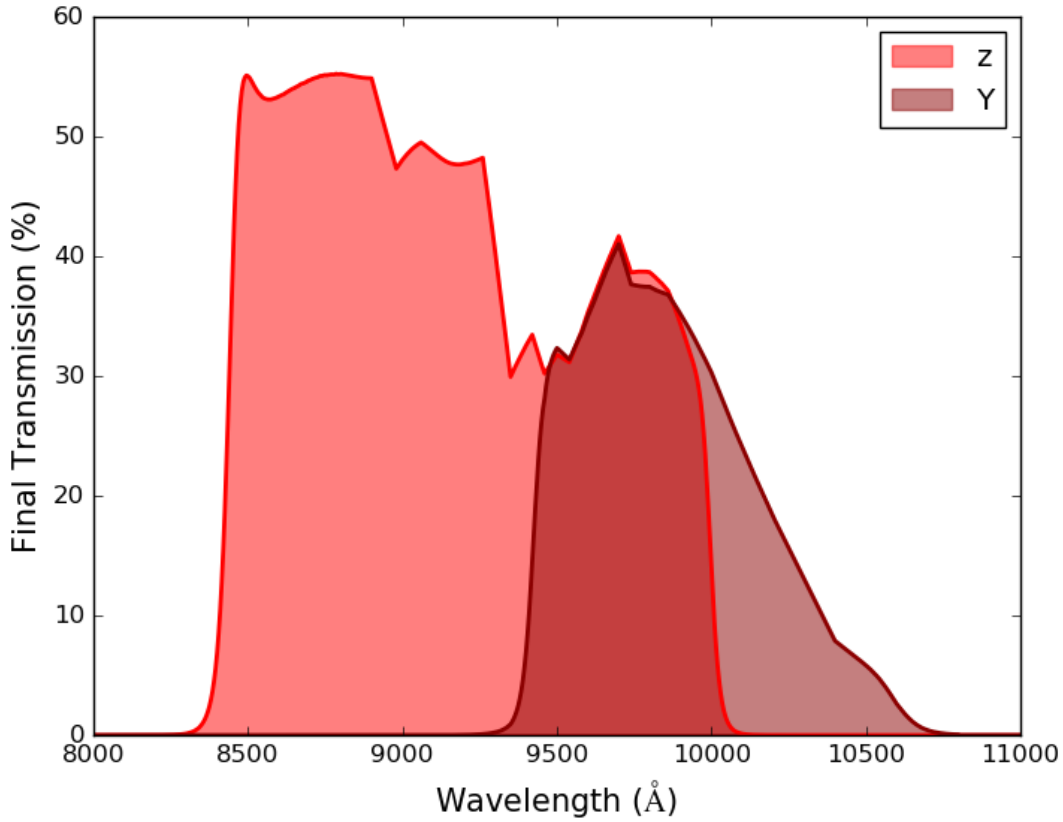

Figure 5.1 The final transmission in the z and Y band for the DES filter set. The considerably overlap between the two filters can be seen this affects how much of a drop out objects appear to be at a given redshift. For a quasar to leave the z band completely it would have to be at a very high redshift (z $\sim$ 7.2).

catalogue. As the Y band DES images are not as important to the primary science drivers of DES they are taken in worse conditions and the final coadded images are not as deep as the other bands. Due to this an error cut of $\sigma_Y < 0.2$ was used rather than 0.1 as was used for the lower redshift selection.

From this clean, flux limited sample point sources were selected using $Y_{psf} - Y_{model} < 0.145$ as described in Section 3.1.2. A colour cut of z - Y > 0.5 was then applied to select red objects that are likely to be quasars above z = 6.5, or their main contaminant cool stars. Figure 5.2 shows the colour cuts used to select candidates and the predicted path of the contaminating cool stars. Many of these cool stars were removed in a later step. As quasars at z > 6.5 are expected to be non detections in the g, r and i bands objects with g_{psf}, r_{psf} or $i_{psf} < 23.0$ were removed. To remove objects which were situated in a particularly deep part of the survey and thus had good detections despite being fainter than 23.0 in g, r or i objects with σ_g, σ_r or $\sigma_i < 0.1$ were also removed. Once this list had been made the brightest objects were visually inspected

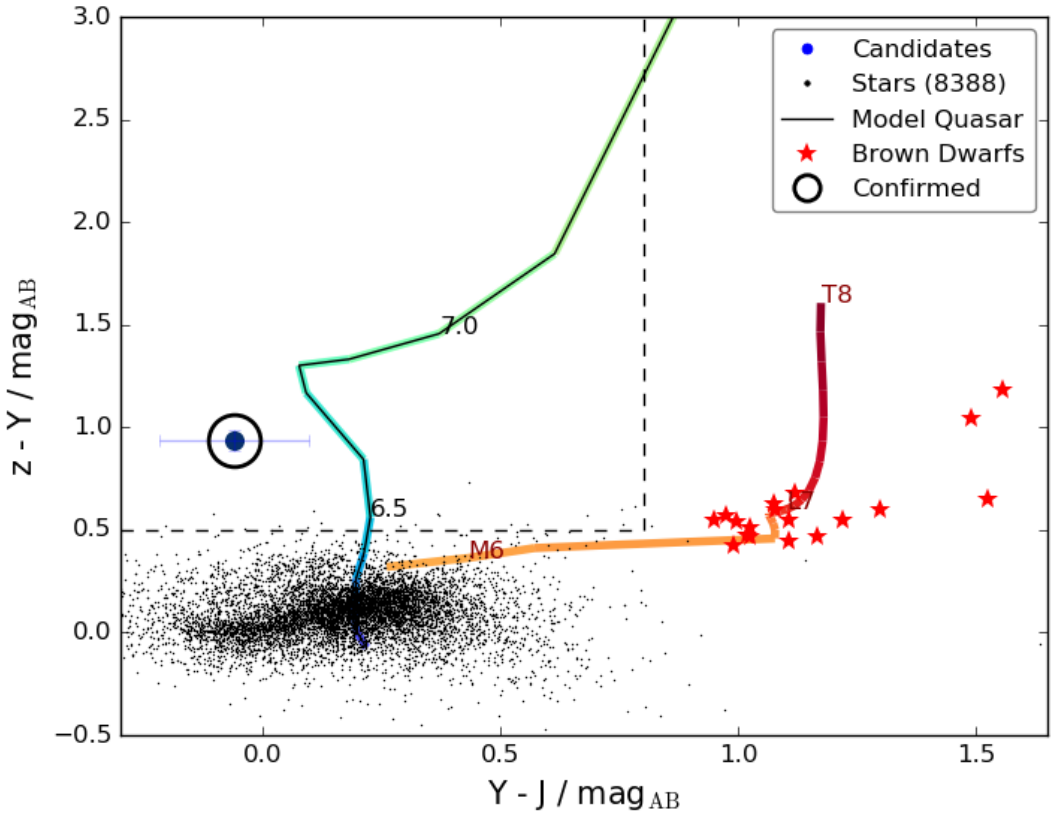

Figure 5.2 A colour - colour diagram showing the predicted tracks of quasars (blue-green line) and cool stars (orange-red line). The red stars are known brown dwarfs taken from (Kirkpatrick et al., 2011), the black points are point sources taken from three tiles of the DES data and the blue circled point is the first confirmed z > 6.5 quasar from DES. The dashed lines show the colour cuts used and it can be seen that they separate the predicted loci of high redshift quasars and cool stars well while being non restrictive.

and it was found that most of them were clear detections in the i band but had errors larger than 0.1. The aim of this initial selection was to find the highest redshift object in the area as a proof of concept for the selection method. Therefore it was decided that only keeping objects with $\sigma_i > 0.2$ (which might remove some z $\sim$ 6.5 objects in particularly deep patches of sky) would be fine for this selection.

After the catalogue based steps were applied the list was visually inspected again and the main contaminants remaining were found to be objects that had obvious, bright detections in the g, r or i band image but were non detections in the catalogue. These were removed in the same way as the bright objects in the g and r band were in Section 3.1.3, by using a rough version of forced photometry. Once this had been done the next largest group of contaminants consisted of image artefacts in the Y

Table 5.1 Summary of the steps in the high-redshift quasar selection process. All magnitudes are in AB.

Step	Description	Number Removed	Number Remaining
	Number of objects in database		139,142,161
1	Flag criteria	6,313,754	132,828,407
2	$Y_{PSF} \leq 21.5$ and $\sigma_Y < 0.2$	98,697,759	34,130,648
3	$Y_{PSF} - Y_{model} < 0.145$	16,773,813	17,356,835
4	z_{PSF} - $Y_{PSF} > 0.5$	16,565,278	791,557
5	g_{PSF}, r_{PSF} and $i_{psf} > 23.0$	739,353	52,204
6	σ_g, σ_r and $\sigma_i > 0.1$	23,474	28,730
7	$\sigma_i > 0.2$	24,829	3,901
8	Forced photometry in r band	1,471	2,430
9	Matched to VHS	1,276	1,154
10	Y_{PSF} - $J_{aper3} < 0.8$	271	883
11	$J_{aper3} < 21$	514	369

band such as cosmic rays and diffraction spikes. A quick way to remove these objects was to only keep objects matched to the VHS database with a good J band detection. Objects without J band matches, that were brighter than our magnitude limit, were likely to be junk that had no corresponding identification in the VHS data. The J band data is also important for removing the cool stars as they have a different Y - J colour to quasars. This colour difference is utilised by only keeping objects with Y_{AB} - J_{AB} < 0.8 which are more likely to be high redshift quasars. The Y - J cut is shown in Figure 5.2 where it can be seen that this cut separates the predicted loci of the quasars and cool stars without incising into the area of colour space quasars are expected to occupy. To ensure that the J band magnitude came from a reliable detection rather than a coincident patch of positive noise a magnitude limit of $J_{aper3,\ AB} < 21.0$ was applied. These steps are summarised and the number of objects removed at each stage given in Table 5.1.

After all of the selection steps 369 candidates were left of which the aim was to select one for spectroscopic follow up. These objects were matched to the *WISE* data to provide additional photometry to help with the prioritisation. Following visual inspection the brightest candidate (VDES J0244-5008) with appropriate *WISE* colours was selected for spectroscopic follow up. *WISE* colours for high redshift quasars are shown in Figure 3.13 and objects situated in the high redshift quasar locus in that Figure were given a higher priority.

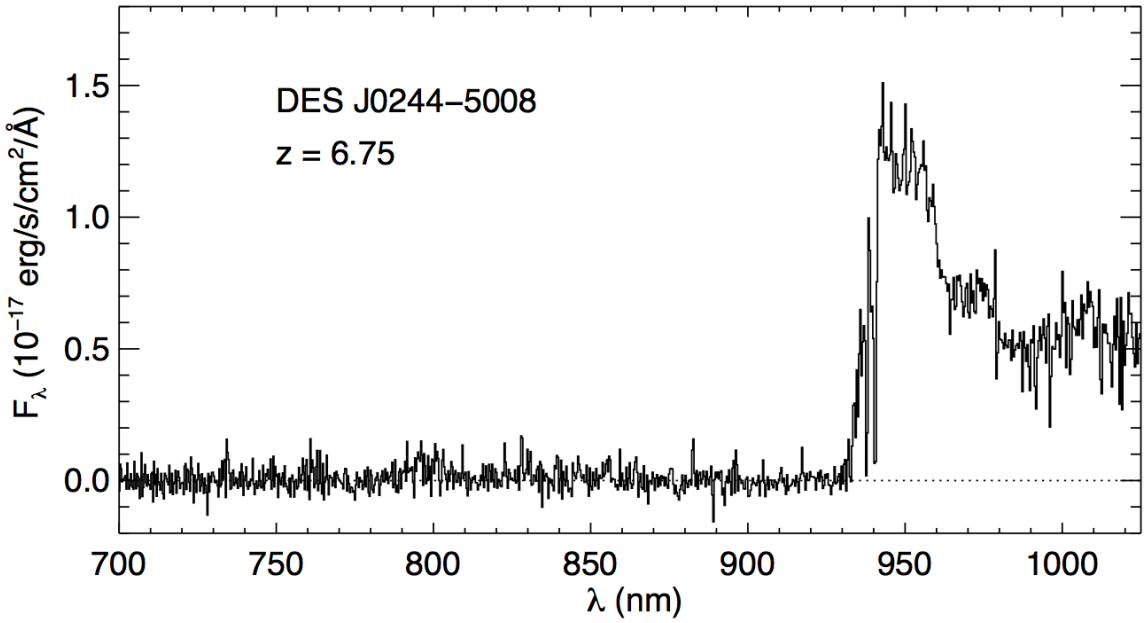

Figure 5.3 The discovery spectrum of VDES J0244-5008 taken by Michael Rauch and reduced by George Becker.

5.1.3 Spectroscopic Confirmation of the First z > 6.5 Quasar from DES

In January 2015 VDES J0244-5008 was observed by Michael Rauch using the Magellan Echellette Spectrograph on the 6.5m Walter Baade Telescope at Las Campanas and was reduced be George Becker. The spectrum shown in Figure 5.3 confirms the identity of the object as a quasar at z = 6.75. A summary of the properties of VDES J0244-5008 are given in Table 5.2 where the lack of detectable flux in the g, r and i bands is shown.

5.2 SED Fitting to Select z > 6.5 Quasars

5.2.1 DES Year 3 Data and VHS Overlap

The VHS data used in this selection covered about 68% of the ∼5000 deg^2 area of the DES Y3 data release, discussed fully in Section 2.2.4. This gave about 3400 deg^2 of area with VHS data. The J band data from VHS is very important for breaking the degeneracy between cool stars and high redshift quasars particularly between 6.6 < z < 6.8 quasars and T dwarf stars. As detailed in Section 5.2.3 two catalogues

Table 5.2 Properties of VDES J0244-5008. The g, r and i band magnitudes are given as a 2σ magnitude limit for a 2" aperture.

	VDES J0244-5008
DES Tilename	DES0245-4957
RA (J2000)	41.00424 ($02^h44^m01.02^s$)
DEC (J2000)	-50.14826 (-50°08'53.7")
Redshift	6.75 ± 0.01
g	> 26.42 [AB]
r	> 25.95 [AB]
i	> 25.18 [AB]
z	21.08 ± 0.08 [AB]
Y	20.15 ± 0.05 [AB]
J	20.21 ± 0.15 [AB]
Ks	19.67 ± 0.14 [AB]
W1	19.72 ± 0.11 [AB]
W2	19.52 ± 0.14 [AB]

were used one which covered only the data matched to VHS and one, with a higher contamination rate, that covered the full area. As the *WISE* forced photometry was driven from the VHS data this was not available for the area not covered by VHS, for this selection the *ALLWISE* catalogue was used to provide additional photometry.

5.2.2 zY Detection Catalogues

The standard DES catalogues are produced using SExtractor in double image mode (as discussed in Section 2.2) using a detection image made from a stack of the r, i and z band images. This is unsuitable for high redshift quasar selection as they are undetected in the r and i bands and dropping out of the z band so are less likely to make it into the catalogue. To rectify this the DES pipeline was rerun on the Y3 images using a detection image made from a combination of the z and Y band images. This is more useful for high redshift quasars but does introduce new artefacts to the catalogue. Due to the achromatic response of the instrument and telescope there are large diffraction features present in the Y band which are not present in the other bands. These are show in Figure 5.4 and cause large numbers of false detections in the catalogue which are propagated into the selection as they look like z - Y drop outs due to only being present in the Y band.

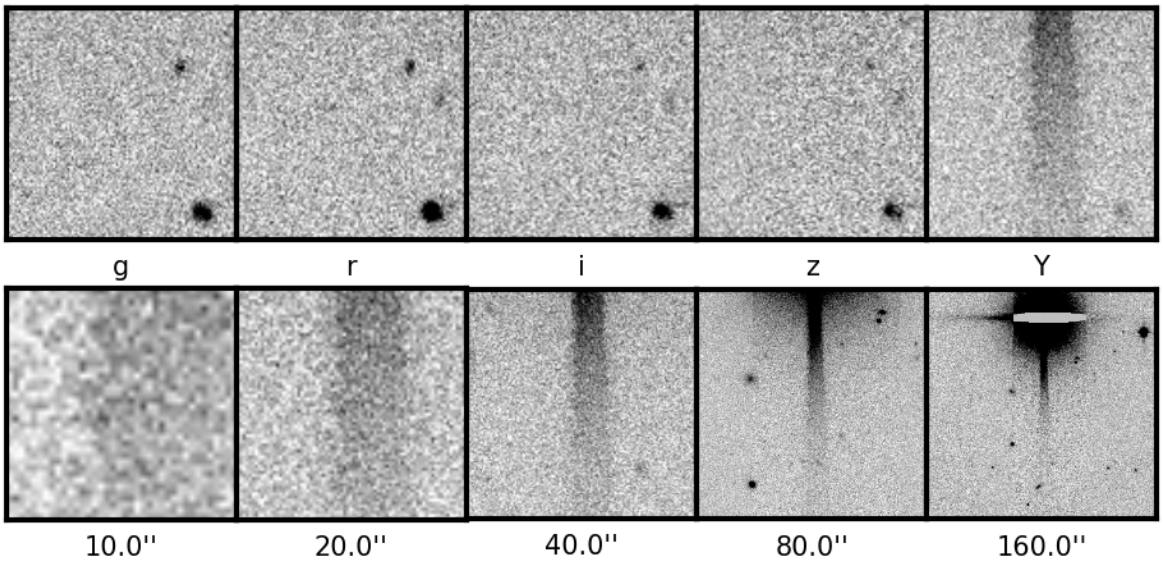

Figure 5.4 The top row of images show 30 arcsecond cutouts of the object in each of the DES bands. It can be seen that there is no clear detection in the other bands but that there is a bright linear feature in the Y band. The bottom row of images gives the same object shown in the Y band at a variety of zoom levels. In the wider images it can be seen that the Y band flux is a diffraction spike originating from a bright object.

5.2.3 SED Fitting Selection

The method discussed in Chapter 4 was extended to redshifts above z = 6.5. The first step was to take all the ∼10,000 DES tiles that were reprocessed and match them to the un*WISE* forced photometry catalogues produced in Section 4.1.1 to get *WISE* and VHS photometry for all the sources. The catalogue based selection cuts given in Section 5.1.2 were then applied to each tile as it was read in, the Y - J cut was not applied at this point and no point source criterion was used.

Once the initial catalogue was made it was split into two different lists. One that was covered by the VHS survey and thus had un*WISE* forced photometry and one that was matched to the standard *ALLWISE* catalogue. Matching to the *ALLWISE* catalogue cut down on the number of artefacts, false detections and moving objects that were in the candidate list by requiring the object to be present in two surveys. For the objects with a VHS detection a colour cut of Y - J < 1.0 was imposed. This was looser than was used previously to allow the selection to probe a wider variety of quasar types while still helping to cut down on the number of cool stars. It was found in Section 4.5 that the objects being selected by the SED fitting method were covering a wider range of properties in colour space than had been allowed by previous selections (for example VDES J2250-5015 is too red in Y - J to satisfy the selection

Table 5.3 Summary of the steps in the z > 6.5 quasar selection process. All magnitudes are in AB. The red highlighting shows the final number in each catalogue.

Step	Description	Number Removed (VHS match) / (All)	Number Remaining (VHS match) / (All)
	Number of objects in database		425,880,019
1	Flag criteria		
	$Y_{PSF} \leq 21.5$ and $\sigma_Y < 0.2$		
	z_{PSF} - $Y_{PSF} > 0.5$		
	g_{PSF} and $r_{PSF} > 23.0$		
	σ_g and $\sigma_r > 0.1$	425,058,310	821,709
2	Match to *WISE* forced photometry or *ALLWISE*	576,543 / 567,616	245,166 / 254,093
3	Y-J < 1.0	361,181 / -	215,362 / -
3	Y < 21.0	- / 217,918	- / 36,175
4	$i_{PSF} > 23.0$ and $\sigma_i > 0.1$	176,678 / 31,290	35,684 / 4,885
5	$z_{predicted} > 6.3$ and $\chi^2_{Quasar} < 25.0$	35,433 / 4,342	251 / 543
6	Chip edges in z and forced photometry in r band	- / 56	- / 487

in some previous studies (Bañados et al. 2016; Venemans et al. 2015a)). To allow for this the Y - J cut used was relaxed from 0.8 used in Section 5.1.2 to Y - J < 1.0 in this selection.

Initially the brightest candidates were focussed on and the non-VHS matched list narrowed down using a magnitude cut of Y < 21.0 since this would give objects more suitable for follow up studies and more easily observed with the NTT which is working at the limit of its wavelength coverage at z = 7.0 and has poor response requiring long integration times at these redshifts. This was not imposed during the selection steps given in Table 5.3 for the objects matching the VHS catalogue but was taken into account when prioritising objects for follow up during the final phase of the selection. At this stage it was found that many of the objects had clear detections in the i band suggesting they were at lower redshift than this selection was aimed at (or that they were not quasars). These were removed by requiring that the object was faint in the i band ($i_{psf} > 23.0$) and that it was not detected at the 10σ level ($\sigma_i > 0.1$). While this may affect the completeness of the sample at the lower end of the redshift range (6.5 < z < 7.2) that we are hoping to probe it is an acceptable sacrifice while the effectiveness of the selection method and the accuracy of the photometric redshifts is studied. Once the accuracy of the photometric redshifts and the efficiency of the χ^2 based selection is fully understood it is hoped to be able to relax the i band cuts and rely on cuts in χ^2 space to narrow down the final candidates, this is discussed in Section 4.6 in the

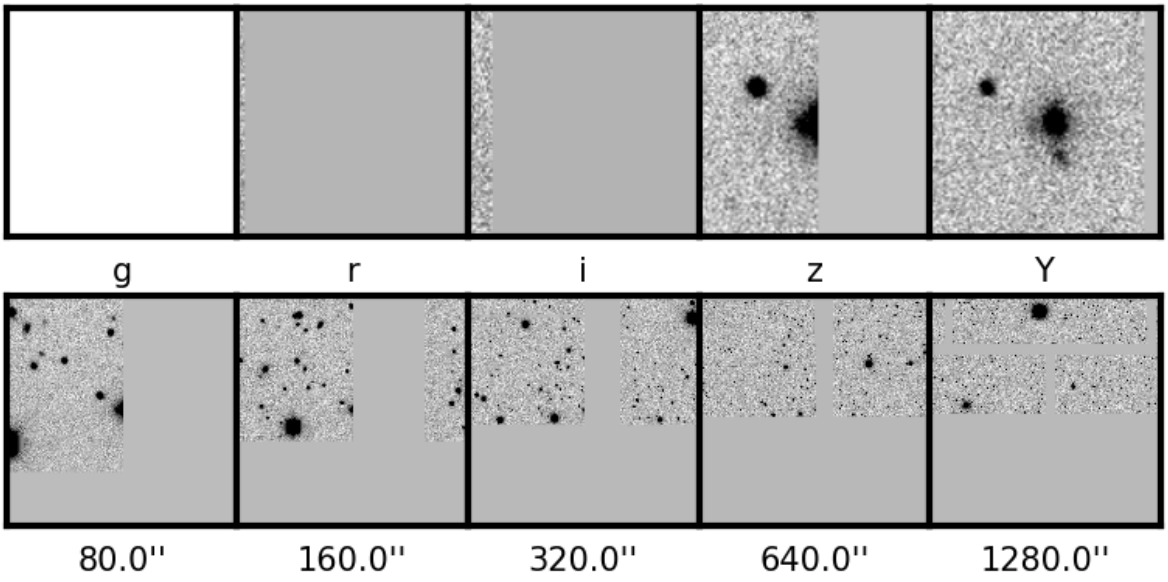

Figure 5.5 The top row of images show 30 arcsecond cutouts of the object in each of the DES bands. The g band has no DES image, the r and i bands have a coadded image covering the area where the object is but it has no data at this position, the z band has half of the object obscured and the Y band looks normal. The bottom row of images gives the same object shown in the z band at a variety of zoom levels. As the image is zoomed out it becomes apparent that the object is situated on one of the chip gaps on the detector and that this coadd stack does not contain enough images to fully cover the chip gaps.

context of the lower redshift search.

To narrow down the two lists to objects most likely to be quasars at high redshift cuts in photometric redshift and χ^2_{Quasar} were used. A photometric redshift of 6.3 was used as the deliminator which gave an allowed uncertainty of 0.2 on the lower bound of the redshift range being covered. An uncertainty of 0.2 is larger than all the differences found between the spectroscopic and photometric redshifts of the objects given in Table 4.2. The differences between the spectroscopic and photometric redshifts calculated for the sample found in Chapter 4 have a maximum value of -0.15 and a median value of -0.09 for $z_{\text{Photometric}}$ - $z_{\text{Spectroscopic}}$. Again a very loose cut in χ^2_{Quasar} was used ($\chi^2_{\text{Quasar}} < 25.0$) as the method was not tested at this redshift range and an increased number of objects for visual inspection was preferred over throwing away potential candidates. There were two known $z \geq 6.5$ redshift quasars in this area; the object found in Section 5.1.2 and a quasar at z = 6.6 (J0305-3150) found in (Venemans et al., 2013). Both of these objects had $\chi^2_{\text{Quasar}} << 25.0$ but due to the small sample size this was not used to heavily influence the value of χ^2_{Quasar} chosen. The quality of the χ^2 fit is dependent on the quality of the photometry that goes into in the fitting. This means that objects that are in patches of dubious imaging

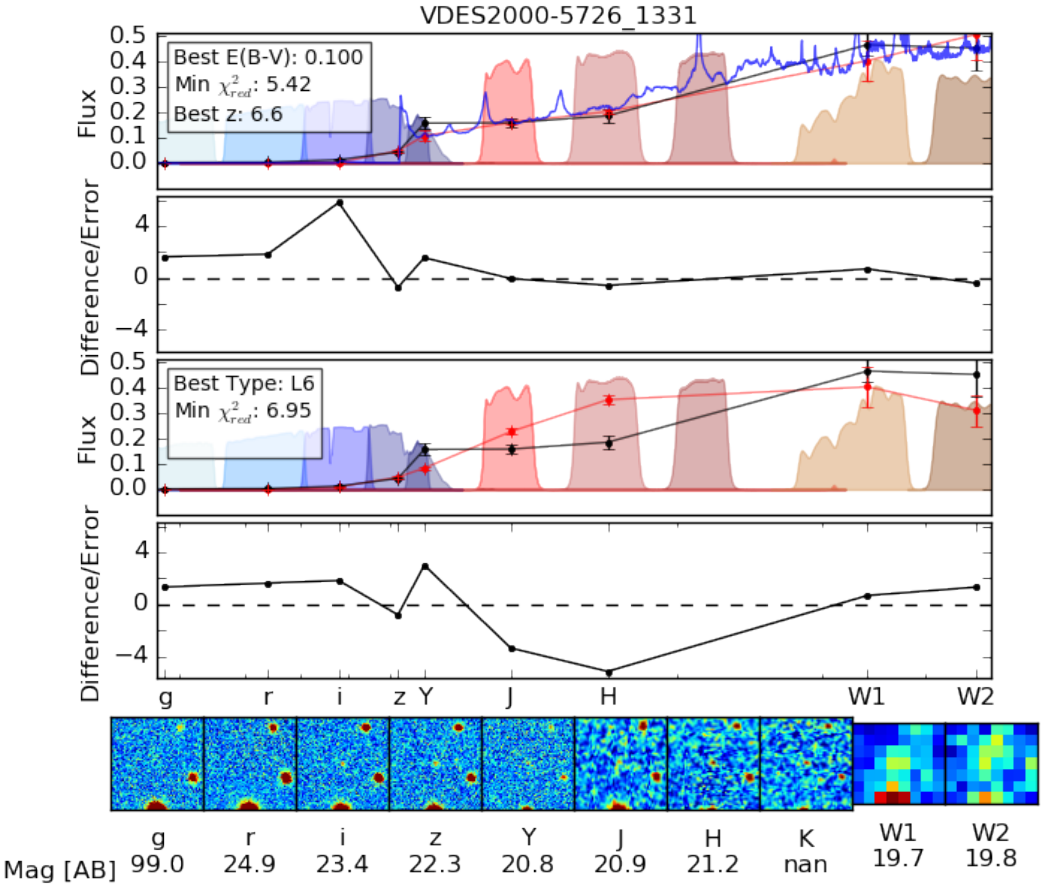

Figure 5.6 The SED fitting plot for VDES J2000-5726 one of the candidates for follow up identified from the Y3 data. The top two panels show the best quasar fit and the residuals for this fit respectively. The next two panels show the same for the best fitting brown dwarf model. The bottom row of images shows 20 arcsecond cutout images across the DES, VHS and *WISE* bands.

can look a lot like quasars due to having no flux measured in the blue bands. When the list matched to *ALLWISE* was visually inspected it was found that objects like this were contaminating the list. The main contaminants were objects that were actually detected in the r band, which were removed using a rough version of forced photometry (discussed fully in Section 3.1.3), objects that were undetected due to poor quality imaging in g/r/i, which were removed as described in Section 4.1.2 and objects that were on the edge of linear areas of zeros in the z band, shown in Figure 5.5. Objects on chip edges were removed by studying the distribution of pixel values in a 30 arcsecond box around the object. Objects where a large number of the pixels had the same value were removed. In the z band image of Figure 5.5 circa half of the pixels have the same value and it was removed at this stage of the processing. After these steps there were two lists for visual inspection, prioritised by χ^2_{Quasar}.

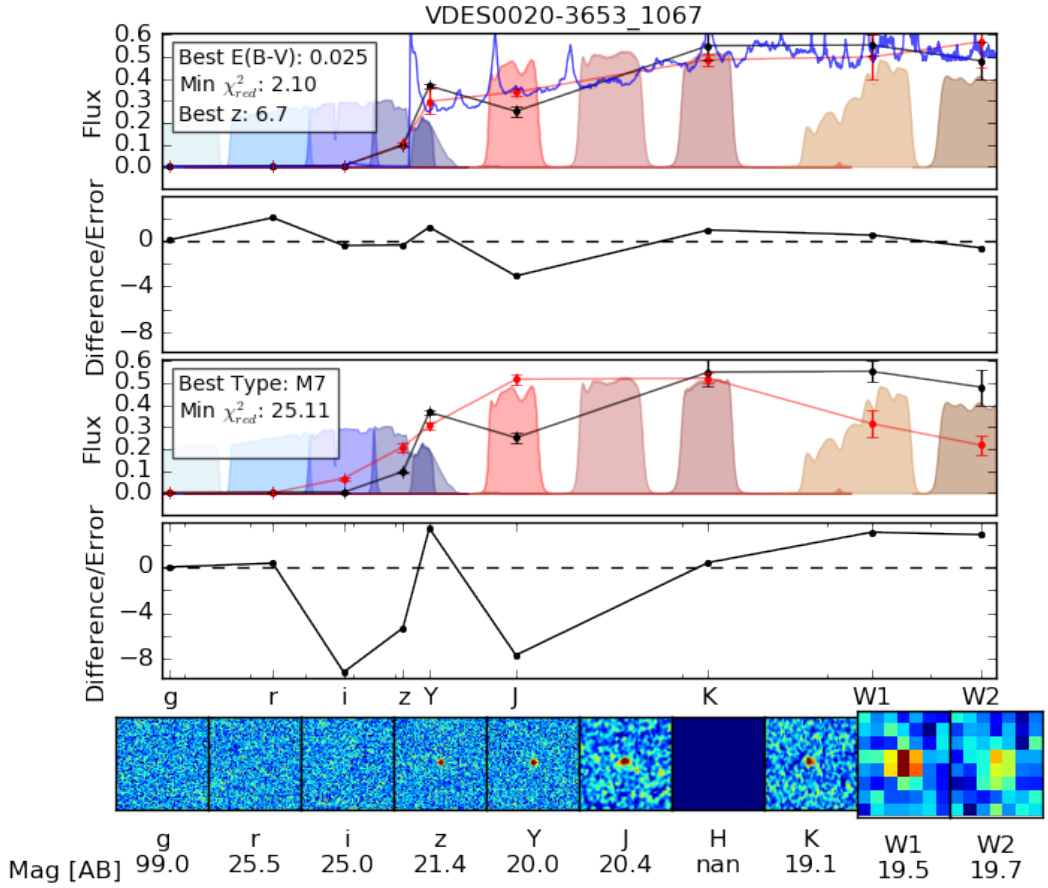

Figure 5.7 The SED fitting plot for VDES J0020-3653 one of the candidates for follow up identified from the Y3 data. The top two panels show the best quasar fit and the residuals for this fit respectively. The next two panels show the same for the best fitting brown dwarf model. The bottom row of images shows 20 arcsecond cutout images across the DES, VHS and *WISE* bands. VDES J0020-3653 was confirmed as a quasar with z = 6.9.

5.3 Spectroscopic Confirmation

From the final lists two candidates were selected as the highest priority candidates for the next observing run. Sadly one of them, shown in Figure 5.6, was unobservable at Christmas 2016 (the time of the last observing run) but will be revisited in future observing time. VDES J2000-5726 has a high χ^2_{Quasar} (5.42) compared to confirmed quasars in the sample and would be an interesting test to see how well the selection method is performing.

On Christmas Eve 2016 the other candidate (VDES J0020-3653, fitting shown in Figure 5.7) was observed using EFOSC2 on the NTT at ESO's La Silla observatory. The data was reduced as summarised in Section 4.2 with a slight variation to the method. At the redshift of this object (z = 6.9) it is very hard to see in the acquisition

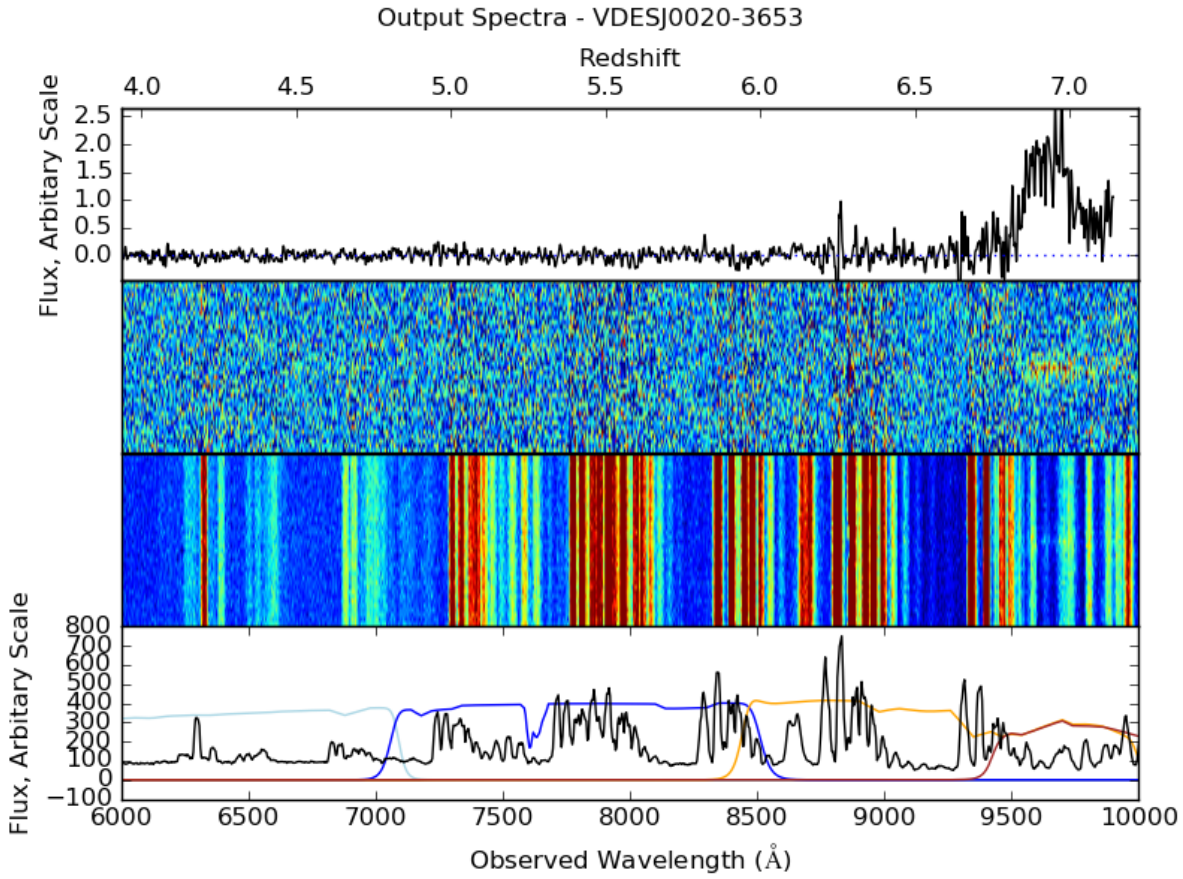

Figure 5.8 The NTT spectrum of VDES J0020-3653, the top panel shows the stacked one dimensional spectrum, the second panel shows one of the two dimensional sky subtracted spectrum, the third panel shows the same 2D spectrum before sky subtraction and the bottom panel shows the error array with the DES filters overplotted. It can be seen that flux from the object covers very little of the wavelength range of the instrument.

images for the NTT even in a long exposure in the z band so acquisition was done using a blind rotation to the target. For this method a nearby bright object was acquired and then the slit was rotated to the angle between the target and the acquired object which meant that the object was in the slit though it could not be seen. This process meant that the object was not central on the detector and it was found that this affected the shape of the trace of the object. Studying objects at different positions on the detector showed differences in the traces of these objects. It was found that this could be accounted for by allowing the gradient of the path of the trace to be changed as well as the offset when calculating the path the trace of the object should take.

Two 1800 second exposures were taken early on Christmas morning in relatively poor seeing conditions (1.2 - 1.6 arcsecond seeing). A 1.5 arcsecond slit was used with grism 16 and blocking filter OG530 to counter reflected light in the set up. The

reduction of these spectra is shown in Figure 5.8 which shows the indicative flux deficit blueward of the inferred Lyα peak of a high redshift quasar at z = 6.9.

5.4 Infra Red Spectroscopy

In order to calculate more accurate redshifts and to give an estimate of the black hole mass an IR spectrum covering the MgII line at 2799Å(restframe) is required. Black hole mass measurements are discussed futher in Section 5.6.3.

5.4.1 Flamingos 2 Data Reduction

IR spectra were taken with Flamingos 2 (F2) on the Gemini South telescope for two of the highest redshift objects discovered, VDES J0224-4711, discovered in Section 4 and VDES J0244-5008, discovered in Section 5.1.2. F2 is a near IR wide field imager and multi-object spectrometer currently installed on Gemini South. For these observations the long slit spectroscopy mode was used with a slit width of 4 pixels. F2 uses a 2048x2048 Hawaii-II (HgCdTe) detector with 18-micron pixels. There are two grisms used in the setup for these observations, the JH and HK grisms. The JH grism covers 0.9 to 1.8 microns and the HK grism covers 1.2 to 2.4 microns. These can then be combined to give coverage from 0.9 to 2.4 microns in the observed frame (0.1 to 0.3 microns in the rest frame).

VDES J0224-4711 was observed on November 8th 2016 and VDES J0244-5008 was observed on January 3rd 2017, all the observations were taken in service mode. Both objects were observed for 200 seconds eight times in both JH and HK. The observations were taken in pairs using an ABBA nodding pattern with a spatial offset between them. These pairs were then reduced together, one observation was subtracted from the other to remove artefacts and as a first pass at sky subtraction. The subtracted image was then flat fielded. This left a relatively clean image with two traces from the object visible, one positive and one negative, shown in Figure 5.9. These two sections were then cutout and reduced separately.

To remove the sky lines left after subtraction the median of the data in the spatial direction was subtracted from the 2D spectrum. The trace of the object was calculated by fitting a Gaussian to each wavelength slice of the data and studying the path their centroids tracked over a section of the data with high signal to noise. It was found that this path was well recovered by a linear fit, this fit could then be used to predict the centroid of the Gaussian in areas of the spectrum with poor system response and low

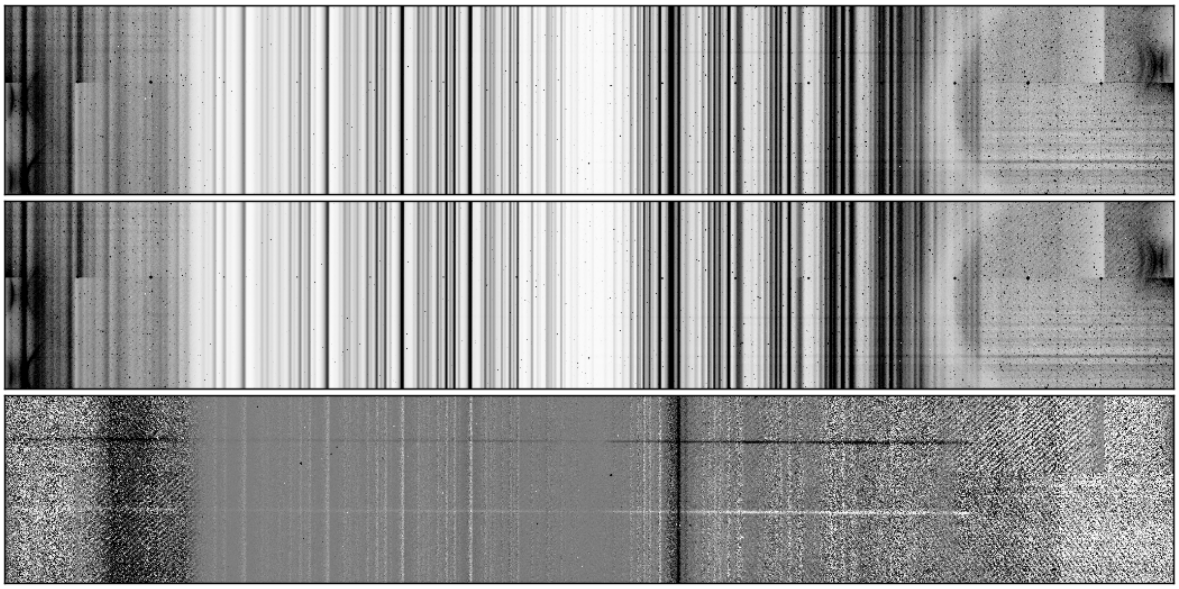

Figure 5.9 The top two panels show a pair of F2 observations of VDES J0244-5008 in the JH filter, these 2D spectra have been flat fielded. In these two 2D spectra lots of sky lines and artefacts can be seen. The bottom panel shows the middle spectrum subtracted from the top spectrum. The positive and negative trace of the object can be seen along with residual sky features. The data is not wavelength calibrated and short wavelengths are on the right of the plot and long wavelengths to the left. The image also shows that the trace of the object is not in the same pixel at every wavelength but moves significantly across the detector.

signal to noise. The predicted trace and the area used for the calculation are shown in Figure 5.10. The spectrum was then extracted along the trace and weighted by a Gaussian centred at the predicted centroid.

Wavelength calibration was done using Argon lines from arc lamp spectra taken during the night of the observations. It was found that the wavelength solution was satisfied by a 5^{th} order Chebyshev polynomial fit. The median was then taken of the eight individual spectra to give the final output spectrum. The system response and its correction was calculated using standard observations of HIP6364, which has a spectral type of A0V, taken just preceding the observations of the target. The standard observations were reduced in the same way as the target data with the only difference being that two pairs of observations were taken rather than four. The output spectrum was then compared to a model for a star of that type (A0V). Dividing one by the other and taking a median filter of the output gave a multiplicative response correction that could be applied to the final spectrum. This process was then repeated for the eight observations taken in the HK filter. The two spectra from the different filters were then combined together to give the final output spectrum.

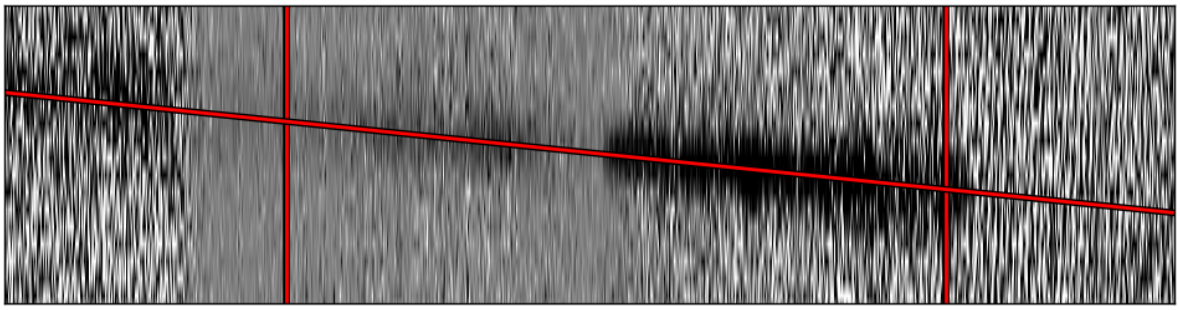

Figure 5.10 A slice of one of the 2D spectra zoomed in on the area around the object. The vertical red lines deliminate the area chosen to calculate the trace from and the diagonal red line shows the predicted path of the trace calculated from the fit.

5.5 Redshift Determination

The redshift determination method described in Section 4.3 was applied to the F2 IR data taken for VDES J0244-5008 and VDES J0224-4711. This method fits a model to the entire spectrum. The model consists of an exponential decay to cover the wavelengths blueward of the predicted Lyα emission line joined to half a Gaussian to cover the red side of the Lyα line. The rest of the spectrum was modelled by Gaussians for each line added to a power law to model the continuum. For the IR data more lines were included to cover the full wavelength range of the data. The CIV line was omitted from the fitting as it seemed to show significant blueshift compared to the other lines (eg. Coatman et al. (2016)).

A simple two Gaussian fit was also done to each of the lines individually. To do this the spectra were normalised by fitting a power law to the continuum flux and dividing through by it. Once this had been done each line was fitted with a line model made up of two Gaussians to give a value of the redshift from that line. These values and those from fitting the full spectrum are given in Table 5.4. The fits to each line are shown in Figures 5.11 and 5.12.

5.6 Analysis of Emission Lines

5.6.1 Spectral Reconstruction

The reduced IR spectra were analysed with Paul Hewett's independent component analysis (ICA) code to give a high signal to noise reconstruction of the spectrum. The individual components used in the fitting are derived from analysis of a large sample

Table 5.4 Redshifts for each of the quasars with IR spectrum calculated from each individual line and from the optical spectra.

	Restframe Wavelength (Å)	VDES J0244-5008	VDES J0224-4711
Optical Spectrum Fit		6.75 ± 0.01	6.50 ± 0.01
IR Spectrum Fit		6.72 ± 0.01	6.52 ± 0.01
SiIV+OIV]	1399.8	6.665 ± 0.009	6.487 ± 0.005
CIV	1549.48	6.6631 ± 0.004	6.477 ± 0.004
CIII]	1908.734	6.699 ± 0.010	6.492 ± 0.010
MgII	2799.117	6.726 ± 0.005	6.526 ± 0.003

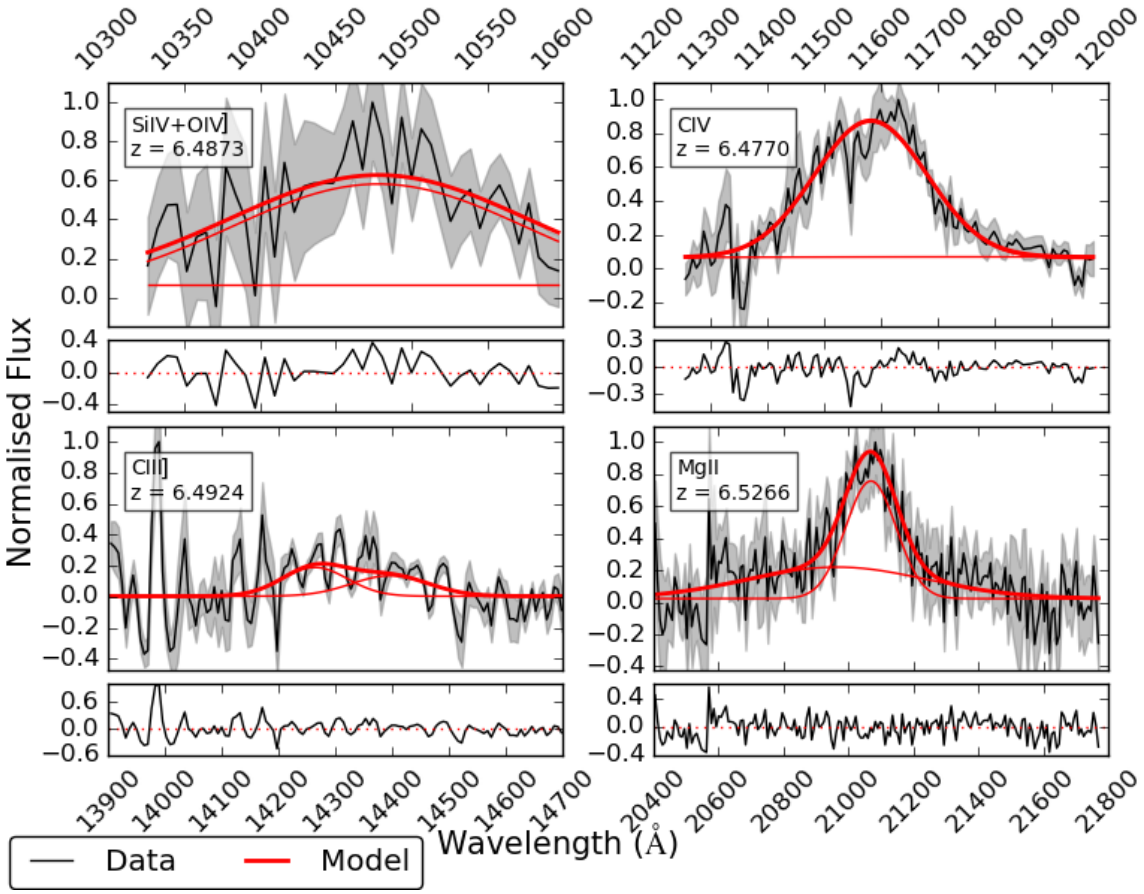

Figure 5.11 Results from fitting two Gaussian components to four of the lines in the spectrum of the z = 6.5 quasar VDES J0244-4711. The small panel under each fit shows the residuals from the fitting. The blueshift of the CIV line compared to the systemic redshift given by MgII can be seen. The thick red line shows the final model and the two thin red lines show the Gaussian components. There was also a constant offset in the y direction included. The grey shaded error shows the spectrum ± the error array. The lines used in this fitting were SiIV+OIV] at 1399.8Å, CIV at 1549.48Å, CIII] at 1908.734Åand MgII at 2799.117

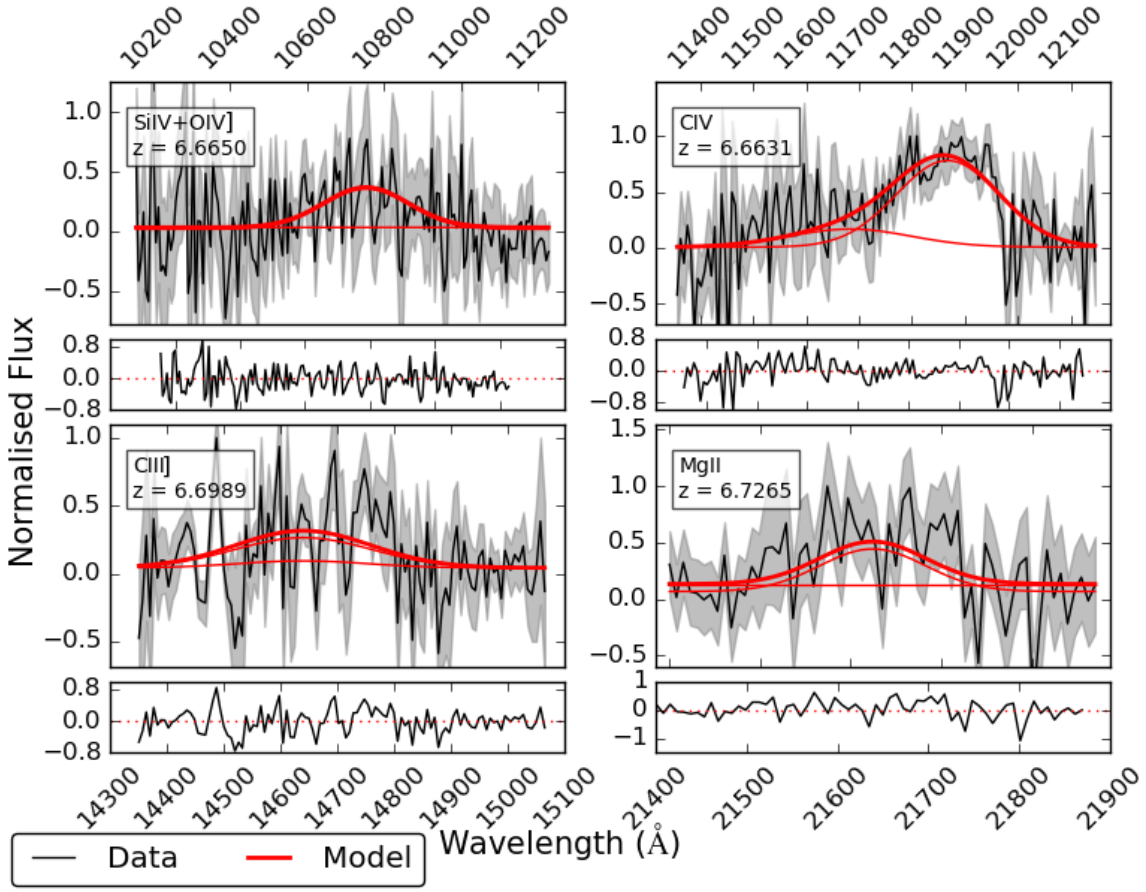

Figure 5.12 The line fits for the z = 6.7 quasar VDES J0244-5008, the plot details are the same as those for Figure 5.11. An even larger offset between MgII and CIV can be seen in this object.

of low redshift (z $\sim$ 2.5) quasar spectra from SDSS. These components can give a more detailed, physically motivated, reconstruction than using a model constructed from component functions, for example a power law continuum with Gaussians added to model the lines. The reconstruction is done by shifting the quasar spectrum into the restframe and then masking out the very low signal to noise sections and absorption systems. After this the resulting spectrum is shape-morphed so that it looks like the typical z $\sim$ 2.5 quasar that the components were derived from. The reconstructed spectra are shown in Figure 5.13 as the red line shown superposed on the black spectrum it was derived from. It can be seen that red line is a good representation of the spectrum.

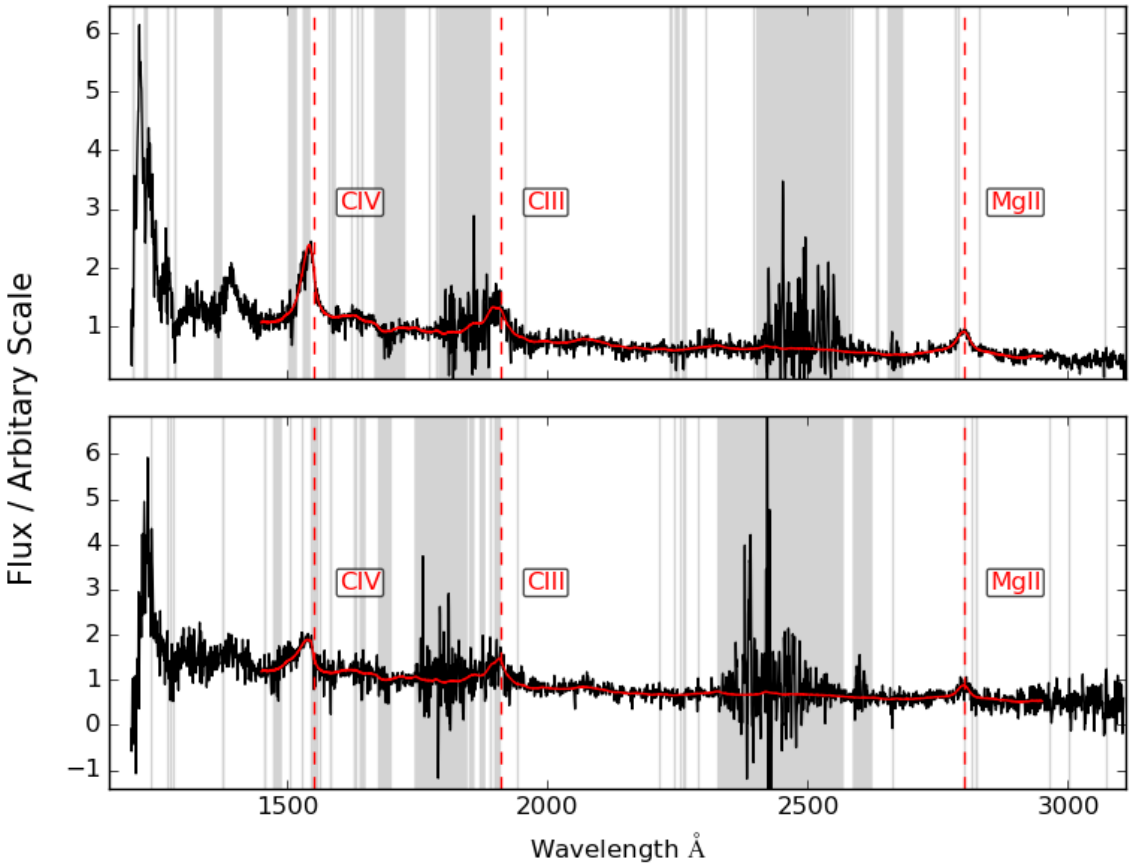

Figure 5.13 The ICA reconstruction (red line) of the spectra overplotted on the shape-morphed spectra (black line). The areas masked out of the reconstruction process are shown with grey shading. The spectra have been shifted into the rest frame. The top panel is the z = 6.5 quasar and the bottom one shows the z = 6.7 object.

5.6.2 CIV Blueshifts

The properties of the CIV line in quasars have long been shown to appear very different from quasar to quasar, with strong blueshifts seen in a significant proportion of the population. Recent studies, such as Coatman et al. (2016), have looked into the relationship between the CIV blueshift and various quasar properties such as FWHM and Eddington ratio. Following the prescription given in Coatman et al. (2016) the blueshift for the CIV line in each of the quasars that have IR spectrum has been calculated. The Coatman et al. (2016) method identifies the location of the CIV line by taking the wavelength that bisects the cumulative total line flux. The location of the CIV line, and thus the blueshift, was calculated for the simple model fit performed in Section 5.5 and for the reconstruction. The blueshifts for each of the lines are recorded in Table 5.5. VDES J0244-5008 (at z = 6.7) in particular has a very large blueshift between the systemic redshift measured from the MgII line and the wavelength that bisects the

Table 5.5 Blueshifts between the systemic redshift calculated from the MgII line fit and the CIV line for .

	VDES J0244-5008	VDES J0224-4711
MgII Redshift	6.726 $\pm$ 0.005	6.526 $\pm$ 0.003
CIV (Line Fit)	3100 $\pm$ 200 kms^{-1}	1800 $\pm$ 200 kms^{-1}
CIV (Reconstruction)	3500 $\pm$ 200 kms^{-1}	1700 $\pm$ 100 kms^{-1}

cumulative total line flux. The blueshift calculated for the 6.7 quasar ($\sim$3000 kms^{-1}) is larger than those found for other z > 6.5 quasars ($\sim$1000-2000 kms^{-1}) in De Rosa et al. (2014) which are consistent with the blueshift measured for the z = 6.5 quasar.

The origin of the blueshift seen in the CIV line is not fully understood but there is an agreement that it is not tracing virial motions of the ionised gas. One theory is that it is caused by outflows driven by disk winds driven by radiation pressure from the UV emission of the quasar (e.g. Gallagher et al. 2015; Higginbottom & Proga 2015). The large blueshift seen in VDES J0244-5008 would be indicative of a strong wind and fast outflow. Another theory is that the blueshifts are caused by the orientation of the accretion disk (Richards et al., 2002b). Here the largest CIV blueshifts would be from quasars seen edge on where the corresponding redshifted component is obscured.

5.6.3 Black Hole Mass Estimates

The measurement of black hole masses places strong constraints on theories of black hole formation and evolution. Theoretical models struggle to grow black holes to the sizes observed ($\sim 10^9$ $M_\odot$) within the brief time available so close to the formation of the Universe (Volonteri & Rees, 2006). Measuring the black hole mass of high redshift quasars can place inference on black hole formation models. Whether the black holes formed from population three stars and then grew rapidly at super-Eddington rates, or if they formed through direct collapse and then grew more slowly can be inferred from the black hole mass and the accretion rates (Trakhtenbrot et al., 2017). Measuring the black hole mass also allows it to be related to the other properties of the quasar. Understanding these relationships at high redshifts gives insight into when the observed low redshift relationships developed. In this Section black hole masses are calculated for all the quasars for which IR spectra covering the MgII line (at λ_{rest} = 2799.117Å) have been obtained.

Black hole masses were calculated from the MgII line following the prescription in

De Rosa et al. (2011) which used the relation obtained by McLure & Dunlop (2004) from a sample of bright low redshift AGN. De Rosa et al. (2011) also defined the bolometric luminosity (L_{Bol}) and the Eddington luminosity (L_{Edd}) as given below.

$$\frac{M_{BH}}{M_{\odot}} = 3.2 \left(\frac{\lambda L_{\lambda}(3000)}{10^{37} W} \right)^{0.62} \left(\frac{FWHM(MgII)}{kms^{-1}} \right)^{2}$$

$$L_{Bol} = 5.15 \lambda L_{\lambda}(3000)$$

$$L_{Edd} = 1.3x10^{38} \left(\frac{M_{BH}}{M_{\odot}} \right) ergs^{-1}$$

The F_{λ}(3000Å) was derived by fitting a power law to the spectrum with the emission lines masked out and computing the flux at 3000. The method to calculate M_{BH} was applied to both the two Gaussian line model derived for the MgII line and the reconstruction of the MgII line computed by Paul Hewett (Hewett, Private Communication). Once calculated the L_{bol} and the L_{Edd} can be used to calculate the Eddington ratio (L_{bol}/L_{Edd}). The L_{Edd} gives the theoretical upper limit that the luminosity can achieve before the resultant radiation pressure drives the material away from the black hole rather than the gravitational force pulling it in. The Eddington ratio indicates how luminous the quasar is with respect to the L_{Edd}, $L_{bol}/L_{Edd} > 1$ indicates that the quasar is brighter than this theoretical limit suggesting that it is very rapidly accreting. Both quasars have M_{BH}, L_{Edd} and L_{bol}/L_{Edd} in the normal range for bright high redshift quasars as shown in Figure 5.14.

To calculate the error on the black hole measurements the line model and the reconstruction were perturbed by random samples from the error array. Measurements of the FWHM were then taken from these realisations of the model and the reconstruction to give a distribution of FWHMs from which the errors could be calculated.

Figure 5.14 plots the distribution of the Eddington ratio versus the M_{BH} for the two quasars analysed in this Chapter along with known z > 6 quasars from the literature. The two different methods of modelling the MgII line give different results for the M_{BH} and the Eddington Ratio. For the z = 6.7 quasar (VDES J0244-5008) these results agree well within the 1σ errors, which are large due to the poor signal to noise of the spectrum covering the MgII line and at 3000Å. The lower redshift object shows a 3σ difference in the calculated Eddington ratio. This difference is driven by the large

Table 5.6 Black hole mass estimates calculated from the two Gaussian model and the ICA reconstruction of the MgII line.

	VDES J0244-5008	VDES J0224-4711
MgII Redshift	6.726 ± 0.005	6.526 ± 0.003
FWHM (Line Fit)	2400 ± 200 kms^{-1}	3100 ± 200 kms^{-1}
FWHM (Reconstruction)	3000 ± 200 kms^{-1}	4100 ± 400 kms^{-1}
$\lambda L_{\lambda}(3000)$	300 ± 200 W	600 ± 200 W
M_{BH} (Line Fit)	0.6 ± 0.3 x 10^9 $M_{\odot}$	1.7 ± 0.4 x 10^9 $M_{\odot}$
M_{BH} (Reconstruction)	0.9 ± 0.5 x 10^9 $M_{\odot}$	2.9 ± 0.7 x 10^9 $M_{\odot}$
L_{Edd} (Line Fit)	0.8 ± 0.4 x 10^{47} erg s^{-1}	2.2 ± 0.5 x 10^{47} erg s^{-1}
L_{Edd} (Reconstruction)	1.2 ± 0.7 x 10^{47} erg s^{-1}	3.8 ± 0.9 x 10^{47} erg s^{-1}
L_{bol}	1.5 ± 1.0 x 10^{47} erg s^{-1}	3.3 ± 1.1 x 10^{47} erg s^{-1}
L_{bol}/L_{Edd} (Line Fit)	1.9 ± 0.6	1.5 ± 0.2
L_{bol}/L_{Edd} (Reconstruction)	1.3 ± 0.4	0.9 ± 0.2

(1000 kms^{-1}) difference in FWHM for the different models of the line.

The two different fits to the MgII line are shown in Figure 5.15 for the z = 6.5 quasar (VDES J0224-4711). In this Figure it can be easily seen that the two models differ in their treatment of the wings of the line. This difference means that the two models give very different measurements of the FWHM which in turn leads to different values for the properties derived from the MgII line. The vertical dashed lines show the extent of the FWHM for each model line profile, it can be seen that the dark red lines delimit a larger FWHM than the red lines.

5.7 Discussion and Conclusions

The method detailed in this Chapter has proved to be successful for finding quasars with z > 6.5 leading to the discovery of two new z > 6.5 quasars to add to the one found

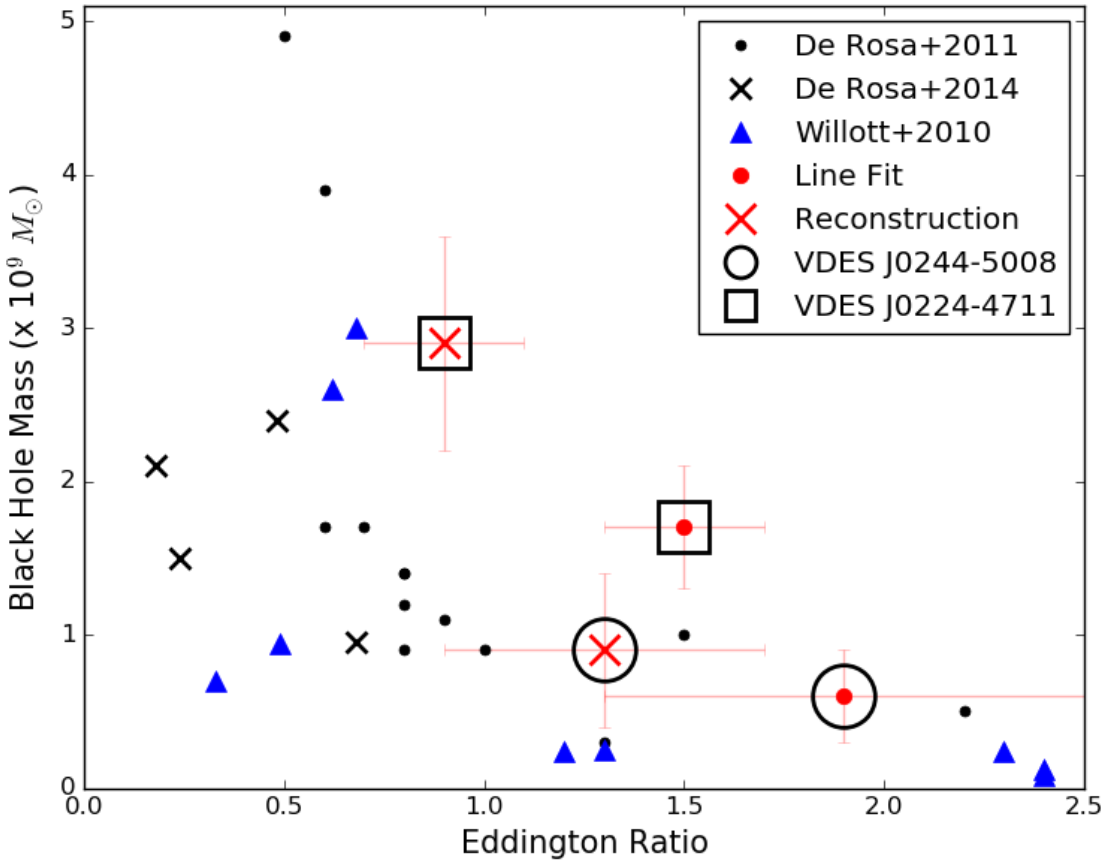

Figure 5.14 Eddington Ratio against M_{BH} for these two objects and for samples from the literature.

in Chapter 4. This method originated in a simple series of colour cuts and was then expanded into a SED fitting selection that covered the full parameter space provided by the complementary multi wavelength surveys. This provides a fast, reproducible selection with low contamination rates. This selection discovered two new z > 6.5 quasars and rediscovered one previously known object from Venemans et al. (2013) J0305-3150. These new objects are shown in Figure 5.16 (along with the z = 6.5 quasar that was discovered in Chapter 4), it can be seen that these quasars are brighter than most previously known objects at z > 6.5. The discovery of these bright quasars, with a 100% success rate, shows that this method is particularly suited to finding these rare bright sources that are needed for follow up studies. The success of the selection shows that the method developed initially for lower redshift selection can be easily applied at higher redshift. This success means that this method can be used to find even higher redshift objects when there is more area available to search. This is currently under investigation using a combination of the DES, Pan-STARRS and VHS to give ∼10,000 deg^2 of sky to search.

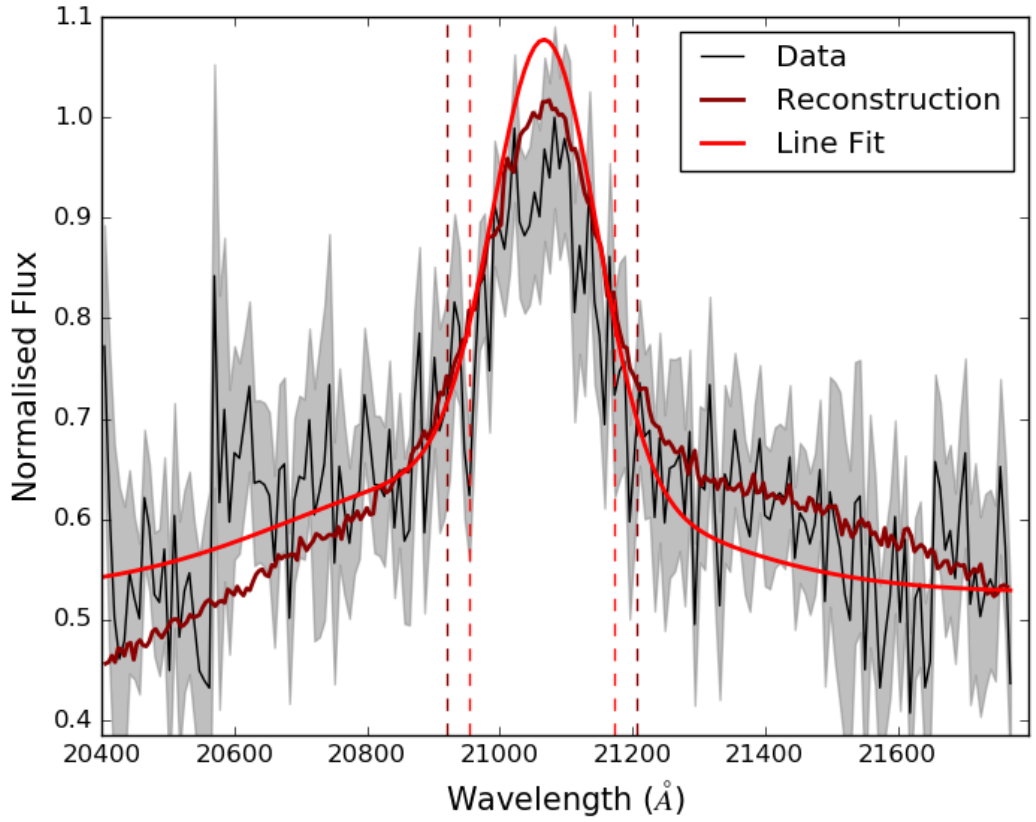

Figure 5.15 The reconstruction and the model line fit for the z = 6.5 quasar (VDES J0224-4711). The black line shows the data with the error given as the grey shaded area. The dark red line is the ICA reconstruction done by Paul Hewett and the red line is the line model constructed from two Gaussians. It can be seen that the models differ significantly in the wings of the line. The vertical dashed lines show the FWHM for each of the fitted line profiles.

From the IR spectra the black hole masses were calculated and the emission line properties studied. This showed a very large blueshift for the CIV line in the quasar at z = 6.72 of $\sim$3500 kms^{-1} which may be indicative of strong disk winds.

The M_{BH}, L_{Edd} and the Eddington ratio were calculated from a two component Gaussian model and an ICA reconstruction. For the z = 6.5 quasar (VDES J0224-4711) the Eddington ratio calculated from the two different models gave different results that did not agree within one sigma. This difference was driven by the large difference in FWHM calculated for each profile and shows that the measurements derived from the MgII line are very dependent on the fitting prescription which they are calculated from.

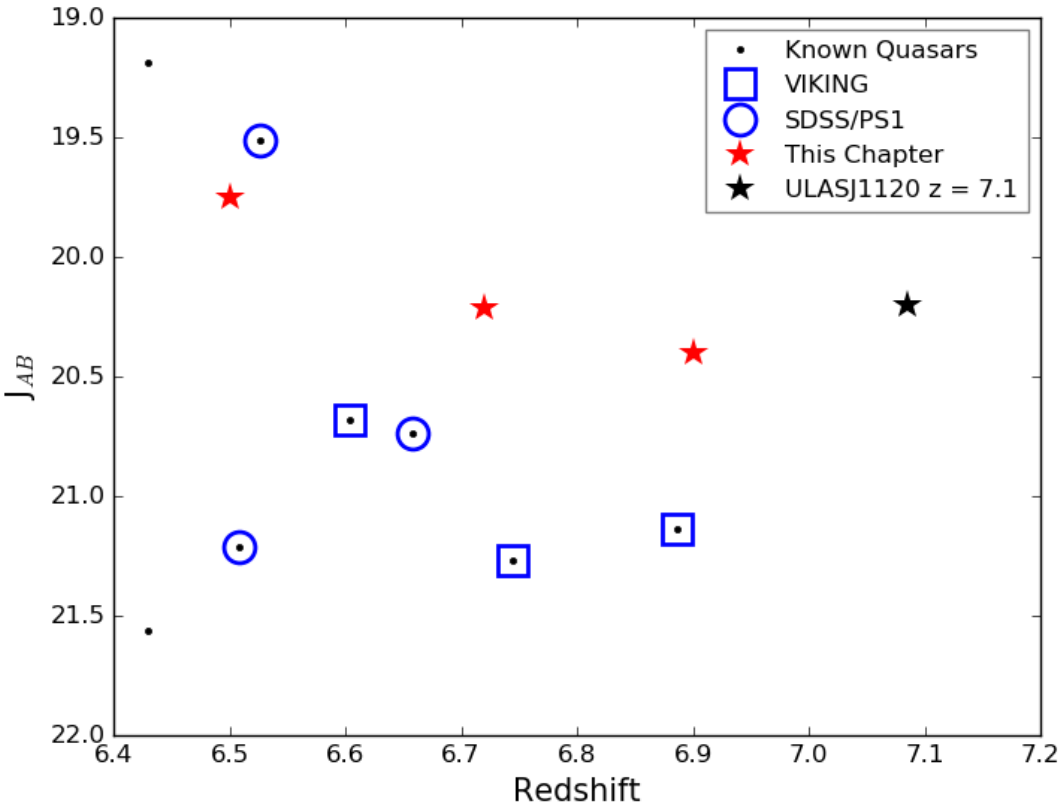

Figure 5.16 Redshift versus J_{AB} for known quasars above z = 6.4 and the quasars discussed in this Chapter. It can be seen that the quasars found in this Thesis (red stars) are brighter than most of the previously known objects. This makes them particularly suitable for follow up studies.

6

High Redshift Quasar Near Zone Size Measurements

One of the main observational constraints on the epoch of reionisation are the spectra of high redshift quasars. The spectra contain tracers of the timing of reionisation and the space density of reionising sources. The Lyα forest, OI forest and the near zone size for these objects are all sensitive to their environment. This Chapter discusses the development of a new way of measuring HII near zone sizes and their uses as a probe of the epoch of reionisation. Understanding the timing of reionisastion is important to cosmic structure formation as it is indicative of the formation epoch of the first luminous objects such as star forming galaxies.

Close to the quasar the UV radiation emitted by the quasar ionises the surrounding medium and creates a bubble of HII. This highly ionised bubble is known as the quasar near zone and its size is determined by the neutral fraction of the surrounding HI gas, the luminosity of the quasar and the age of the expanding radiation front emitted from the quasar. Observations of the near zone sizes and their evolution with redshift have the potential to act as important probes of the Universe in the epoch of reionisation with the caveat that the near zone size is not solely dependent on the neutral fraction and is sensitive to the inhomogeneity of reionisation. On a more positive note with a large enough sample one could determine the clumping scale of HI and the neutral fraction since the clumps can be detected via absorption line spectroscopy.

With the advent of large area surveys > 100 z $\sim$ 6 quasars have been discovered and upcoming surveys, such as LSST, promise to discover many more. The number of high redshift quasars discovered is going to become large enough to make detailed long-exposure follow up spectroscopy unfeasible. So far near zone measurements have been carried out on these longer exposure spectra. Developing a method that can be robustly used on the, often low quality, optical discovery spectra first taken of each object would make statistically sized studies of NZ sizes feasible.

Table 6.1 The spectroscopic data of quasars discovered in this Thesis used in this Chapter.

Object Name	Telescope	Instrument	Date Taken	Exposure Time
VDES J0020-3653	NTT	EFOSC2	25/12/2016	1800 + 1800 = 3600s
VDES J0109-5423	NTT	EFOSC2	24/12/2016	900s
VDES J0159-3633	NTT	EFOSC2	08/10/2015	900 + 900 = 1800s
VDES J0131-3841	NTT	EFOSC2	24/12/2016	900s
VDES J0143-5545	NTT	EFOSC2	10/10/2015	1200 + 1200 = 2400s
VDES J0122-4609	NTT	EFOSC2	23/12/2016	1200s
VDES J0224-4711	NTT	EFOSC2	08/10/2015	1800 + 1800 = 3600s
VDES J0224-4711	Gemini-S	GMOS	22/11/2015	300 x 4 = 1200s
VDES J0244-5008	Magellan	MagE	18/01/2015	1200s
VDES J0323-4701	Gemini-S	GMOS	22/11/2015	600 x 4 = 2400s
VDES J0330-4025	Gemini-S	GMOS	22/11/2015	600 x 4 = 2400s
VDES J0408-5632	NTT	EFOSC2	09/10/2015	1200 + 1200 = 2400s
VDES J0410-4414	Gemini-S	GMOS	05/09/2015	600 x 4 = 2400s
VDES J0420-4453	Gemini-S	GMOS	04/09/2015	600 x 4 = 2400s
VDES J0433-5153	NTT	EFOSC2	24/12/2016	1800s
VDES J0454-4448	Magellan	MagE	02/12/2013	600s
VDES J0532-4401	NTT	EFOSC2	25/12/2016	1200 + 1200 = 2400s
VDES J2250-5015	NTT	EFOSC2	08/10/2015	1800 + 1800 = 3600s

6.1 Observational Data

The quasars discovered over the course of the work detailed in this Thesis are given in Table 6.1. These were used as the basis for a project on near zone sizes. The spectra come from a variety of instruments and have varying resolution and signal to noise. A second optical spectrum of the z = 6.5 quasar (VDES J0224-4711) was taken using GMOS on Gemini-S as the original spectrum was taken in poor observing conditions ($\sim$2 arcsecond seeing).

VDES J0159-3633 was initially discovered by Carnall et al. (2015) but was rediscovered during this work and a spectrum taken of it as part of our follow up observations. Observations taken as part of Venemans et al. (2015b), Venemans et al. (2013) and Mortlock et al. (2011) where also used in this work. These increased the number of objects above z > 6.5 in the sample by including those discovered in Pan-STARRS, VIKING and UKIDSS. There are 17 objects from DES, 2 from PS, 3 from VIKING and 1 for UKIDSS used in this study, giving 23 overall with 9 at $z \geq 6.5$.

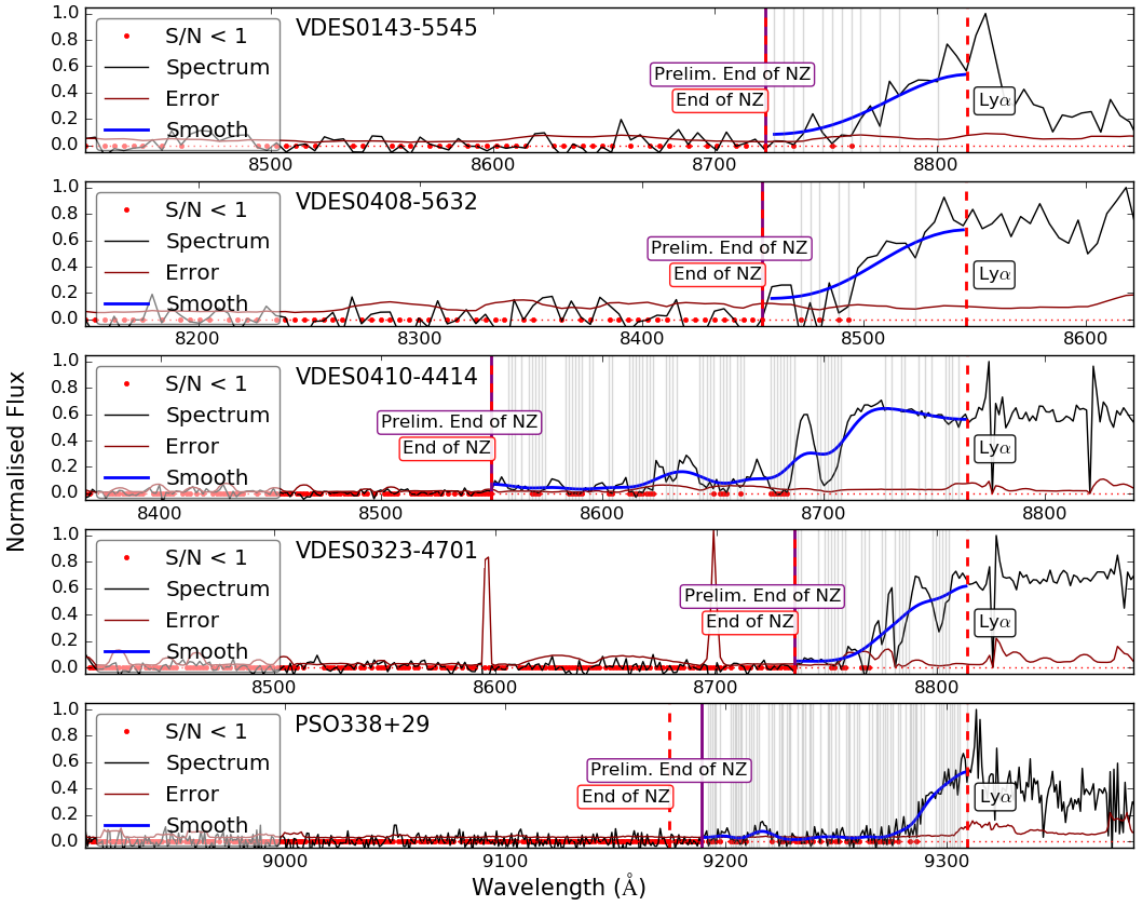

Figure 6.1 The near zone calculation shown for five of the objects in the sample. The black line is the spectrum of each object and the red dashed vertical line labelled Lyα gives the position of the Lyα peak at the calculated redshift. The dark red line gives the error in the flux. Along the 0 flux line the red points mark the areas of the spectra that have signal to noise < 1. The blue lines show the Gaussian smooth and the grey vertical lines mark the areas defined as absorption by being less than the smooth of the data. The purple vertical line (often in the same position as a vertical dashed red line) gives the preliminary end of the near zone that is refined as detailed in Section 6.2 to give the dashed red line labelled end of NZ. It can be seen that in the third panel the method has given a very extended near zone.

6.2 Near Zone Measurement Method

Near zone (NZ) measurements have been calculated in the past using the method outlined in Fan et al. (2006b). This method takes the edge of the NZ to be the point (moving blueward from Lyα) where the ratio of the extrapolated continuum flux and the spectrum first falls below 0.1 when the spectrum has been rebinned to 15Å bins. This method is dependent on having a good measurement of a continuum flux which

at z > 6 can be challenging since the observational wavelength range longward of Lyα in the rest frame is restricted. For example one micron, at which points most optical CCDs finish, corresponds to 1333Å at z = 6.5 and 1250Å at z = 7 and is dominated by the NV emission line at 1240Å. Previously in this Thesis the continuum flux had been approximated by fitting a template to the optical spectra and extrapolating from the template. This could introduce new errors and systematics to the measurement. To avoid doing this I have developed a new method that neither smooths the data excessively nor requires a continuum fit.

Working blueward from the position of the Lyα emission line at the measured redshift of the object the first point at which the signal to noise of the spectrum was < 1 for 10 pixels, with an allowed one pixel gap between pixels that satisfied the criteria, was taken as the initial estimate of the end of the near zone. The spectrum within this area was then smoothed with a Gaussian filter and the maximum size of the absorption features, defined as areas that fell below the smoothed spectrum, was used to define the number of pixels needed to signify the end of the near zone. For example if the maximum sized absorption feature was 15 pixels across then the end of the near zone would be the point at which the signal to noise was < 1 for more than 15 pixels. This was used to finalise where the end of the near zone would be. This process is shown in Figure 6.1 for a subsample of the objects given above.

6.3 Near Zone Sizes

The NZ sizes were measured and converted into proper Mpc using a flat ΛCDM concordance cosmology ($\Omega_{m,0}$ = 0.3, Ω_Λ = 0.7 and H_0 = 70.0) and the astropy cosmology package. These were then corrected using the formula from Carilli et al. (2010), which normalises them to an absolute magnitude of -27.0.

$$R_{NZ,corrected} = R_{NZ} \times 10^{0.4(27.0+M_{1450})/3}$$

The resulting near zone sizes are shown in Figure 6.2 and tabulated in Table 6.2. This Figure also shows a comparison to the analytical prediction of Keating et al. (2015) and the observational fit of Carilli et al. (2010). The two circled points at z = 6.5 are both for the same object but from the two different spectra taken of it. These are both shown in Figure 6.3 where it can be seen that the two spectra give different near zone sizes.

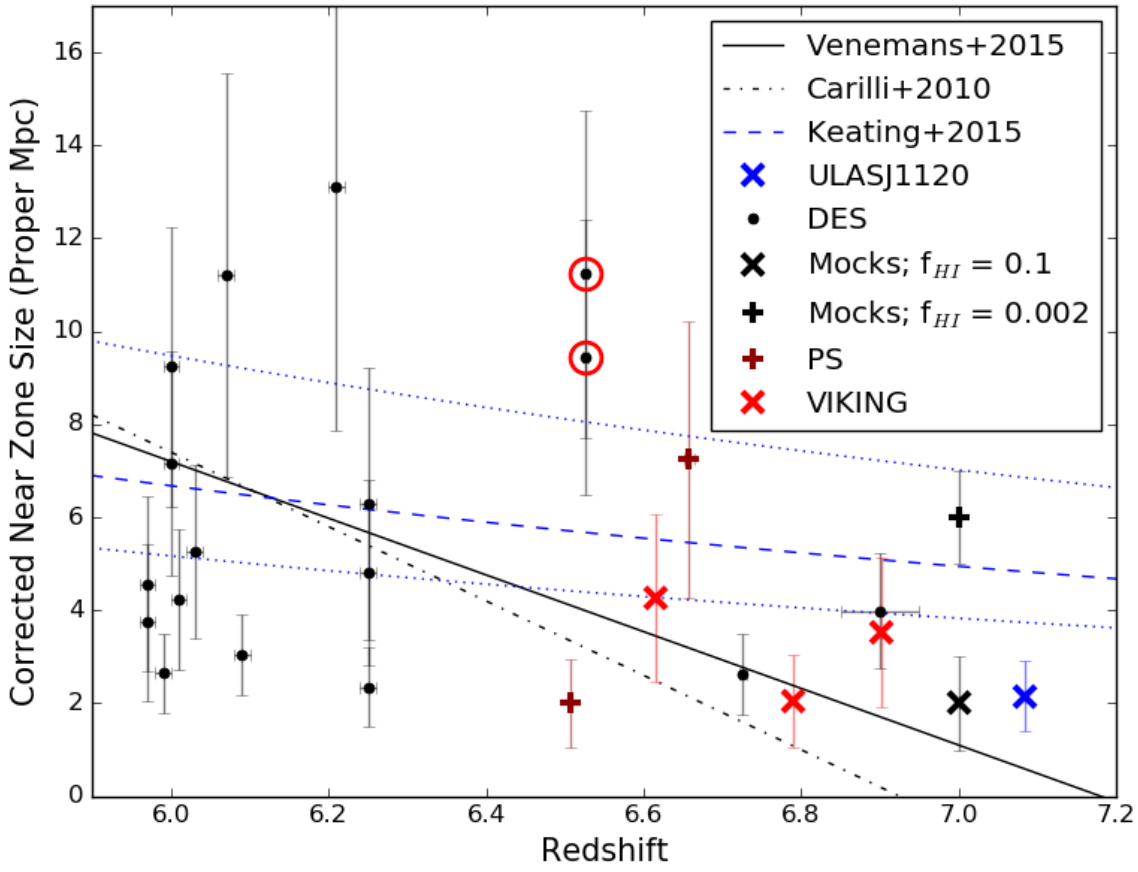

Figure 6.2 The measured near zone sizes compared with analytical predictions from Keating et al. (2015) (the blue dashed line with the 15th and 85th percentiles from the simulations given by the two dotted blue lines), the Carilli et al. (2010) (black dot-dashed line) and Venemans et al. (2015b) (black solid line) fits to observational data. The two points circled in red are the different spectra for the same object.

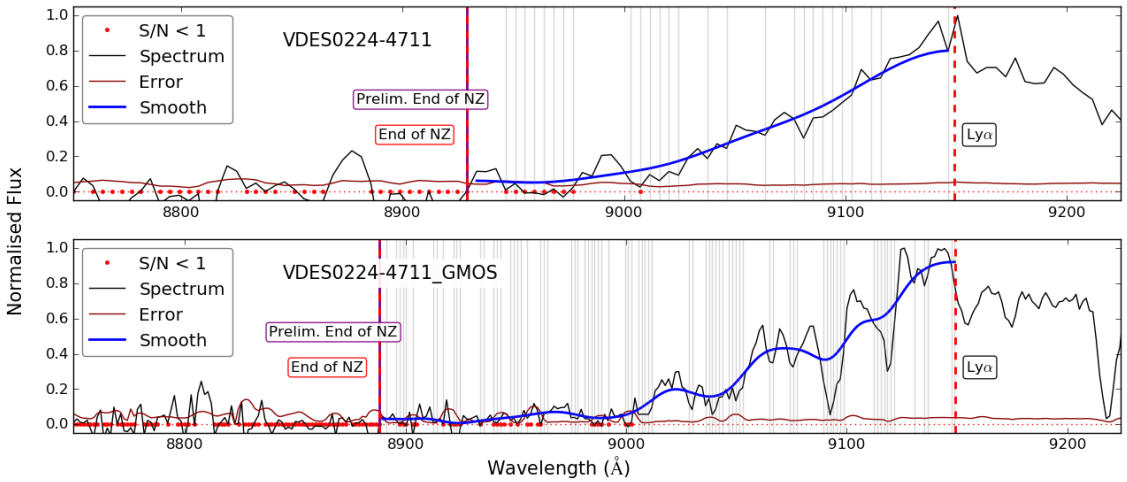

Figure 6.3 The NZ method applied to the two different z = 6.5 quasar spectra. The top spectrum is from GMOS and the bottom one from the NTT. The GMOS spectrum gives a larger NZ size.

Table 6.2 Redshifts and near zone sizes for the quasars used in this study.

Object Name	Redshift	Near Zone Size (Corrected) Mpc
VDES J0020-3653	6.90 ± 0.05	4.0 ± 1.0
VIK J0109-3047	6.7909 ± 0.0004	2.0 ± 1.0
VDES J0109-5423	6.09 ± 0.01	3.0 ± 0.9
VDES J0122-4609	6.00 ± 0.01	9.0 ± 3.0
VDES J0131-3841	6.01 ± 0.01	4.0 ± 2.0
VDES J0143-5545	6.25 ± 0.01	6.0 ± 3.0
VDES J0159-3633	5.99 ± 0.01	2.7 ± 0.9
PS J0167-13	6.508 ± 0.001	2.0 ± 1.0
VDES J0224-4711	6.526 ± 0.003	9.0 ± 3.0
VDES J0224-4711 (GMOS)	6.526 ± 0.003	11.0 ± 4.0
VDES J0244-5008	6.726 ± 0.005	2.6 ± 0.9
VIK J0305-3150	6.6145 ± 0.0001	4.0 ± 2.0
VDES J0323-4701	6.25 ± 0.01	5.0 ± 2.0
VDES J0330-4025	6.25 ± 0.01	2.3 ± 0.9
PSO338+29	6.658 ± 0.007	7.0 ± 3.0
VDES J0408-5632	6.03 ± 0.01	5.0 ± 2.0
VDES J0410-4414	6.21 ± 0.01	13.0 ± 5.0
VDES J0420-4453	6.07 ± 0.01	11.0 ± 4.0
VDES J0433-5153	5.97 ± 0.01	5.0 ± 2.0
VDES J0454-4448	5.10 ± 0.01	6.0 ± 2.0
VDES J0532-4401	5.97 ± 0.01	4.0 ± 2.0
ULAS J1120	7.0851 ± 0.0005	2.0 ± 0.7
VDES J2250-5015	6.00 ± 0.01	7.0 ± 2.0
VIK J2348-3054	6.9018 ± 0.0007	4.0 ± 2.0

6.4 Comparison with Theory

To compare the results of our observations with those from Keating et al. (2015) directly the same method was run over sightlines taken from that simulation. Here we use two of their simulations of a z = 7 quasar one with initial neutral fraction f_{HI} = 0.002 and one with f_{HI} = 0.1 for both of the simulations the quasar has been ionising its surroundings for 1 Myr. These simulations resimulated three haloes taken from the Millennium Simulation (Springel et al., 2005) using the prescription given in Costa et al. (2014). The Millennium Simulation was a large volume dark matter only simulation that ran from z = 127 to z = 0. The large volume allowed the production of the rare, massive haloes which host the largest black holes. Once the z $\sim$ 6 haloes had been selected they were resimulated at higher resolution.

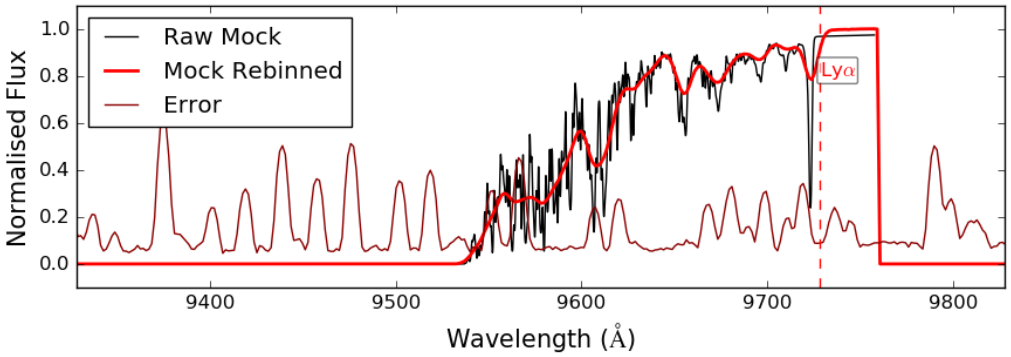

Figure 6.4 An example mock spectrum generated from one sightline to a simulated z = 7 quasar taken from Keating et al. (2015). The overplotted error spectrum is taken from a GMOS observation of a quasar observed in Chapter 4 and scaled to give a signal to noise of 10 at the wavelength of Lyα (1216). The black line shows the spectrum taken directly from the simulation and the red line shows the spectrum after smoothing to the Gemini instrumentation FWHM and rebinning.

The resulting sightlines were convolved with a Gaussian profile with FWHM = 240 kms^{-1} to simulate the effects of the Gemini instrumentation. The mock spectra were rebinned to the Gemini resolution and a typical noise spectrum from a Gemini observation added to represent the observational noise. Due to the box size of the simulation the synthetic spectra did not cover the full wavelength range of the observational data. For all of the sightlines from the f_{HI} = 0.1 simulation the near zone was clearly finished within the length of the spectrum taken from the simulation. For consistency with the observations the mock spectra were superposed onto an array of zeros to represent the lack of transmission at short wavelengths seen in high redshift quasars. An example mock spectrum is shown in Figure 6.4, the error array has been scaled to give a signal to noise of 10 at the wavelength of Lyα at this redshift. For the simulation with f_{HI} = 0.002 16% of the simulated sightlines ended outside of the box. The analysis here therefore artificially truncates the near zone size to be the maximum possible. The median near zone size for the simulation should be unaffected by the truncation as the extreme values are significantly larger than the median value. To counter the systematic effect on the spread in near zone size the 1σ uncertainty was taken from the values smaller than the median and used as the error in both directions. This assumes a Gaussian distribution of the sizes around the median and while this may be incorrect it provides a good first estimate.

6.5 Discussion and Summary

The method presented here has been directly run on the output of hydrodynamical simulations. When the method was run on the results of a z = 7 simulation with f_{HI} = 0.1 (Figure 6.2; black x) it was able to reproduce the result from running the same method on the known z = 7.1 quasar (Figure 6.2; blue x). However while this was not possible with the results from the simulation with f_{HI} = 0.002 (Figure 6.2; black +) the existence of a large number of comparably sized haloes at lower redshift suggests that the assumption that this is due to HI evolution and a high neutral fraction needs to be revisited. Figure 6.2 shows no strong evidence for evolution of NZ size with redshift.

Figure 6.5 shows a comparison between the method presented here and the method from Fan et al. (2006b). It can be seen that the method presented here gives larger NZ sizes for some of the sources. This is because the NZ end is not truncated by absorption features that fall below the 10% threshold as it is for the Fan et al. (2006b) method.

To assess the impact of varying signal to noise on the measurement of the near zone size the near zone sizes of the simulations were calculated with signal to noise at Lyα of 5, 10 and 20. The results of this are shown in Figure 6.6. The large spread in near zone size can be seen in this Figure, the horizontal lines show the median size for each signal to noise and it can be seen that the intrinsic scatter in size is much larger than the change in median size with signal to noise.

6.6 Future Work

This method could be developed further by properly characterising the Lyα forest and the NZ so that a fully Bayesian method can be used to determine if a pixel is more likely to belong to one population or the other. Another way to improve it would be to better model and identify the absorption features in the near zone.

To fully compare the observations to the simulations the simulated spectra would need to cover a large enough wavelength range that they are not artificially truncated by the box size of the simulation. If this is not possible then the shorter spectra would need to be extrapolated to cover the required range.

The simulations can be used to fully investigate the effects of resolution, instrumentational FWHM and signal to noise on the results. This would determine whether a study using data from a variety of different instruments is feasible and if the, often

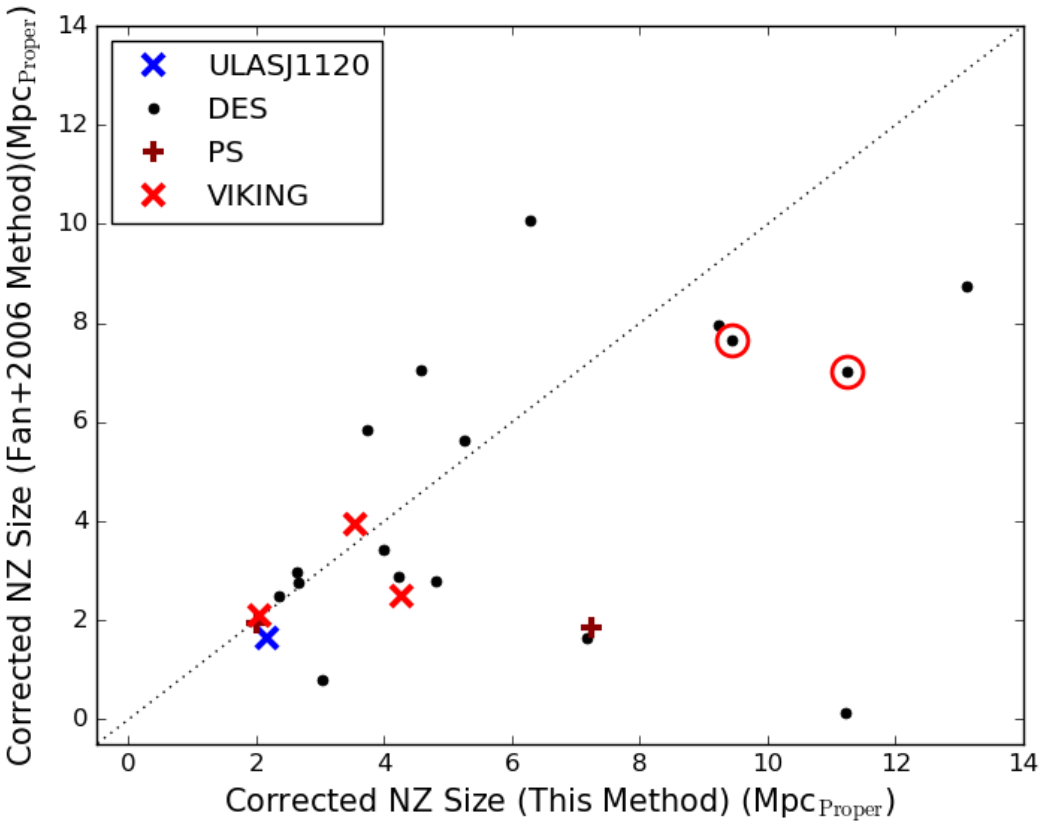

Figure 6.5 The NZ sizes calculated in this Chapter compared with those calculated using the Fan et al. (2006b) method. The black dashed line shows the one to one relation. While most of the points lie close to this line it can be seen that this method tends to give larger measurements of near zone size. The two points circled in red are different spectra for the same object.

poor signal to noise, discovery spectra are sufficient to achieve a meaningful result. Studying a larger number of simulated spectra will give an indication of how many quasars need to be observed to give a statistically robust indication of the effects of a changing neutral fraction.

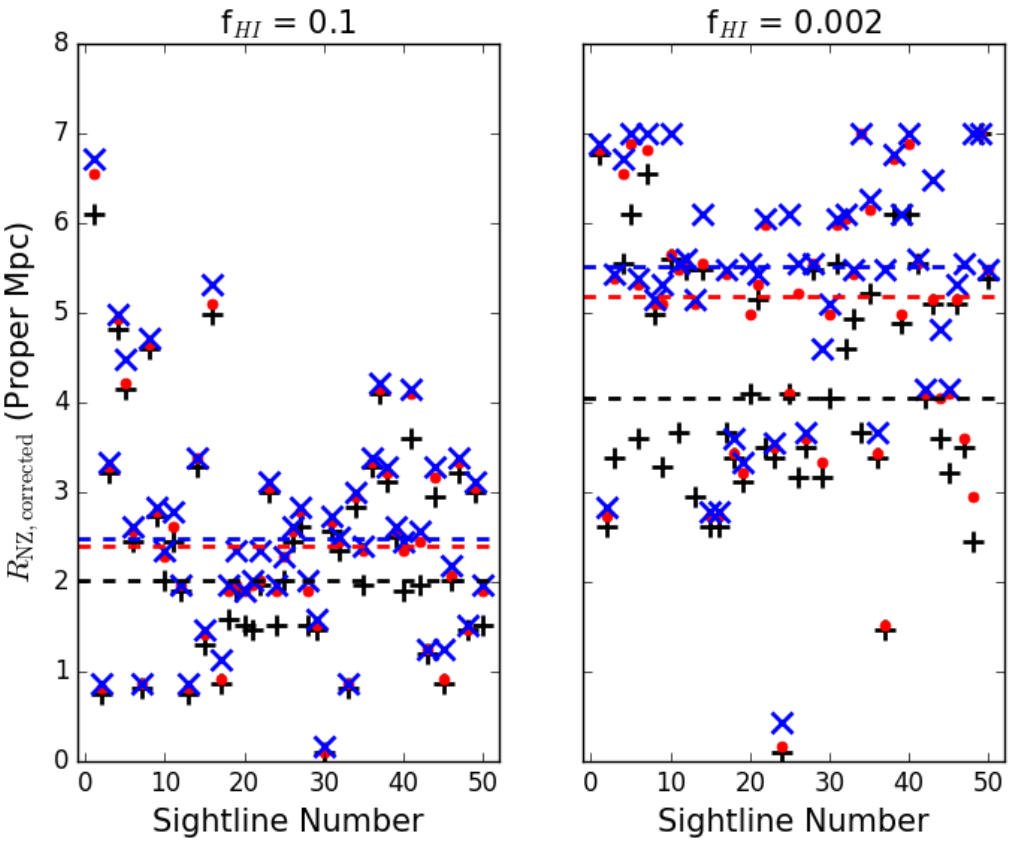

Figure 6.6 The measured near zone sizes for each sightline in each simulation. For each sightline the near zone size was calculated for a signal to noise of 5 (black cross), 10 (red dot) and 20 (blue x). The horizontal lines show the median for all the sightlines for each signal to noise ratio. The intrinsic scatter between the sightlines is much greater than the difference in the medians. The left plot is for the simulation with a larger neutral fraction of hydrogen.

7 Conclusions and Future Work

7.1 Summary

This Thesis has detailed a new robust method of finding high redshift (z > 6.0) quasars without the need for follow up photometric observations. This method was extended to find quasars at z > 6.5. New spectroscopic pipelines were written specifically for the reduction of EFOSC and GMOS observations of high redshift quasars. Once a sample of new quasars had been found the emission line properties of two at $z \geq 6.5$ were studied and the feasibility of using the optical spectrum of quasars with z > 6.0 to study the changing neutral fraction with near zone measurements was investigated.

7.2 Conclusions

This Thesis presented the first search for high redshift quasars in the Dark Energy Survey. The initial selection method presented resulted in the discovery of the first z > 6 quasar from 291 deg^2 of optical imaging data from the DES SV observations. Methods for repeatably removing artefacts, such as cosmic rays and satellite, before visual inspection were developed. These are essential as most catalogue detections that occupy the outlier area of colour space that high redshift quasars habitate are false positive non-Gaussian spurious sources, large numbers of which can swamp candidate lists and cause real candidates to be missed.

Using only the DES photometric data the first photometric error-weighted colour selection described was able to reduce the candidate list to a size suitable for visual inspection and the candidate prioritised for follow up spectroscopy was confirmed to be a z = 6.1 (Reed et al., 2015) quasar without the need for taking any additional photometry. The discovery of one quasar down to a magnitude of 20.1 in the z band was entirely consistent with current predictions of the quasar luminosity function (Willott et al., 2010).

Following the discovery of the first z > 6 quasar the method was further developed to incorporate all the available photometry for the sources. This led to the photometric selection, statistical classification and spectroscopic confirmation of eight new high redshift 6.0 < z < 6.5 quasars with z_{AB} < 21.0 (Reed et al., 2017). These were selected without any morphological star-galaxy classification from $\sim$1500 deg^2 using SED model fitting to photometric data from the Dark Energy Survey (g, r, i, z, Y), the VISTA Hemisphere Survey (J, H, K) and the Wide-Field Infrared Survey Explorer (W1, W2). The initial catalogue contained over 100 million sources and was reduced to 147 candidates using repeatable machine based techniques. These candidates were ranked on their photometric classification which down weighted probable cool stars and any remaining artefacts. Visual inspection could then be performed in a documented, repeatable way using the web interface developed for the purpose to generate a clean list for follow up spectroscopy. The spectral success rate is 100% for this selection technique even without utilising any additional photometry as has been used in previous searches. Automatic removal of the main types of non-astrophysical sources and prioritisation of candidates allows large datasets to be processed without the need for human intervention and without being over run by specious candidates. The highest redshift (z = 6.5) quasar discovered with this method has J_{AB} = 19.75 and is the second most luminous quasar known with z $\geq$ 6.5 and is 0.2 magnitudes fainter than the most luminous known at z $\geq$ 6.5; PSO J0226+0302 at z = 6.53 which has J_{AB} = 19.51 (Venemans et al., 2015b). Candidates were ranked based on the ratio of reduced χ^2-statistic values for the best fit quasar model compared to the best fit stellar model.

This approach is extendible to other photometric systems and imaging surveys (e.g. LSST, Euclid), in contrast to the purely colour cut based criteria widely used in other high redshift quasars searches which generate large numbers of false candidates. The success of this method at producing small, clean candidate lists meant that looser colour cuts could be used to narrow down the initial input list. This resulted in finding objects that would have been missed by previous surveys such as VDES J2250-5015 which was redder in Y - J than the selection cuts in Bañados et al. (2016) and Venemans et al. (2015a). The initial cuts were then relaxed further when the DES Y3 data was analysed resulting in the discovery of five new z $\sim$ 6.0 quasars and the rediscovery of 13 previously known quasars, one of these VDES J0109-5423, had a > 10σ detection in the r band and would not have been selected by the non-relaxed cuts. The relaxed selection maintained the 100% success rate of this technique.

A high redshift quasar specific pipeline to reduce the 2D optical spectra taken as part of this work was written. As high redshift quasars do not have flux over most of

the optical wavelength coverage of the spectrographs used they present challenges for data reduction techniques designed for bright objects with full wavelength coverage. Redshift determination for high redshift quasars is hard to do in a reproducible way from optical spectra as the lines typically used for deriving the redshift (CIV, MgII and CO) are beyond the wavelength coverage of the detector. A technique was developed to reproducibly estimate the redshifts of the objects based on the onset of the Lyα forest and fitting the Lyα emission line with a semi-Gaussian and an exponential. When this method was tested against a sample of quasars with MgII and/or CO emission line redshifts (Carilli et al., 2010) it was found to reproduce the redshifts with a median difference of 0.00 and a distribution of σ_{MAD} = 0.01.

The selection methods developed for use at z $\sim$ 6 where adapted to find z > 6.5 quasars. This resulted in the selection and confirmation of two bright quasars at z = 6.7 and z = 6.9, the identification of one other high priority target for follow up and the rediscovery of one previously known quasar (J0305-3150, J_{AB} = 20.68, z = 6.6, (Venemans et al., 2013)). These objects were identified from the DES Y1 and Y3 releases respectively and were the highest ranked candidates from the selection method. Quasars with z > 6.5 are rare and ones bright enough for absorption line studies to be successful (without requiring considerable amounts of large telescope time) are even rarer. Here the discoveries of two z > 6.5 sources with comparable luminosities to the known z = 7.1 quasar were detailed. The z = 6.7 quasar is the brightest source above z = 6.7 and the z = 6.9 quasar is the third brightest making them ideal probes for the IGM at these redshifts. Both objects are bright enough that even with a relatively short exposure of 30 minutes on an 8m telescope black hole masses could be calculated and the emission line properties studied. The z = 6.7 quasar shows a very strong CIV blueshift which could be indicative of strong disk winds. The Eddington ratio and black hole masses were calculated using two different methods of modelling the line profile. The large difference in the results for each profile for the z = 6.5 quasar is driven by the considerable difference in FWHM for each profile. This difference is indicative of the sensitivity of the calculation to the fitting prescription used to represent the line.

Once a sample of z > 6 quasars had been identified they could be used to study their near zone sizes. A new method was developed that was appropriate for quasars with only optical spectra. The method did not require a continuum fit and was more robust to large, deep absorption features in the near zone. This method was designed to be directly applicable to the output of hydrodynamical simulations thus allowing comparisons to be made directly between the observations and theoretical work. When the method was applied to the output of the simulations from Keating et al. (2015) it

was found that the nearzone size of the known z = 7.1 quasar could be reproduced using a neutral fraction of f_{HI} = 0.1 and not with f_{HI} = 0.002. However the length of time the quasar had been shining for was fixed to a relatively short age of 1 Myr and the size of the near zone will be influenced by how long the quasar has been emitting ionising photons for. The results from the full sample show no strong evidence for evolution in size with redshift. There were also a number of objects with small near zones found at all redshifts which suggests that the assumption that the small size of the near zone of the z = 7.1 quasar can be attributed only to the HI evolution and a high neutral fraction needs to be revisited.

7.3 Future Work

During this Thesis selection methods were developed and applied to wide field surveys to select the brightest high redshift quasar candidates that would be most suitable for follow up absorption line studies. One of the next things to do would be to use this method on deeper surveys to select samples of faint quasars to put constraints on the faint end of the quasar luminosity function at high redshift. Searching for faint quasars will benefit from deeper and more precise unWISE forced photometry. To do this the latest release of unWISE images which incorporates the NEOWISE-R images and has deeper limiting magnitudes could be used. An alternative would be to use an extraction that propagates the detection parameters from the clean detections in the VHS images. This is done on *SPITZER* images using T-PHOT (Merlin et al., 2015) (or similar software) for high redshift galaxy searches and has been done for SDSS sources on the unWISE images (Lang, 2014).

Now that a significant number of quasars have been identified in the DES footprint the selection using only χ^2 cuts can be fully assessed and then run on the whole dataset. Applying no colour cuts to the input data along with the inclusion of more templates would allow the identification of rarer types of quasars such as highly reddened quasars.

The selection method can also be used to search for higher redshift objects. For example a search starting from the VHS data and using forced photometry driven by the VHS positions on the DES images and NEOWISE-R coadded unWISE images could be used to find quasars above z = 7.2 at which point they start to drop out of the Y band.

The method presented in this Thesis for calculating near zone sizes is designed to be applicable to simulated data. This data can then be used to study the effect of resolution and signal to noise on the near zone sizes measured. These simulations

can also be used to assess how large a number of spectra are required to combat the intrinsic distribution of sizes at any given redshift and give a robust indication of the changing neutral fraction.

A

Appendix

A.1 SQL Used In SVA1 Analysis

Here we present the SQL (Structured Query Language) code used to query the SVA1 DES database. This code returns 838 rows from a database with 40,129,963 unique sources as shown in Steps 1-8b in Table 3.2.

```
SELECT

  *

FROM

  SVA1_COADD_GRIZY

WHERE

  /* Flag criteria */
  (FLAGS_G = 0 OR FLAGS_WEIGHT_G = 0 OR
   FLAGS_G > 3) AND
  (FLAGS_R = 0 OR FLAGS_WEIGHT_R = 0 OR
   FLAGS_R > 3) AND
  (FLAGS_I = 0 OR FLAGS_WEIGHT_I = 0 OR
   FLAGS_I > 3) AND
  (FLAGS_Z = 0 OR FLAGS_WEIGHT_Z = 0 OR
   FLAGS_Z > 3) AND
  (FLAGS_Y = 0 OR FLAGS_WEIGHT_Y = 0 OR
   FLAGS_Y > 3) AND
```

```
/* Z band limits */
MAG_PSF_Z <= 21.5 AND MAGERR_PSF_Z < 0.1
AND

/* Morphological criterion */
MAG_PSF_Z - MAG_MODEL_Z < 0.145 AND

/* I-Z colour criterion */
MAG_PSF_I - MAG_PSF_Z > 1.694 AND

/*  G and R dropout criteria */
MAG_PSF_G > 23 AND MAG_PSF_R > 23 AND
MAGERR_PSF_G > 0.1 AND
MAGERR_PSF_R > 0.1 AND

/* Z-Y colour criterion */
MAG_PSF_Z - MAG_PSF_Y < 0.5 AND

/* Y band detection criterion */
MAG_PSF_Y <> 99 AND
MAG_PSF_Y < 23
```

A.2 Colour Terms

The colour terms used in this analysis are included here for completeness.

$$
\begin{aligned}
H_{VHS} - H_{UKIDSS} &= -0.01(i-z)_{SDSS} + 0.02 \\
i_{DES} - i_{SDSS} &= -0.30(i-z)_{SDSS} + 0.02 \\
J_{VHS} - J_{UKIDSS} &= -0.01(i-z)_{SDSS} - 0.02 \\
K_{VHS} - K_{UKIDSS} &= 0.04(i-z)_{SDSS} - 0.07 \\
Y_{DES} - Y_{UKIDSS} &= 0.09(i-z)_{SDSS} - 0.08 \\
z_{DES} - z_{SDSS} &= -0.07(i-z)_{SDSS} - 0.01
\end{aligned}
$$

A.3 Web Interface

Searches for high redshift quasars are heavily contaminated by both astrophysical contaminants and imaging artefacts. During this Thesis algorithms were developed to remove both of these populations automatically. In order not to remove rarer, stranger looking quasars, for example the very red quasar discovered in Chapter 4, the cuts used to remove contaminants were left deliberately loose. While the selection detailed in this Thesis has proved to be much cleaner than previous surveys have managed it still has contaminants that have to be removed via visual inspection. The final step to a clean candidate list is a tool that allows reproducible, fast and well informed visual inspection. To address this need a web interface to a SQL database was developed which allowed classification and comments to be easily shared between collaborators. The following series of Figures show the usage of the web interface.

The first step to using the interface is to log in and then select the required survey, data release and selection criteria. This leads to the table shown in Figure A.1 which contains links to pages with detailed information on each object. Subsections of this table can be made using the SQL interface at the top of the page. For example viewing only objects that have been classified as known quasars can be done by requesting that the variable class = 100. Columns can also be added or removed to the visible ones at this stage allowing access to all the $\sim$1000 columns that are present in the table at the end of the code without displaying ones that are not relevant at this stage.

Each object links to a page with more information on it. This page has more catalogue information, shown in Figure A.2 along with cutout images from DES, VHS and WISE. Also on this page are the results of the photometric fitting algorithms and the option to classify the object and submit comments about it, the comment and classification options are shown at the bottom of Figure A.3.

Grouping all of the relevant information into one easy to use page allows visual inspection to be performed quickly. Storing the comments and classifications of all the users who access the table makes it easy to compare differing opinions on an object and helps to ensure that low priority candidates are not submitted for follow up. This interface, along with other library code developed during this Thesis, is used as part of ongoing lensed quasar and high redshift galaxy candidate selection efforts.

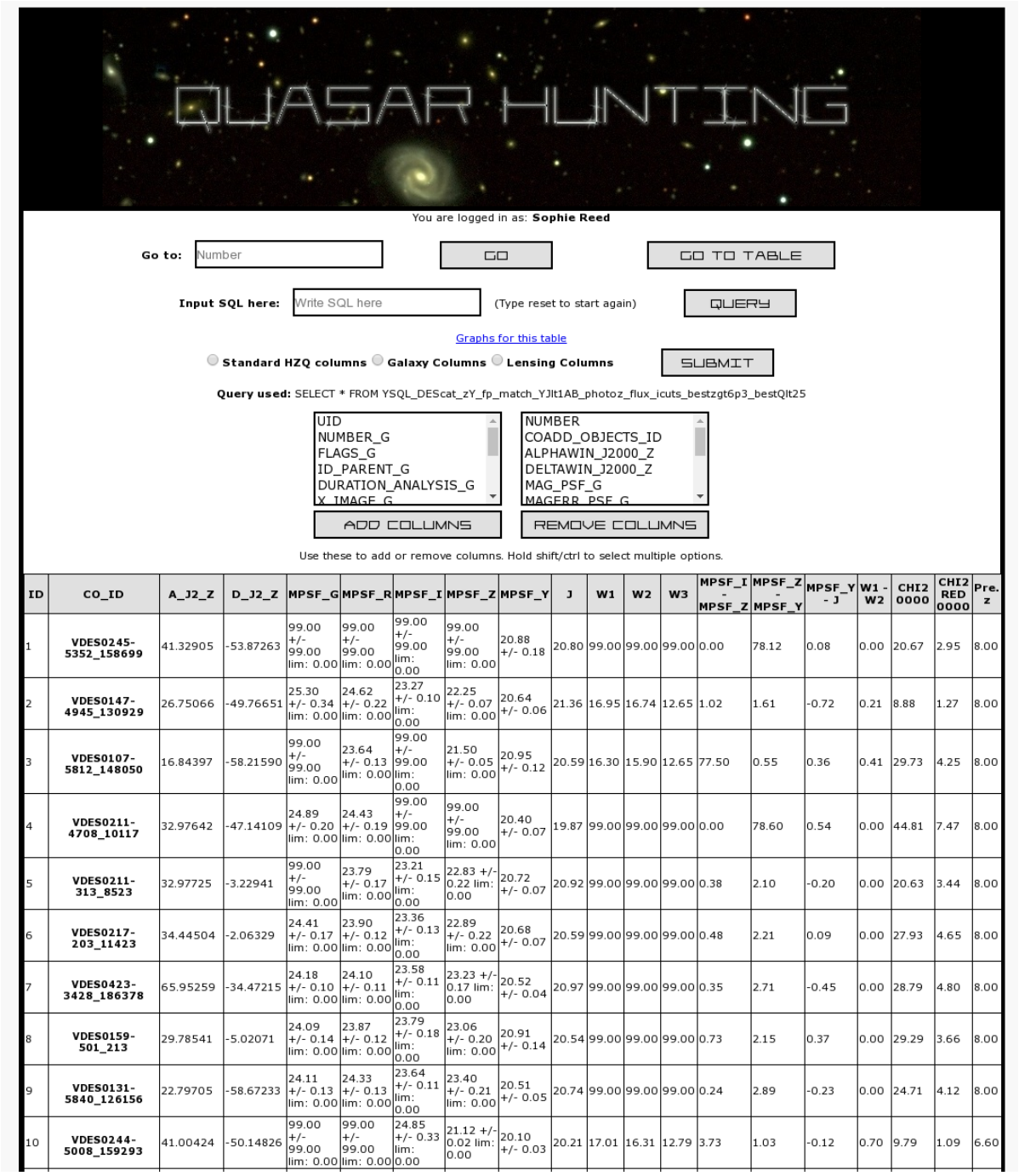

ID	CO_ID	A_J2_Z	D_J2_Z	MPSF_G	MPSF_R	MPSF_I	MPSF_Z	MPSF_Y	J	W1	W2	W3	MPSF_I - MPSF_Z	MPSF_Z - MPSF_Y	MPSF_Y - J	W1 - W2	CHI2 0000	CHI2 RED 0000	Pre. z
1	VDES0245-5352_158699	41.32905	-53.87263	99.00 +/- 99.00 lim: 0.00	99.00 +/- 99.00 lim: 0.00	99.00 +/- 99.00 lim: 0.00	99.00 +/- 99.00 lim: 0.00	20.88 +/- 0.18	20.80	99.00	99.00	99.00	0.00	78.12	0.08	0.00	20.67	2.95	8.00
2	VDES0147-4945_130929	26.75066	-49.76651	25.30 +/- 0.34 lim: 0.00	24.62 +/- 0.22 lim: 0.00	23.27 +/- 0.10 lim: 0.00	22.25 +/- 0.07 lim: 0.00	20.64 +/- 0.06	21.36	16.95	16.74	12.65	1.02	1.61	-0.72	0.21	8.88	1.27	8.00
3	VDES0107-5812_148050	16.84397	-58.21590	99.00 +/- 99.00 lim: 0.00	23.64 +/- 0.13 lim: 0.00	99.00 +/- 99.00 lim: 0.00	21.50 +/- 0.05 lim: 0.00	20.95 +/- 0.12	20.59	16.30	15.90	12.65	77.50	0.55	0.36	0.41	29.73	4.25	8.00
4	VDES0211-4708_10117	32.97642	-47.14109	24.89 +/- 0.20 lim: 0.00	24.43 +/- 0.19 lim: 0.00	99.00 +/- 99.00 lim: 0.00	99.00 +/- 99.00 lim: 0.00	20.40 +/- 0.07	19.87	99.00	99.00	99.00	0.00	78.60	0.54	0.00	44.81	7.47	8.00
5	VDES0211-313_8523	32.97725	-3.22941	99.00 +/- 99.00 lim: 0.00	23.79 +/- 0.17 lim: 0.00	23.21 +/- 0.15 lim: 0.00	22.83 +/- 0.22 lim: 0.00	20.72 +/- 0.07	20.92	99.00	99.00	99.00	0.38	2.10	-0.20	0.00	20.63	3.44	8.00
6	VDES0217-203_11423	34.44504	-2.06329	24.41 +/- 0.17 lim: 0.00	23.90 +/- 0.12 lim: 0.00	23.36 +/- 0.13 lim: 0.00	22.89 +/- 0.22 lim: 0.00	20.68 +/- 0.07	20.59	99.00	99.00	99.00	0.48	2.21	0.09	0.00	27.93	4.65	8.00
7	VDES0423-3428_186378	65.95259	-34.47215	24.18 +/- 0.10 lim: 0.00	24.10 +/- 0.11 lim: 0.00	23.58 +/- 0.11 lim: 0.00	23.23 +/- 0.17 lim: 0.00	20.52 +/- 0.04	20.97	99.00	99.00	99.00	0.35	2.71	-0.45	0.00	28.79	4.80	8.00
8	VDES0159-501_213	29.78541	-5.02071	24.09 +/- 0.14 lim: 0.00	23.87 +/- 0.12 lim: 0.00	23.79 +/- 0.18 lim: 0.00	23.06 +/- 0.20 lim: 0.00	20.91 +/- 0.14	20.54	99.00	99.00	99.00	0.73	2.15	0.37	0.00	29.29	3.66	8.00
9	VDES0131-5840_126156	22.79705	-58.67233	24.11 +/- 0.13 lim: 0.00	24.33 +/- 0.13 lim: 0.00	23.64 +/- 0.11 lim: 0.00	23.40 +/- 0.21 lim: 0.00	20.51 +/- 0.05	20.74	99.00	99.00	99.00	0.24	2.89	-0.23	0.00	24.71	4.12	8.00
10	VDES0244-5008_159293	41.00424	-50.14826	99.00 +/- 99.00 lim: 0.00	99.00 +/- 99.00 lim: 0.00	24.85 +/- 0.33 lim: 0.00	21.12 +/- 0.02 lim: 0.00	20.10 +/- 0.03	20.21	17.01	16.31	12.79	3.73	1.03	-0.12	0.70	9.79	1.09	6.60

Figure A.1 After logging in and selecting the relevant survey, data release and selection criteria the user is presented with a table of the objects included in that selection.

Go to: Number GO GO TO TABLE START

PREVIOUS 24 NEXT

COADD OBJECTS ID: VDES0020-3653_56554, **RA:** 5.13113295958, **Dec**: -36.8949487627
RNUM: r2590, **PNUM:** p02, **Tilename:** DES0021-3706

Graphs for this table

Bands	PSF Magnitudes	Mag Limits	Aperture 3 Magnitudes	Model Magnitudes	Det Model Magnitudes	Auto Magnitudes	Spread Models	PSF Magnitude - Model Magnitude	PSF Magnitude - Apeture 3 Magnitude
g	99.00 +/- 99.00	0.00	0.00 +/- 0.00	0.00 +/- 0.00	0.00 +/- 0.00	27.58 +/- 3.94	0.00	99.00	99.00
r	25.53 +/- 0.60	0.00	0.00 +/- 0.00	0.00 +/- 0.00	0.00 +/- 0.00	99.00 +/- 99.00	0.00	25.53	25.53
i	25.01 +/- 0.64	0.00	0.00 +/- 0.00	0.00 +/- 0.00	0.00 +/- 0.00	99.00 +/- 99.00	0.00	25.01	25.01
z	21.39 +/- 0.04	0.00	0.00 +/- 0.00	0.00 +/- 0.00	0.00 +/- 0.00	21.54 +/- 0.08	0.00	21.39	21.39
Y	19.98 +/- 0.03	0.00	0.00 +/- 0.00	0.00 +/- 0.00	0.00 +/- 0.00	20.10 +/- 0.06	0.00	19.98	19.98

VHS Magnitudes [AB]
J: 20.40 +/- 0.10 **K:** 19.55 +/- 0.13

WISE Magnitudes
[VEGA]
W1: 16.84 +/- 0.09 **W2:** 16.35 +/- 0.20 **W3:** 12.68 +/- 0.00 **W4:** 8.34 +/- 0.00
[AB]
W1: 19.54 +/- 0.09 **W2:** 19.69 +/- 0.20 **W3:** 17.85 +/- 0.00 **W4:** 14.96 +/- 0.00

Colours
g - r: 73.47 **r - i:** 0.52 **i - z:** 3.62 **z - Y:** 1.41 **Y - J:** -0.42 **J - K:** 0.85 **K - W1:** 0.01 **W1 - W2:** -0.15 **W2 - W3:** 1.84 **W3 - W4:** 2.89

Classifications
Phi izY: 0.00 **Phi iz:** 0.00 **Phi zY:** 0.00 **Classification:** 100 **Number of epochs detected in the z band:** 0

Links
The coordinates in WISE
NED Link
Is it an asteroid in z?
SDSS DR9 Skyserver Link

VIEW COMMENTS

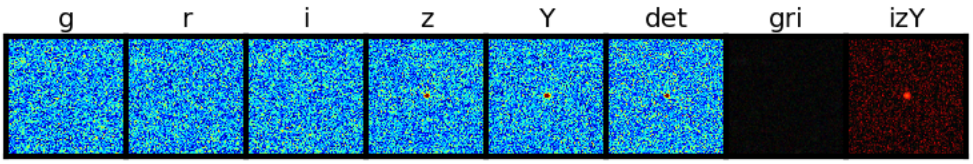

No Annotation Smoothed Catalogue Information Object Circled CHANGE

Figure A.2 Each object in the table shown in Figure A.1 links to a page of detailed information on the object. An example of this for the z = 6.9 quasar discovered in Chapter 5 is shown here.

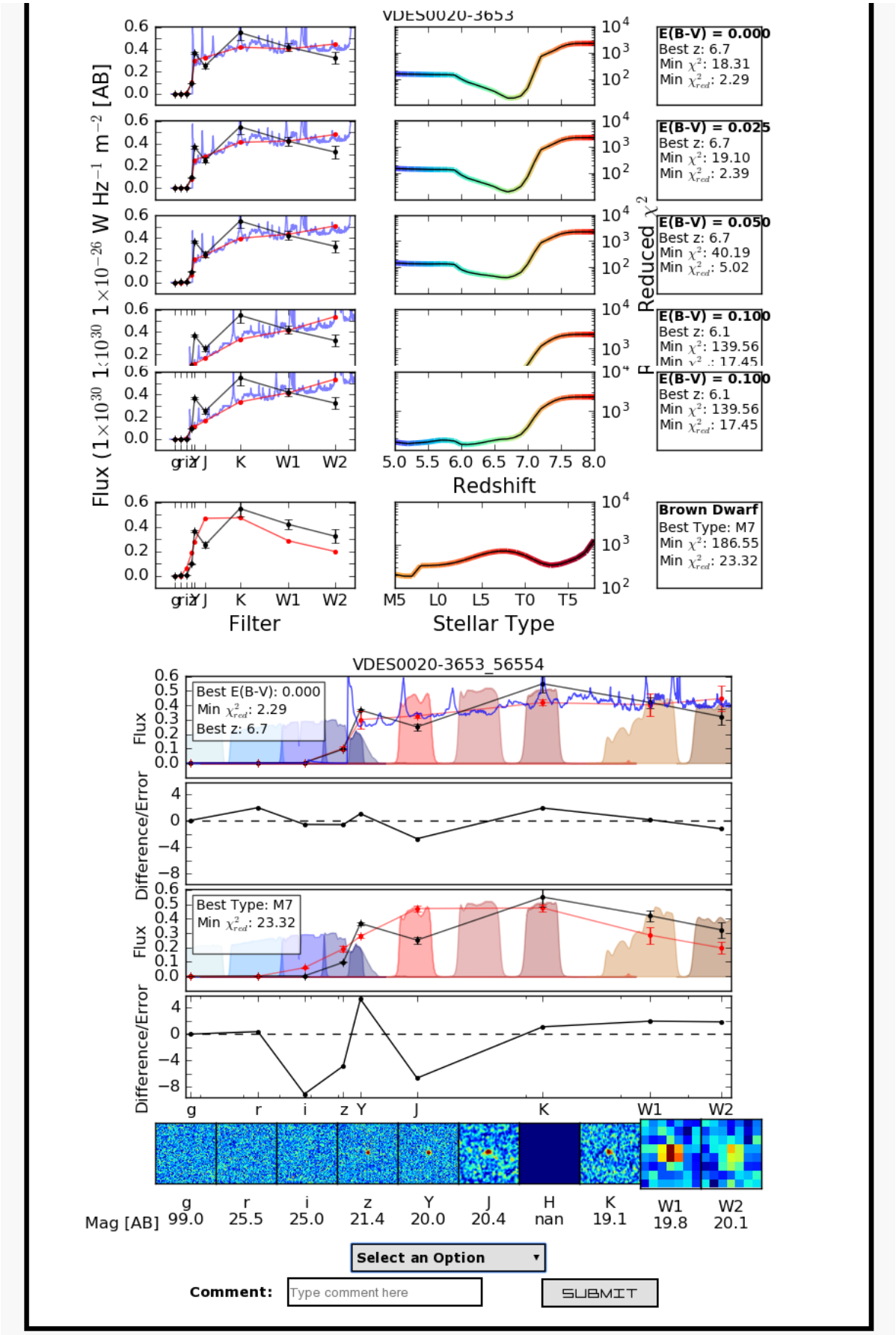

Figure A.3 More of the page shown in Figure A.2. At the bottom of the page is a drop down menu of classification options and a box to allow comments to be submitted.

Bibliography

Aihara H., et al., 2017, preprint, (arXiv:1704.05858)

Assef R. J., Kochanek C. S., Brodwin M., Cool R., Forman W., Gonzzalez A. H., Hickox R. C., et al., 2010, ApJ, 713, 970

Astropy Collaboration et al., 2013, A&A, 558, A33

Bañados E., Venemans B. P., Decarli R., Farina E. P., Mazzucchelli C., Walter F., Fan X., Stern D., 2016, preprint, (arXiv:1608.03279)

Becker G. D., Rauch M., Sargent W. L. W., 2007, ApJ, 662, 72

Becker G. D., Bolton J. S., Madau P., Pettini M., Ryan-Weber E. V., Venemans B. P., 2015, MNRAS, 447, 3402

Bertin E., 2006, in Gabriel C., Arviset C., Ponz D., Enrique S., eds, Astronomical Society of the Pacific Conference Series Vol. 351, Astronomical Data Analysis Software and Systems XV.

Bertin E., 2011, in Evans I. N., Accomazzi A., Mink D. J., Rots A. H., eds, Astronomical Society of the Pacific Conference Series Vol. 442, Astronomical Data Analysis Software and Systems XX. p. pages435

Bertin E., Arnouts S., 1996, Astronomy and Astrophysics Supplement, 117, 393

Bertin E., Mellier Y., Radovich M., Missonnier G., Didelon P., andMorin B., 2002, in Bohlender D. A., Durand D., Handley T. H., eds, Astronomical Society of the Pacific Conference Series Vol. 281, Astronomical Data Analysis Software and Systems XI. p. 228

Blain A. W., et al., 2013, ApJ, 778, 113

Bolton J. S., Haehnelt M. G., 2007, MNRAS, 374, 493

Bolton J. S., Haehnelt M. G., Warren S. J., Hewett P. H., Mortlock D. J., Venemans B. P., McMahon R. G. andnd Simpson C., 2011, MNRAS, 416, L70

Bouwens R. J., Illingworth G. D., Oesch P. A., Caruana J., Holwerda B., Smit R., Wilkins S., 2015, ApJ, 811, 140

Buzzoni B., et al., 1984, The Messenger, 38, 9

Carilli C. L., et al., 2010, ApJ, 714, 834

Carnall A. C., et al., 2015, ArXiv e-prints,1502.07748,

Chambers K. C., et al., 2016, preprint, (arXiv:1612.05560)

Coatman L., Hewett P. C., Banerji M., Richards G. T., 2016, MNRAS, 461, 647

Costa T., Sijacki D., Haehnelt M. G., 2014, MNRAS, 444, 2355
Cross N. J. G., et al., 2012, A&A, 548, A119
Dalton G. B., et al., 2006, in Society of Photo-Optical Instrumentation Engineers (SPIE) Conference Series. p. 62690X, doi:10.1117/12.670018
Danforth C. W., Keeney B. A., Stocke J. T., Shull J. M., Yao Y., 2010, ApJ, 720, 976
De Rosa G., Decarli R., Walter F., Fan X., Jiang L., Kurk J., Pasquali A., Rix H. W., 2011, ApJ, 739, 56
De Rosa G., et al., 2014, ApJ, 790, 145
Desai S., et al., 2012, ApJ, 757, 83
Diehl H. T., Abbott T. M. C., Annis J., Armstrong R., Baruah L., Bermeo A., Bernstein G., Beynon 2014, in Observatory Operations: Strategies, Processes, and Systems V. p. 91490V, doi:10.1117/12.2056982
Emerson J. P., et al., 2004, in Quinn P. J., Bridger A., eds, SPIEVol. 5493, Optimizing Scientific Return for Astronomy through Information Technologies. pp 401–410, doi:10.1117/12.551582
Fan X., White R. L., Davis M., Becker R. H., Strauss Z., 2000, AJ, 120, 1167
Fan X., Narayanan V. K., Lupton R. H., Strauss M. A., et al., 2001, ApJ, 122, 2833
Fan X., et al., 2003, AJ, 125, 1649
Fan X., Hennawi J. F., Richards G. T., Strauss M. A., 2004, AJ, 128, 515
Fan X., Strauss M. A., Richards G. T., Hennawi J. F., Becker R. H., White R. L., Diamond-Stanic A. M., Donley J. L., 2006a, AJ, 131, 1203
Fan X., Strauss M. A., Becker R. H., White R. L., Gunn J. E., Knapp G. R., Richards et al., 2006b, ApJ, 132, 117
Flaugher B. L., Abbott T. M. C., Angstadt R., Annis J., Antonik M. L., Bailey J., Ballester O., 2012, in Society of Photo-Optical Instrumentation Engineers (SPIE) Conference Series. p. 11, doi:10.1117/12.926216
Gallagher S. C., Everett J. E., Abado M. M., Keatinging S. K., 2015, MNRAS, 451, 2991
Genzel R., Thatte N., Krabbe A., Kroker H., Tacconi-Garman L. E., 1996, ApJ, 472, 153
Ghez A. M., et al., 2008, ApJ, 689, 1044
Giallongo E., et al., 2015, A&A, 578, A83
Gillessen S., Eisenhauer F., Trippe S., Alexander T., Genzel R., Martins F., Ott T., 2009, ApJ, 692, 1075
Gunn J. E., Peterson B. A., 1965, The Astrophysical Journal, 142, 1633
Hambly N. C., Mann R. G., Bond I., Sutorius E., Read M., Williams P., LawrenceLawrence A., Emerson J. P., 2004, in Quinn P. J., Bridger A., eds, SPIEVol.

5493, Optimizing Scientific Return for Astronomy through Information Technologies. pp 423–431, doi:10.1117/12.551623
Hazard C., Mackey M. B., Shimmins A. J., 1963, Nature, 197, 1037
Hewett P. C., Warren S. J., Leggett S. K., Hodgkin S. T., 2006, MNRAS, 367, 454
Higginbottom N., Proga D., 2015, ApJ, 807, 107
Hook I. M., Jørgensen I., Allington-Smith J. R., Davies R. L., Metcalfee N., Murowinski R. G., Crampton D., 2004, PASP, 116, 425
Irwin M. J., 1985, MNRAS, 214, 575
Irwin M. J., et al., 2004, in Quinn P. J., Bridger A., eds, SPIEVol. 5493, Optimizing Scientific Return for Astronomy through Information Technologies. pp 411–422, doi:10.1117/12.551449
Jarrett T. H., et al., 2011, ApJ, 735, 112
Jiang L., Fan X., Annis J., Becker R. H., White R. L., Chiu K., Lin H., Luminouspton R. H., 2008, AJ, 135, 1057
Jiang L., et al., 2009, The Astronomical Journal, 138, 305
Jiang L., et al., 2016, preprint, (arXiv:1610.05369)
Keating L. C., Haehnelt M. G., Cantalupo S., Puchwein E., 2015, MNRAS, 454, 681
Kirkpatrick J. D., Cushing M. C., Gelino C. R., Griffith R. L., Skyrutskie M. F., Marsh K. A., Wright E. L., Mainzer A., 2011, ApJS, 197, 19
Kron R. G., 1980, ApJS, 43, 305
Lang D., 2014, AJ, 147, 108
Lawrence A., et al., 2007, MNRAS, 379, 1599
Lewis J. R., Irwin M., Bunclark P., 2010, in Mizumoto Y., Morita K.-I., Ohishi M., eds, Astronomical Society of the Pacific Conference Series Vol. 434, Astronomical Data Analysis Software and Systems XIX. p. 91
Loeb A., 2006, Scientific American, 295
Madau P., Haardt F., 2015, ApJL, 813, L8
Maddox N., Hewett P. C., 2006, MNRAS, 367, 717
Maddox N., Hewett P. C., Péroux C., Nestor D. B., Williamssotzki L., 2012, MNRAS, 424, 2876
Marshall J. L., et al., 2008, in Society of Photo-Optical Instrumentation Engineers (SPIE) Conference Series. (arXiv:0807.3774), doi:10.1117/12.789972
McGreer I. D., et al., 2013, ApJ, 768, 105
McLure R. J., Dunlop J. S., 2004, MNRAS, 352, 1390
McMahon R. G., Banerji M., Gonzalez E., Koposov S. E., Bejar B. V. J., Lodieu N., Rebolo R., VHS Collaboration 2013, The Messenger, 154, 35
Merlin E., et al., 2015, A&A, 582, A15

Mohr J. J., et al., 2012, in Society of Photo-Optical Instrumentation Engineers (SPIE) Conference Series. p. 0 (arXiv:1207.3189), doi:10.1117/12.926785
Mortlock D. J., et al., 2011, Nature, 474, 616
Mortlock D. J., Patel M., Warren S. J., Hewett P. C., Venemans B. P., McMahon R. G., Simpsonon C., 2012, MNRAS, 419, 390
Pâris I., et al., 2012, Astronomy and Astrophysics, 548, A66
Pâris I., et al., 2014, A&A, 563, A54
Planck Collaboration et al., 2015, ArXiv e-prints,1502.01589,
Reed S. L., McMahon R. G., Banerji M., Becker G. D., Gonzalez-Solaresres E., Martini P., Ostrovski F., Rauch M., 2015, MNRAS, 454, 3952
Reed S. L., et al., 2017, MNRAS, 468, 4702
Richards G. T., Fan X., Newberg H. J., Strauss M. A., Vanden Berk D. E., Schneider D. P., Yanny B., 2002a, The Astronomical Journal, 123, 2945
Richards G. T., Vanden Berk D. E., Reichard T. A., Hall P. B., Schneider D. P., SubbaRao M., Thakar A. R., YorkYork D. G., 2002b, AJ, 124, 1
Robertson B. E., Ellis R. S., Furlanetto S. R., Dunlop J. S., 2015, ApJL, 802, L19
Schmidt M., 1963, Nature, 197, 1040
Schneider D. P., et al., 2010, AJ, 139, 2360
Skrzypek N., Warren S. J., Faherty J. K., Modesrtlock D. J., Burgasser A. J., Hewett P. C., 2015, A&A, 574, A78
Smartt S. J., Valenti S., Fraser M., Inserra C., Young D. Y., Sullivan M., Pastorello A., Benetti S., 2015, A&A, 579, A40
Springel V., et al., 2005, Nature, 435, 629
Stern D., et al., 2012, ApJ, 753, 30
Stoughton C., et al., 2002, AJ, 123, 485
Sutherland W., et al., 2015, A&A, 575, A25
Swanson M. E. C., Tegmark M., Hamilton A. J. S., Hill J. C., 2008, MNRAS, 387, 1391
Szalay A. S., Connolly A. J., Szokoly G. P., 1999, AJ, 117, 68
Trakhtenbrot B., Volonteri M., Natarajan P., 2017, ApJL, 836, L1
Tytler D., Fan X.-M., 1992, ApJS, 79, 1
Venemans B. P., Findlay J. R., Sutherland W. J., De Rosa G., McMahon R. G., Simcoe R., González-Solares E. A., et al., 2013, ApJ, 779, 24
Venemans B. P., et al., 2015a, MNRAS, 453, 2259
Venemans B. P., et al., 2015b, ApJL, 801, L11
Véron-Cetty M.-P., Véron P., 2010, A&A, 518, A10
Volonteri M., Rees M. J., 2006, The Astrophysical Journal, 650, 669
Willott C. J., Delfosse X., Forveille T., Delorme P., Gwyn S. D. J., 2005, ApJ, 633, 630

Willott C. J., et al., 2007, AJ, 134, 2435
Willott C. J., et al., 2009, AJ, 137, 3541
Willott C. J., et al., 2010, The Astronomical Journal, 139, 906
Wright E. L., et al., 2010, ApJ, 140, 1868
York D. G., Adelman J., Anderson Jr. J. E., Anderson S., Anderson F., Annis J., Bahcall N. A., 2000, AJ, 120, 1579
Zeimann G. R., White R. L., Becker R. H., Hodge J. A., Stanford S. A., Richards G. T., 2011, ApJ, 736, 57
van Dokkum P. G., 2001, PASP, 113, 1420